Fatigue and Fracture of a Railway Wheel Steel

by

David C. Grundy

B.S., University of Pittsburgh (1991)

Submitted to the Department of Materials Science and Engineering
in Partial Fulfillment of the Requirements for the Degree of
Master of Science in Materials Science and Engineering

at

Massachusetts Institute of Technology

May 1994

Signature of Author_____
Department of Materials Science and Engineering
6 May 1994

Certified by_____
Professor Regis M.Pelloux
Thesis Advisor

Accepted by_____
Carl V.Thompson II
Professor of Electronic Materials
Chair, Departmental Committee on Graduate Students

Fatigue and Fracture of a Railway Wheel Steel

by

David C. Grundy

Submitted to the Department of Materials Science and Engineering
on 6 May 1994 in partial fulfillment of the requirements for the
degree of Master of Science in Materials Science and Engineering

ABSTRACT

Federal Railroad Administration (FRA) inspections of three commuter railroads serving the greater New York area found high rates of cracking in the wheels of multiple unit locomotive wheels. The FRA initiated an engineering study to derive long term solutions to the cracking problem which safeguard against catastrophic fracture of a wheel yet are economically reasonable for the railroads .

The mechanical behavior of the Class A and L wheels are studied. Forging operations do not impart any anisotropicity to the wheel microstructure as the grains are equiaxed with respect to the wheel.. Quenching the rims causes the formation of some Widmanstätten plates in Class L wheels near the tread surface but not in Class A . The quench causes the Class A wheel to harden more at the tread surface, but the Class L wheel hardens deeper into the rim. In service, the Class L wheel rim hardens 28% more than a new wheel. Braking transforms the parent ferritic and pearlitic microstructure into one devoid of ferrite grains. This heat affected zone (HAZ) is considerably harder than the parent microstructure and can be as deep as 0.46 mm. Monotonic compression tests of the Class L steel were unable to simulate the HAZ microstructure. These tests did show that recrystallization in Class L steel can be suppressed through increasing strain.

Tensile tests at room temperature indicate a higher yield point for Class L steel than previous studies. Charpy impact tests show the Class A steel to be tougher than Class L. Plane strain fracture toughness testing of Class L steel produced a valid K_{Ic} of 49.6 ksi$\sqrt{in}$ at 0°F. At 70 and 150°F, the toughness is estimated to be 55.5 and 58 ksi$\sqrt{in}$, respectively.

Fatigue tests of Class L steel are conducted under load control and load line displacement (COD) control. The data show that accounting for the closure load gives comparable crack growth rates for tests run at R=-1 and -0.5 and under COD control. Fatigue crack growth rates correlate well with either the cyclic stress intensity range or the cyclic J-integral range. The limited number of visible striations produced during fatigue testing are approximately constant over a wide range of crack growth rates. Under identical loading conditions, calculations reveal surface crack sizes of rim edge cracks are smaller than those for center tread cracks. Estimates of the braking cycles needed to attain critical crack sizes indicate that center tread cracks can reach critical size faster than rim front edge cracks, although this is primarily due to the different initial crack sizes of the two. An attempt to account for closure affects in these predictions shortens the life by 65%.

Thesis Supervisor: Regis M. Pelloux
Title: Professor of Materials Science and Engineering

TABLE OF CONTENTS

LIST OF FIGURES

LIST OF TABLES

ACKNOWLEDGMENTS

Primary thanks are extended to Prof. Regis "Boss" Pelloux for the opportunity to work on this project. I would like to thank you for your patience (going north to get to Canton) for I know I've pressed the limits of it, especially in the completion of this thesis. I would also like to say that having you as an advisor brings a peace of mind in that I know that any problem I have can be solved by a quick trip to your office for a 10 minute chat wherein I become the proud owner of a few post-it notes or, at most, a sheet of loose-leaf paper with the equivalent of a book chapter's information on it.

I must also thank Dr. Jin Liang for your help, especially these past few days. I would like to thank you for answering all of the questions I kept bombarding you with and for steering me from paths on which my ignorance was leading me.

At VNTSC, I would like to thank Dr. Oscar Orringer for financial support, the steady supply of very heavy chunks of wheel and the extension of your help, in general. Also, to Jeff Gordon for allowing me to set up camp in your office for half a day to peruse all of your papers and for the info on the TGV (found that tape yet?).

To Dr. David Jablonski for the essential use of all the machinery at Instron and for not blinking when I erased all the pertinent programs from the PC.

Around the lab, I'd like to thank Jean Marc Genkin for figuring everything out and explaining it to me later.

Special thanks are extended to friends made since my arrival at MIT, the likes of which include Kristi "The Hawaiian Terror" Fukami, my vertically challenged, geography impaired (go ahead, ask her to point to Nebraska on a map) goombah from the middle of the Pacific Ocean, my partner in crime (or have you repressed that memory) without whom I'm certain to have folded my tent in the first term and certainly would have starved to death without this past term (I still think I owe you a few Whoppers). I wish you luck in your job and happiness in your nascent marriage. To Clarence Chui for brainstorming the most memorable birthday, the introduction to Lansdowne St. followed by the ingestion of whole deep fried shrimp (shell, antennae and all) followed by the Loft, for the late nighters concerning this that or the other thing, for completing the most spectacular double dating duo the planet has ever seen, for the general abuse of your stereo and speakers but especially for understanding my obscure references (put the gears of pain away). To Brian Gally for the tireless absorption of my harshest digs and the occasional, yet usually tepid rebuttal, for the introduction to real camping and hiking (the next time I leave the camera in the car, flog me), for accepting the ultimate skier's hell, sailing, running and biking, for the use of your car, I am eternally grateful, for setting a desirable work ethic example that I simply must achieve someday and most of all for your dependable and unwavering help these past few weeks, including the dutiful profreading of this here thesis.

And thanks to friends from home: Jim, for the timely phone call returns and the choicest study clothing (Dartmouth, CWRU), John & Jen for the home away from hell, V & Janet, use the phone bills as an indicator of my gratitude, Rob for the monthly Simpson's review, for living a dream and passing it along, the Sejvar's for the letters and the M&M's, Dr.D.J.Simons for the constant push to apply here. To you all, my appreciation is bellied by my few words.

Ultimately, I would like to give credit to my family, Reed, Jane, Leslie and Tim. It is no small statement that I could not have done this without you.

1.0 INTRODUCTION

1.1 COMMUTER CAR WHEEL CRACKING

Inspections of three commuter railroads in the New York area conducted by the Federal Railroad Administration (FRA) found high thermal cracking rates in multiple unit locomotive wheels. Cracks in wheel treads are removed by trueing the wheelset; material is removed until no cracks remain on the surface. Records from the railroads indicate that as many as 1500 wheels require trueing over an eight month period[1]. The railroads in question operate similar vehicles yet the types of cracks exhibited vary[2]. The rail line experiencing the highest cracking rate operates vehicles with moderate weights at moderate speeds. Tread brakes are assisted by blended dynamic braking for deceleration. Thermal cracks form at the rim front edge. Another rail line plagued by comparable cracking rates operates moderately heavy vehicles at high speed but slows the cars using only tread brakes. The dominant thermal cracks here usually form at the tread center (Fig. 1.1). The third railroad, operating heavy cars at moderate speeds using combined tread and blended dynamic braking, forms thermal and mechanical cracks.

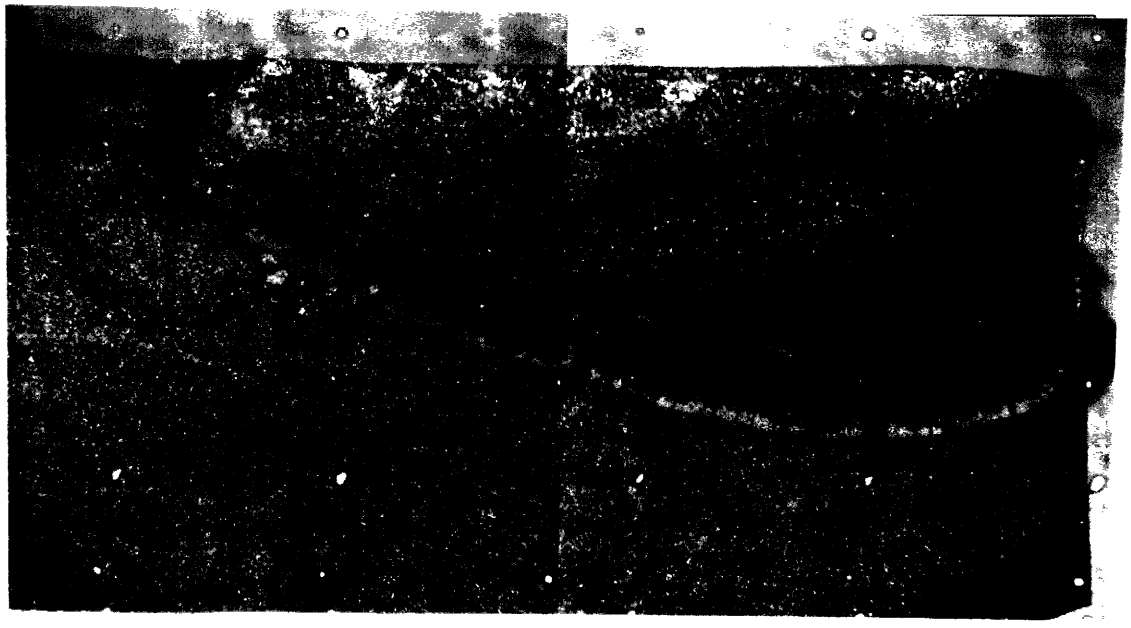

Fig. 1.1 The fracture surface of a thermal fatigue crack from a Class L wheel. (3.6x)

FRA regulations define a wheel with any crack to be defective and must be removed from service for trueing[2]. The Field Manual of the Interchange Rules, the published railroad industry standards, also dictates any wheel with a crack to be defective, but allows for the continued use of wheels affected by thermal checks[3].

Because of these differences, conflicts arise between federal and railroad inspector's interpretations of damaged wheels.

In light of these conflicts the FRA and the affected railroads agreed to a new set of guidelines for dealing with damaged wheels[2]. Part of the guidelines involve improving the maintenance of braking systems. Inspections of wheels for thermal cracks are to be conducted daily. The discovery of thermal cracks in either the flange or the rim front edge requires immediate trueing. Center tread cracks (< 1/2" long) are acceptable.

1.2 PROJECT MOTIVATION

Realizing the cost involved to the railroads in upholding the guidelines, the FRA initiated an engineering study to probe possible alternate and long term solutions to the instituted guidelines[2]. The part of the study which forms the basis for this thesis is the determination of the mechanical behavior of the wheel steel and an estimate of the life of a wheel given surface cracks of certain initial size.

1.3 WHEEL PRODUCTION

Either the Association of American Railroads (AAR) or the American Society for Testing and Materials (ASTM) specifications (M-107 and A504-89, respectively) dictate the manufacture of steel wheels[4]. The specifications outline five wheel classes (U, L, A, B and C) and serve as guidelines for intended service conditions, steel carbon content and heat treatment (Table 1.1)[5]. All wheel steels contain between 0.60 and 0.85 weight percent (w/o) Mn, less than 0.05 w/o each of S and P and more than 0.15 w/o Si. Class L, A, B and C wheels are rim quenched and tempered to meet required hardnesses.

Table 1.1 The carbon content in weight percent, the Brinell hardness number (BHN) in kgf/mm^2 and intended service conditions for the five steel wheel classes.

Class	w/o C	BHN	Service Conditions
U	0.65-0.77	—	General service where an untreated wheel is satisfactory
L	≤0.47	197-277	Light wheel loads, high speed service, more severe braking conditions than other classes
A	0.47-0.57	255-321	Moderate wheel loads, high speed service, severe braking conditions
B	0.57-0.67	277-341	Heavy wheel loads, high speed service, severe braking conditions
C	0.67-0.77	321-363	(1) High wheel loads under light braking (2) Heavier braking conditions employing off-tread brakes

The inspected railroads use forged 32 inch diameter Class L wheels with a reversed dish, straight plate design[2]. Two of the railroads replaced defective Class L

wheels with Class A sporting an S plate design. Production of steel wheels is as follows[4]. Wheel blocks are heated to 1175°F, descaled with high pressure water jets and upset forged into a disk. A rough wheel including initial shaping of the rim, flange, hub and plate is formed during the second forging. Wheel rolling contours the wheel tread, flange, rim faces and plate while maintaining the desired diameter. The wheel is then coned and the hub punched followed by controlled cooling to 1000°F. At this point Class U wheels are slowly cooled to 300°F. The remaining Classes are reheated to 1600°F for heat treatment. Submersion in water quenches only the rim. Hardness requirements, rim thickness and wheel diameter dictate quench times. Reheating to 900°F tempers the quench[6]. The final forging step is slow cooling to 300°F. Final dimensions are achieved by turning on a lathe followed by inspection of surfaces, dimensions, concentricity, internal quality, plate shot peening and a final inspection.

Rim quench and temper practices increase the wear resistance of the tread surface and produce a residual compressive hoop stress. Because the AAR and ASTM specifications mandate only a single Brinell hardness measurement as the target for successful heat treatments, variation between wheels and manufacturers can be expected. To illustrate this, typical wheel steel mechanical properties are listed in Table 1.2[2,6-12]. Class L wheel steel has been poorly characterized with respect to the other classes.

Table 1.2 Mechanical properties of wheel steels. Samples removed from the rim are designated as r and p for plate. Stresses are in ksi, %el is the percent elongation, %RA is the percent reduction in area, K_I is in ksi$\sqrt{in}$. For K_I data the subscript c indicates a valid test while Q is for invalid tests. Also, numbers 1 through 8 correspond to temperatures of -40, 0, 25, 70, 100, 150, 200 and 300°F, respectfully.

		σ_{ys}	UTS	%el	%RA	K_I
U	r	50-66	109-126	9	15	29_{Q1} 34_{Q2} 39_{c3} 39_{c4} 42_{Q5} 45_{Q6} 55_{Q7} 44_{Q8}
	p	50-68	109-127	9	18	32_{c1} 31_{Q2} 47_{Q4}
L	r	63	105			
	p					
A	r	65-97	104-139	11-17	13-44	53_{Q1} 54_{Q2} 57_{Q4} 52_{Q6} 57_{Q8}
	p	45-54	90-107	14	8-35	47_{Q1} 51_{Q2} 42_{Q4}
B	r	80-88	135-145			
	p	50-55	110-117			
C	r	57-127	119-178	8-11	8-33	36_{c1} 36_{c2} 54_{c4} 67_{Q6} 66_{Q8}
	p	47-66	108-128	10	21	28_{Q1} 27_{Q2} 34_{Q4}

1.4 SURFACE DEFECTS AND CAUSES

Railroad wheels must support and steer the car, while serving as a brake drum. These primary functions subject wheels to various service loads each of which causes damage. A moving train's kinetic energy is transferred by friction into the wheel as heat

during deceleration. This large thermal input expands the surface of the tread and develops compressive stresses against the tensile stresses of the plate and hub. Elevated temperatures promote plastic deformation through yield stress reduction. Any inelastic deformation at high temperatures affects the quench compressive residual stress state upon cooling[6]. The new stress state depends upon the severity and duration of the braking and the prior loading history.

1.4.1 SHALLOW CRACKS

Mechanisms of crack formation are attributable to thermal and mechanical loads. A local hot spot on the tread surface, formed by either braking or sliding, chilled by the rail (able to cool over 100°F per pass) contracts under the constraint of the surrounding material[13]. This describes thermal checking, small, benign cracks which do not propagate by thermal loads[6,13]. If the local hot spot reaches 1333°F, subsequent cooling may form martensite[14]. "Spalls" form by either fracture of the brittle, untempered martensite patch or from volumetric differences between the martensite and parent pearlite crystal structures[15]. Another process, shelling, produces a surface defect indistinguishable from spalling[16]. The load on a wheel causes high contact stresses at the rail. The low coefficient of friction between wheel and rail hinders the development of significant surface tractions. Rolling contact induces maximum shear stresses and crack initiation below the tread surface[17]. The crack (or a thermal check or a spall), driven by compressive rolling stresses, propagates at an angle to the tread surface[15]. The cracks grow in the circumferential direction and if progress far enough, will "shell" a thin slab of tread material[6].

1.4.2 DEEP CRACKS

For a more severe stop braking condition, e.g. high speed service lines, a larger volume of the rim can undergo plastic deformation. Cooling, contracting tread surface material places more of the rim volume in tension. Under these conditions thermal fatigue cracks initiate and propagate[6]. Under drag braking conditions, extreme thermal input occurs which can fracture the wheel[18]. Fracture is caused by the complete reversal of the quench compressive residual stress state to that where the entire rim has undergone plastic deformation and upon cooling, contracts, becomes tensile and has enough stored elastic strain energy to drive the crack to failure.

1.5 OBJECTIVE

Class L wheel steel is the primary material studied. This is compared to Class A wheel steel. Metallography is performed to ascertain the effects of fabrication steps and braking on rim and tread microstructures: the grain size, volume fraction ferrite and

interlamellar spacing. The characterization of the microstructural development of Class L steel wheels under heavy braking conditions necessitates thermomechanical testing. Variations of test temperature and monotonic plastic strain simulate service conditions in an attempt to recreate the heat affected zone (HAZ) of the tread surface. In conjunction with changes in the microstructure caused by either fabrication or service conditions there will be changes in the mechanical properties of the wheel. These changes are assessed by measuring microscopic (Knoop) and macroscopic (Rockwell) hardnesses. The reported Class L yield strength (Table 1.2) is lower than steels of similar carbon content[19]. As the validity of linear elastic fracture mechanics parameters depends upon the yield strength, tensile tests are conducted to accurately establish the yield point. The Charpy impact test yields an energy value (CVN) that represents the work required to initiate a crack from a notch and propagate the crack through the sample ligament. This is a qualitative representation of a material's toughness. In contrast to the Charpy impact energy, the plane strain fracture toughness (K_{Ic}) yields a quantitative measure of a material's resistance to the initiation of unstable crack growth. This allows an estimation of critical crack sizes a component may withstand, given a service stress. Finally, the materials resistance to fatigue crack propagation will be measured as a function of either the linear elastic cyclic stress intensity factor range (ΔK and ΔK_{eff}) or the elastic-plastic cyclic J-integral range (ΔJ and ΔJ_{eff}). This material data allows life predictions to be made for known service conditions.

2.0 MATERIALS AND EXPERIMENTS

The primary material studied is Class L wheel steel. Large blocks from 5 to 12 inches along the tread, provided by the Department of Transportation (DOT), are sectioned from new and used 32 inch wheels. Conducted on this steel are metallographic, Gleeble hot compression, Rockwell B and C scale hardness (R_B and R_C), Knoop microhardness, tensile, Charpy (CVN) impact, plane strain fracture toughness (K_{Ic}), fatigue crack propagation and fractographic tests. For comparison, a 12 inch section of a new Class A wheel is also subjected to metallographic, R_B, R_C, and CVN testing. Wheel forging operations and heat treatments will impart non uniform mechanical properties throughout the wheel rim section. Results must be reconciled with specimen origins.

2.1 METALLOGRAPHY

At the Class A wheel tread surface, two metallography samples are oriented such that the planes of polish have normals along circumferential and transverse wheel axes (Fig. 2.1). Three rim interior samples, located approximately 1.5 inches from the tread surface, are each oriented with a wheel axis (Fig. 2.1). Five similarly oriented samples are sectioned from a new Class L wheel (Fig. 2.2). From a used Class L wheel, tread samples have transverse planes of polish and a fracture surface as one edge (Fig. 2.3).

All metallographic specimens are mounted in a thermosetting polymer powder using Struer's Prestopress-3 and Prontopress-2. Grinding follows the 240-320-400-600 grit sequence on a Leco VP-50 Vari/Pol or the 220-500-1200-4000 grit sequence on a

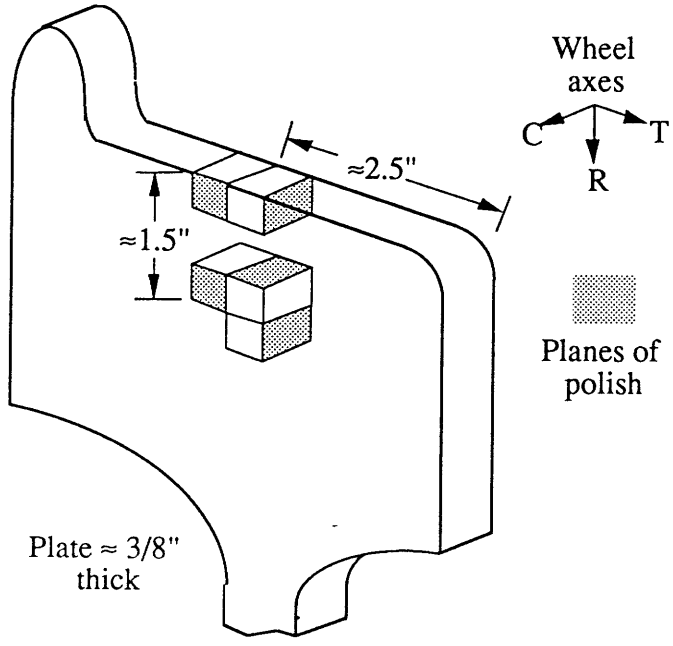

Fig. 2.1 The new Class A wheel metallography samples and the Rockwell hardness testing circumferential cross sectional plate.

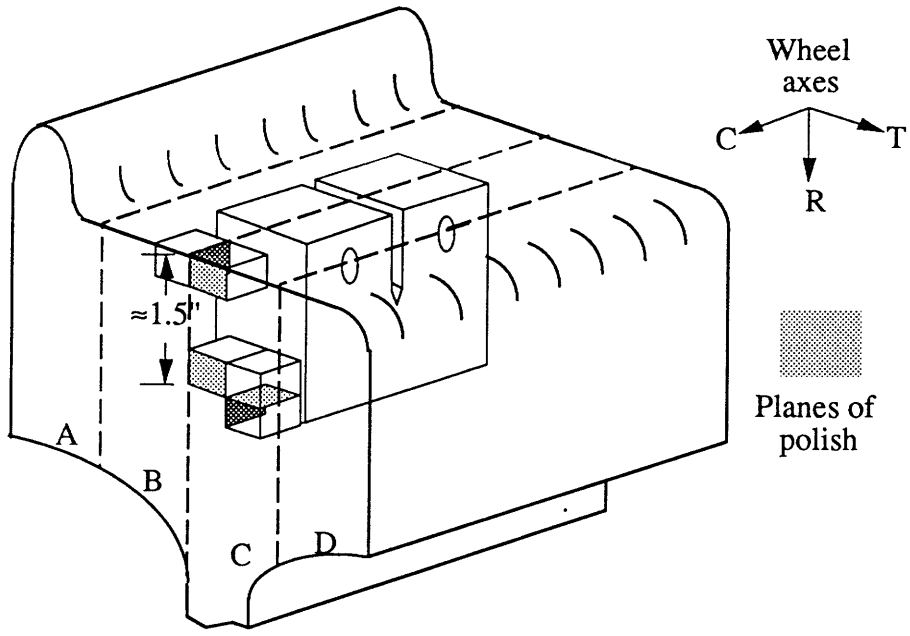

Fig. 2.2 A new Class L wheel block is sectioned into five metallography and eight compact tension specimens for plane strain fracture toughness testing. For fatigue tests, another block is machined into seven compact tension specimens having the orientation shown.

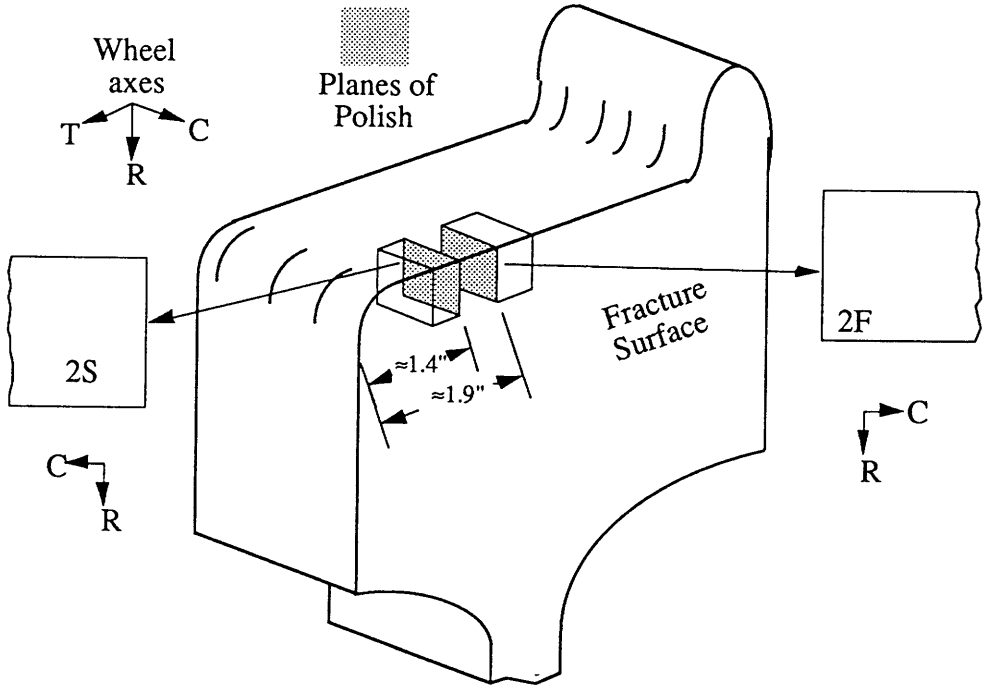

Fig. 2.3 Positions from within the fractured DOT Class L wheel block from which metallography samples 2F and 2S are removed.

Struer's Rotopol-1. Fine polishing following the Leco polisher is conducted by hand using 1.0, 0.3 and 0.05 micron alumina. Polishing after grinding on the Struer's machine, also by hand, requires only 0.05 micron alumina. Between polishing steps, samples are ultrasonically cleaned for 5 minutes using Struer's Metason 200. To reveal the grain structure, samples are immersed in either one or two percent nitric acid in alcohol (nital) solutions for 5 to 30 seconds. Following etching, samples are again ultrasonically cleaned for 15 minutes to completely remove any nital. Micrographs are taken either optically using Olympus Vanox or Nikon Optiphot microscopes or using Cambridge Instruments Stereoscan 250Mk3 scanning electron microscope (SEM). Micrographs used for metallography are taken at random locations from a sample's surface.

The technique specified in ASTM standard test method (STM) E112-88 determines the effective grain size (so termed because it determines the grain size for both phases simultaneously by treating them as a single phase) for the ferritic-pearlitic steels[20]. The average number of intercepts per mm and corresponding standard deviation (SD) are calculated from the summation of grain boundary intercepts of all individual test lines from all fields. The effective grain size is determined using this average while the range is determined by adding and subtracting the standard deviation from the average and redetermining the grain size. Consequently, the range of grain sizes may not center around the average.

ASTM STM E562-89 establishes the volume percent of ferrite[20]. The percentage of a 49 point grid falling on any single phase per field averaged over many fields directly gives the volume fraction. The 95% confidence interval ($CI_{95\%}$) determines the accuracy of an average with respect to the actual property value.

The technique established by Ridley measures interlamellar spacings[21]. The mean intercept spacing (s_I) between ferrite lamellae is measured by superposing straight lines at random orientations across micrographs taken of random pearlite colonies, s_I being the total line length divided by the number of intersected lamellae. Since this spacing is dependent upon the angle the lamellae intersect the plane of polish, the true interlamellar spacing (λ_o) is smaller. Ridley showed that $s_I=2\lambda_o$.

2.2 GLEEBLE TESTS

Testing by the Oregon Graduate Institute of Science and Technology involves hot compression of 21 specimens to various target strain values at temperatures above and below the eutectoid (1340°F) on a Gleeble 1500[22]. Specimens are removed from a used Class L wheel and machined into square prisms with dimensions of 5x10x20 mm (Fig. 2.4 (a)). Samples are resistance heated. Type K thermocouples percussion welded to the 5x20 mm surface monitor and control temperature. Hydraulic compression between 5

mm wide tungsten carbide anvils held in stainless steel jaws produces plane deformation through the 5 mm thickness (Fig. 2.4 (a) and (b)). An LVDT transducer measures the lengthwise displacements over the 20 mm gauge length. A strain rate of 100 mm/mm/second is maintained. This high strain rate requires blocks to arrest crosshead movement at the desired target displacement value. Data obtained during testing are plots of temperature and lengthwise strain versus time (Fig. 2.5 (a) and (b)). The actual thickness achieved is measured after testing and recorded as strain (Table 2.1).

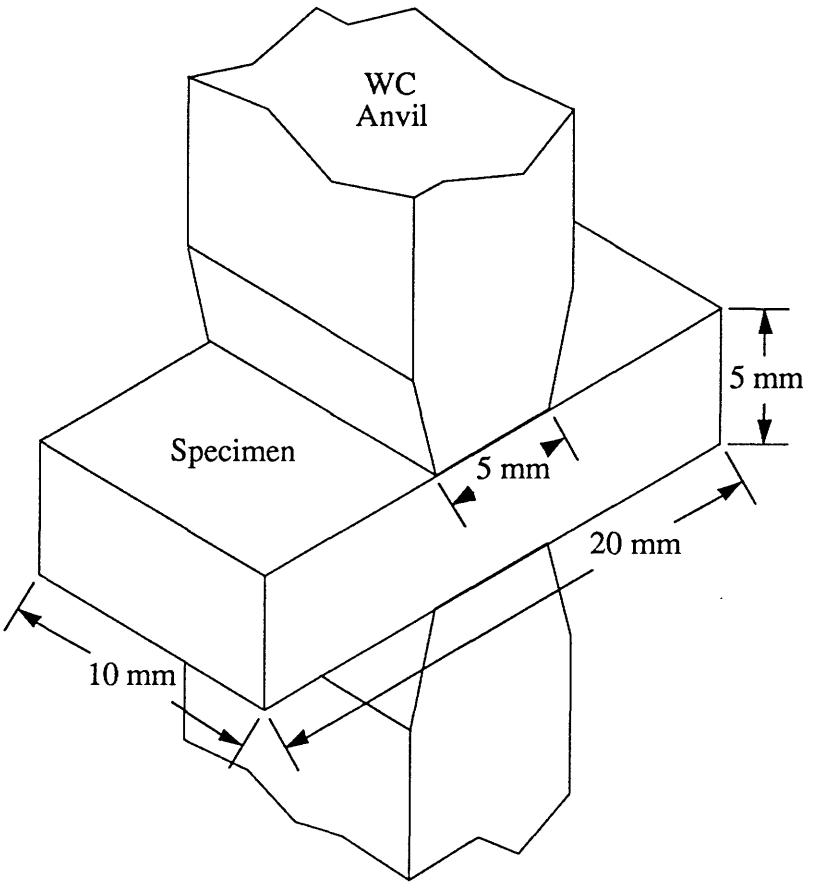

Fig. 2.4(a) Orientation and dimensions of Gleeble hot compression test specimens between tungsten carbide anvils.

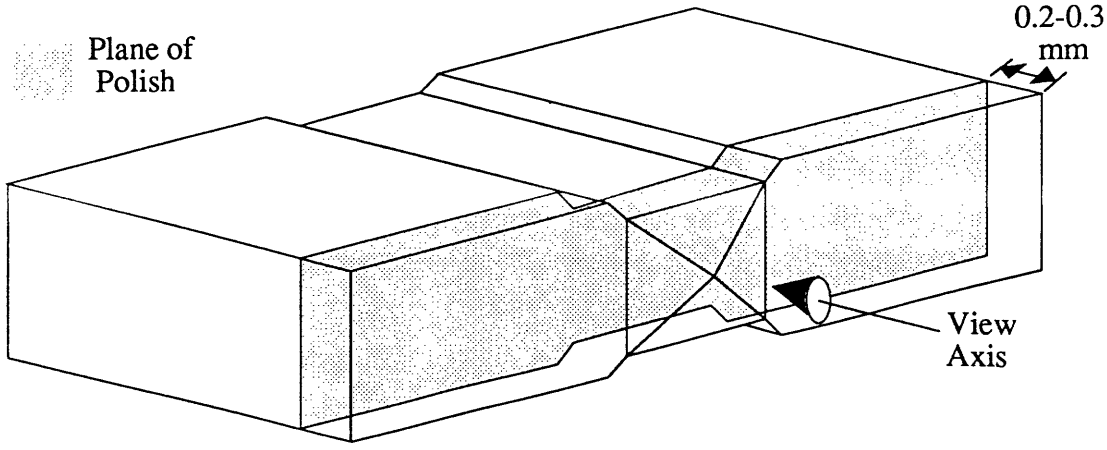

Fig. 2.4(b) Appearance of a Gleeble specimen after deformation.

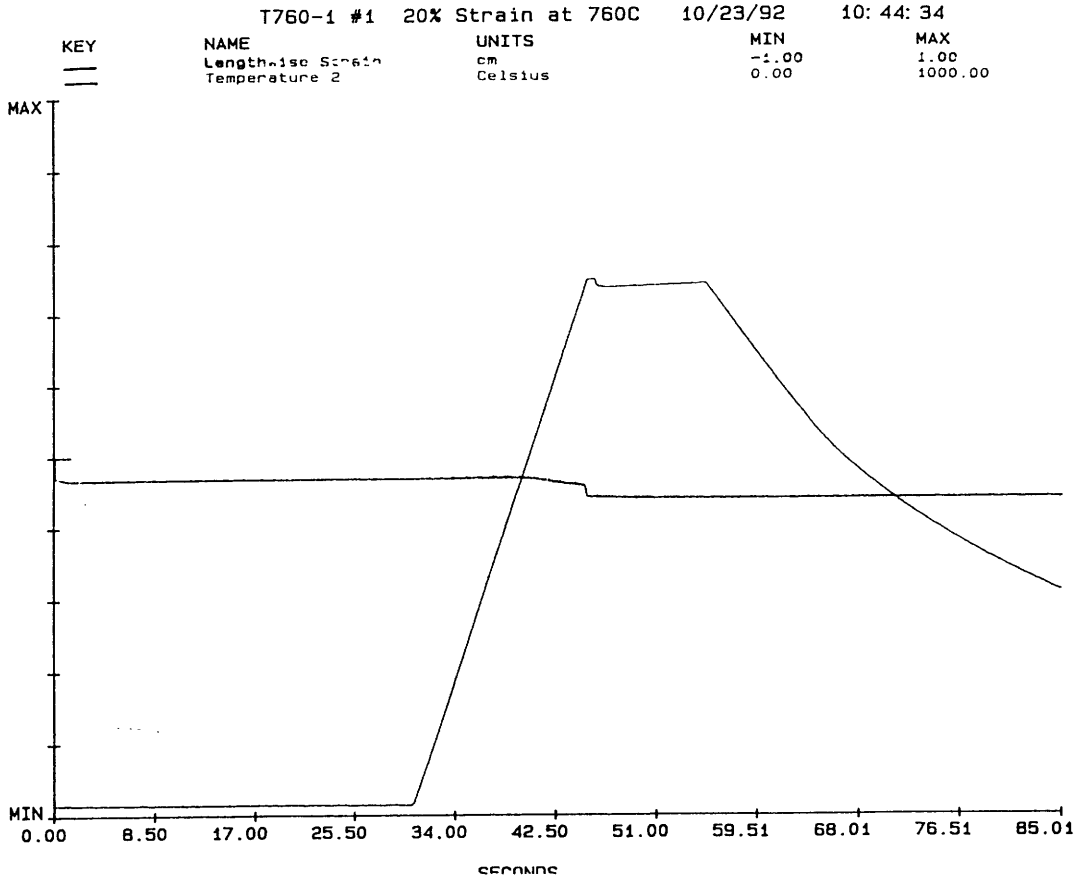

Fig. 2.5(a) Plot of lengthwise strain versus time produced for each specimen during hot compression.

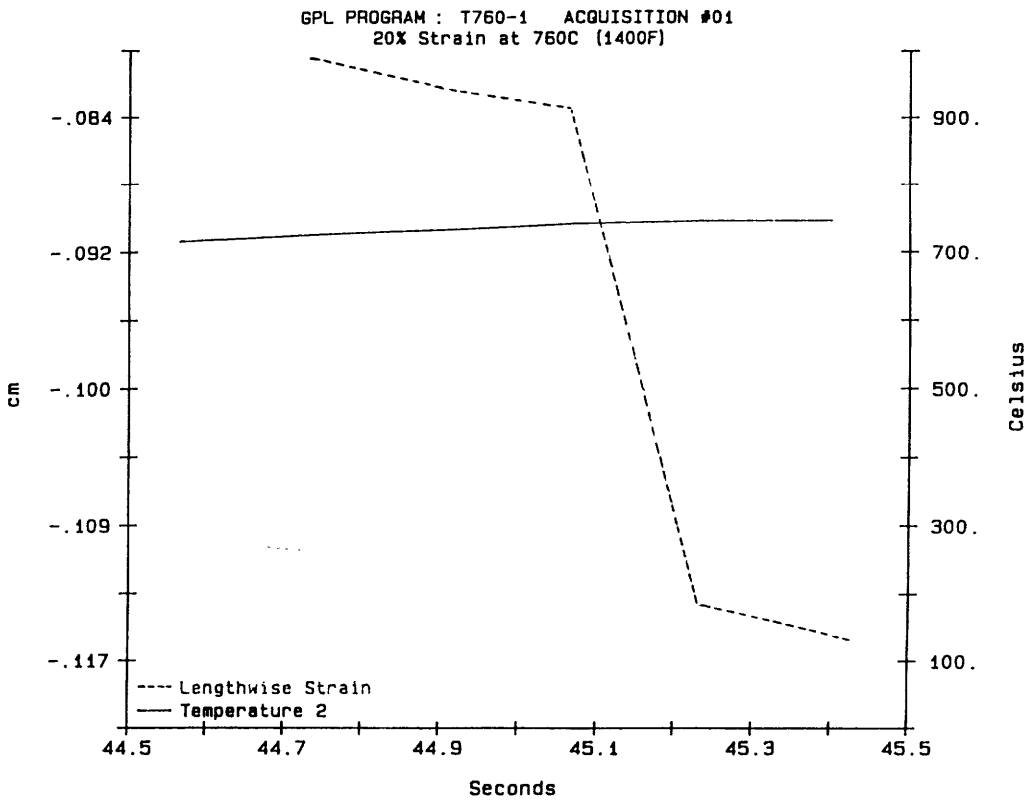

Fig. 2.5(b) The same plot as Fig. 2.5(a) expanding the compression region.

Table 2.1 Gleeble test matrix. SN stands for sample number, T is the test temperature (°F), te% is the target strain in percent and ae% is the achieved strain in percent.

SN	T°F	te%	ae%	SN	T°F	te%	ae%
760-1	1400	20	20.2	677-3	1250	5	21.2
760-2	1400	10	14.0	649-1	1200	20	21.2
760-3	1400	5	16.2	649-2	1200	10	6.1
760-4	1400	1	4.8	649-3	1200	5	13.1
732-1	1350	20	17.8	649-4	1200	1	1.6
732-3	1350	5	13.2	621-1	1150	20	15.6
704-1	1300	20	22.5	621-3	1150	5	4.8
704-2	1300	10	11.2	593-1	1100	20	15.6
704-3	1300	5	15.1	593-2	1100	10	5.4
704-4	1300	1	2.8	593-3	1100	5	3.4
677-1	1250	20	22.0	593-4	1100	1	21.8

After testing, samples are mounted, polished and etched as described in section 2.1. Low magnification optical macrographs of the etched surfaces are taken with a Nikon SMZ-10 stereo microscope illuminated by an Excel ring lamp. High magnification micrographs of the microstructure produced during hot compression are taken using both optical and scanning electron microscopes. Quantitative metallography of select micrographs is performed as described in section 2.1.

2.3 HARDNESS TESTS

2.3.1 KNOOP MICROHARDNESS TESTS

Knoop microhardness measurements are made in accordance with ASTM STM E384-89 using a Leco DM-400 tester and a 300 gram load[20]. All Gleeble specimens and the metallographic specimens 2F and 2S (Fig. 2.3) are tested. For Gleeble samples, indentations are made at two or more of the locations (A, B, C, G, H or J) specified in Fig. 2.6. These sites are chosen to include all microstructures formed during hot

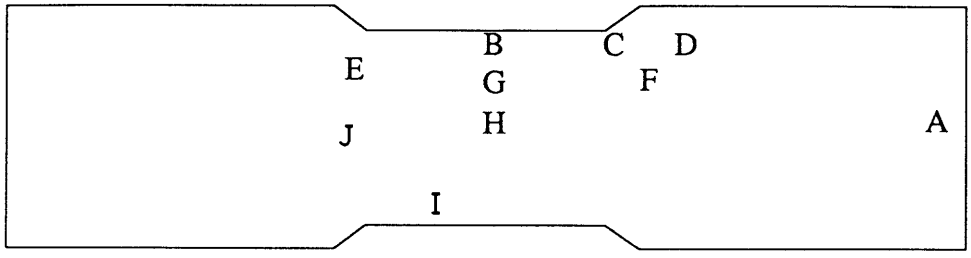

Fig. 2.6 Schematic of the plane of polish of a post-deformation Gleeble specimen. The letters denote cited photomicrograph and Knoop microhardness indentation locations.

compression and subsequent cooling during the Gleeble test. For samples 2F and 2S, indentation traverses are made across the transverse wheel plane (Fig. 2.7). For both samples, traverse 1 is along the rolling surface at a depth of 0.05 mm. For sample 2F, traverses 4 and 6 are at a depth of 0.05 mm from the fracture surface. The remaining traverses are perpendicular to either the rolling or fracture surfaces.

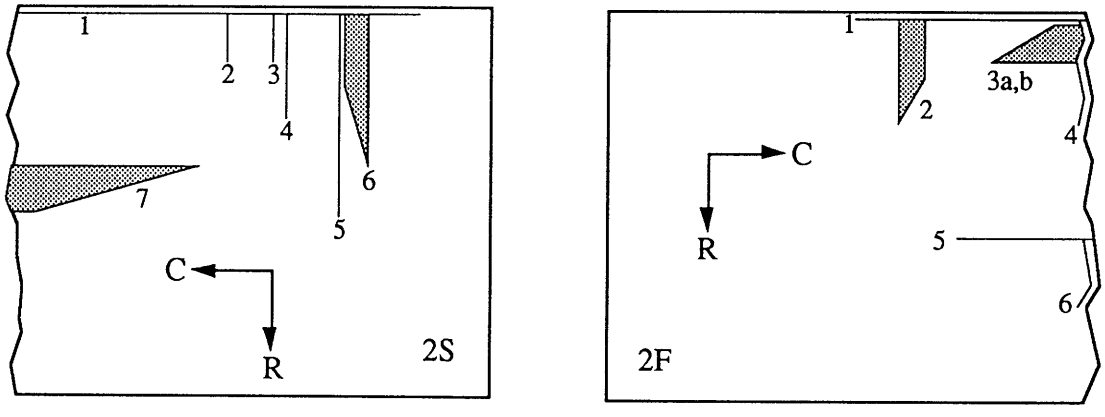

Fig. 2.7 Schematic of metallography samples 2F and 2S displaying the traverses of Knoop microhardness indentations made across each sample.

2.3.2 ROCKWELL HARDNESS TESTS

Rockwell hardness is measured in accordance with ASTM STM E18-92 using a Wilson tester[20]. New Class A and L wheels and a used Class L wheel are tested. Samples are cut from DOT wheel sections as circumferential cross sectional plates approximately 3/8" thick (Fig. 2.1). Smooth and parallel surfaces are obtained by grinding. A 1/2" by 1/2" grid is superimposed on the plate cross sections with the vertical lines parallel to the rim front edge and the horizontal lines parallel to the tread surface. Indentations are made at all intersections unless located too close to the plate edge.

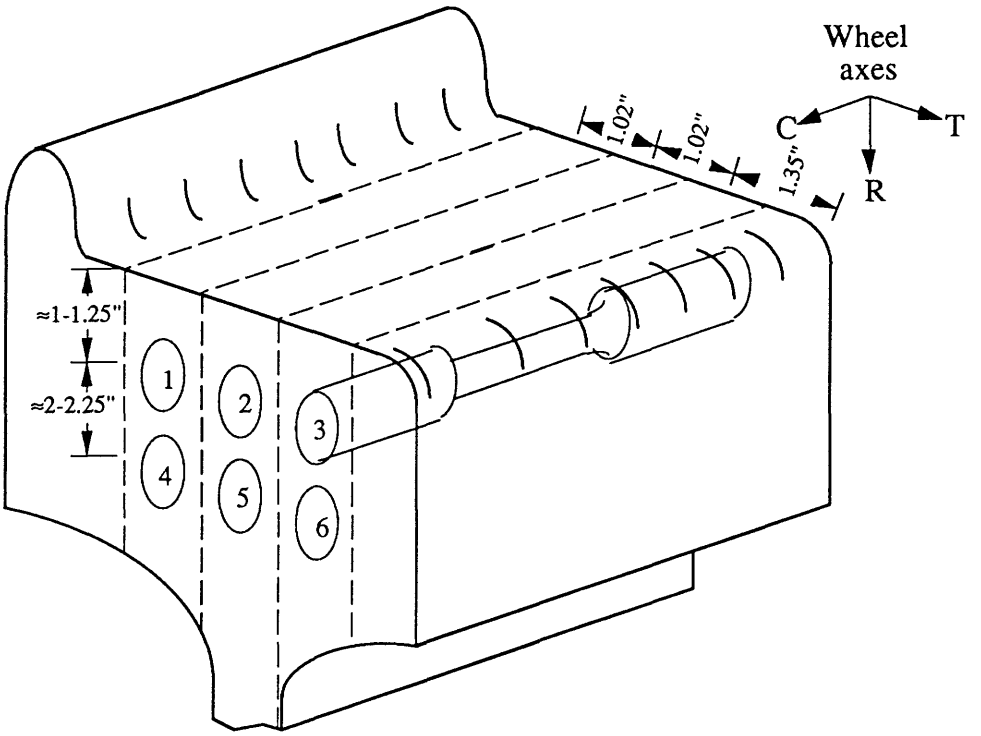

Fig. 2.8 Location and specimen numbers for new Class L wheel tensile tests.

2.4 TENSILE TESTS

A new Class L wheel section is cut into slabs as shown in Fig. 2.8. From the central three slabs are machined standard 0.5" diameter and 2" gage length tensile specimens as specified in ASTM STM E8-91[20]. The tensile axis coincides with the circumferential direction. Wheel curvature causes the reduced section of specimens 1, 2 and 3 to be approximately 1" from the tread and 2" for the rest.

Manlabs, the Testing Services Division of Altran Materials Engineering Incorporated, conducted the tests. An Instron 1332 servohydraulic load frame equipped with a 56 kip load cell and 8500 Series electronics applies load. An Instron 2620-825 extensometer output voltages converted into displacements by a Compaq PC running

Series IX software. The test is conducted in general agreement with E8-91[20]. Two samples are tested at each of three temperatures: samples 1 and 5 at 0°F, samples 3 and 4 at 70°F and samples 2 and 6 at 150°F. The test temperature is maintained by an Instron 3116 Environmental Chamber. Samples are exposed to the test temperature for 10 minutes prior to testing. The actuator displaces at 0.06 in/min until the onset of plastic strain and then increases to 0.10 in/min at which point the extensometer is removed. After removal of the extensometer, gage length displacements are extrapolated by a correlation between actuator and extensometer displacements established during the earlier part of the test.

2.5 CHARPY IMPACT TESTS

As shown in Fig. 2.9, DOT wheel sections are cut into approximately 1/2 inch thick slabs. Each slab yields one or two CVN specimens with standard dimensions set by ASTM STM E23-92[20]. The sample notches are machined such that the crack initiates in the circumferential plane and propagates in the radial direction (Fig 2.9) akin to cracks in used wheels. For the Class A wheel, 9 specimens are machined while 7 are machined for the Class L wheel. Samples are broken at 0, 70 and 150°F. Table 2.2 lists the sample numbers from Fig. 2.9 and the temperature at which they are tested. The testing is conducted at Manlabs in accordance with E23-92. Samples are cooled to 0°F by immersion in a bath of isopropyl alcohol and dry ice. Samples are warmed to 150°F with a Carbolite CSF 1200 oven. The samples are soaked at the test temperature for 15 minutes prior to fracture. The specimens are broken using two Physmet Charpy impact machines of the pendulum type. For the 0 and 70°F tests, the 24 ft-lb capacity machine is used. The 128 ft-lb capacity machine is used to determine if the 150°F tests require more than 24 ft-lbs to fracture the steel. Data is read directly from a machine as an angle and converted into CVN.

Table 2.2 Test matrix for Charpy impact specimens.

	Temperature		
	0°	70°	150°
Class A	1, 4, 7	2, 5, 8	3, 6, 9
Class L	3, 5, 7	1	2, 4, 6

2.6 PLANE STRAIN FRACTURE TOUGHNESS TESTS

A portion of a new wheel is cut into slabs approximately 1.25 inches thick (Fig. 2.2). These slabs are machined into one inch thick compact test specimens (Fig. 2.10) with a straight through notch oriented (Fig. 2.2) such that the normal to the crack plane is circumferential and the crack propagation direction is radial, away from the tread surface

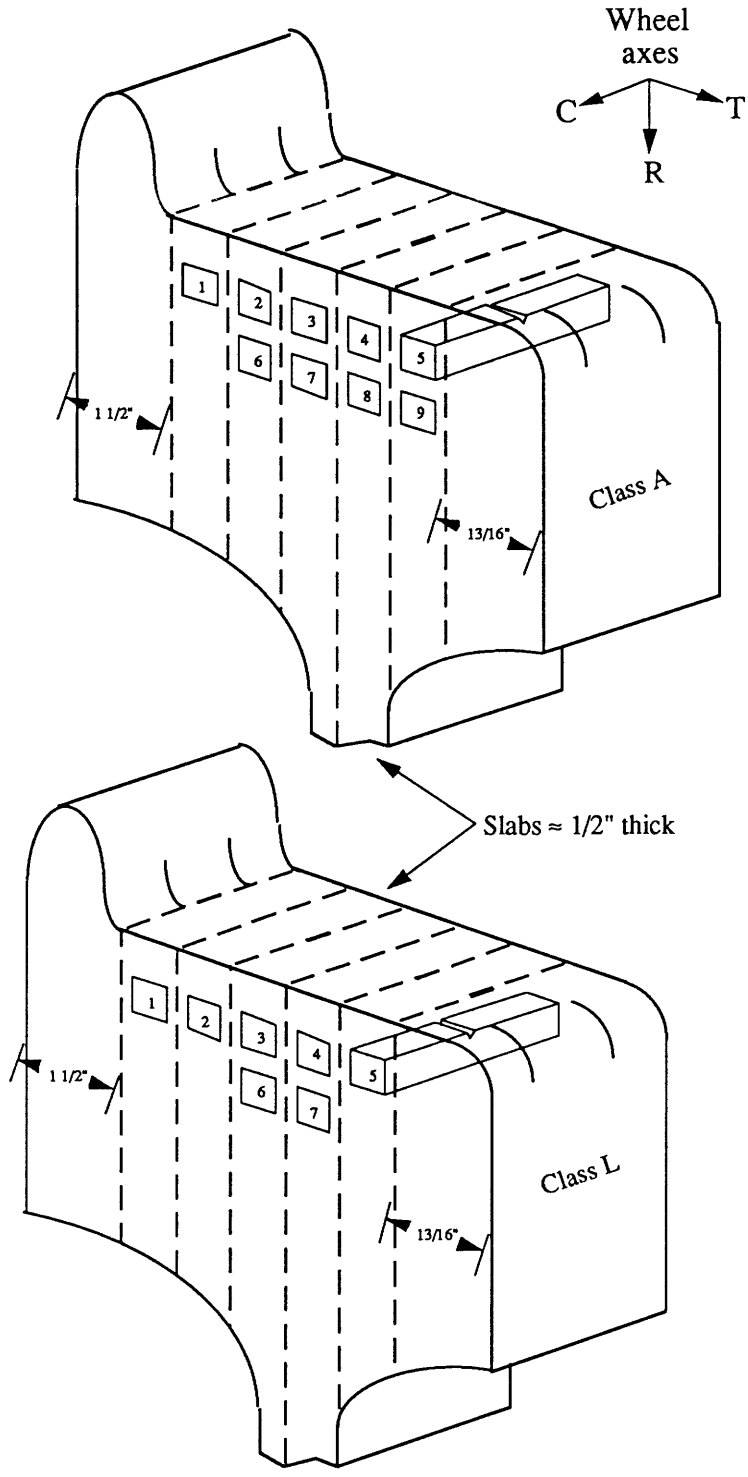

Fig. 2.9 Location and specimen numbers for new Class A and Class L wheel CVN tests.

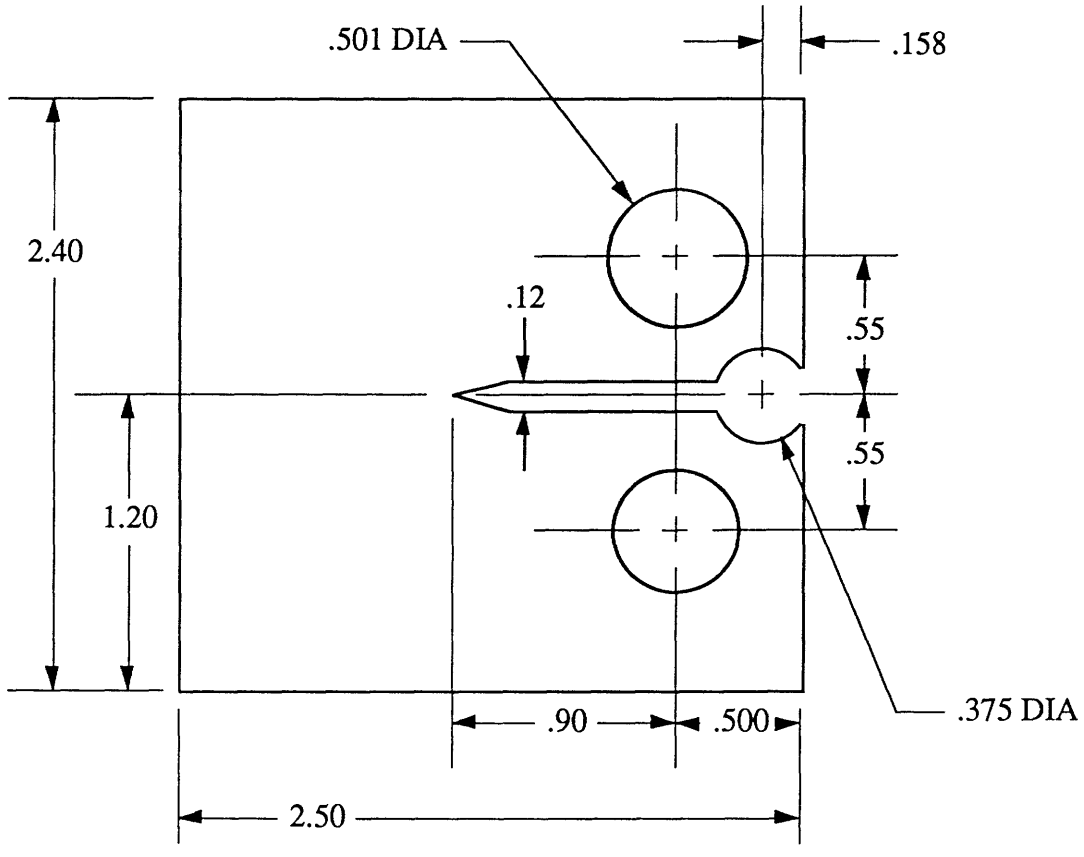

Fig. 2.10 Drawing of the 1" thick compact tension specimen used for plane strain fracture toughness testing. All dimensions are in inches. The machined starter notch has an included angle of 30° and the notch root radius is 0.015".

(ASTM specimen identification: C(T)(C-R)), corresponding to the orientation of fatigue cracks observed in damaged wheels[20]. Testing by Manlabs utilizes an Instron 1332 servohydraulic load frame controlled by a Compaq PC running the Falcon Suite program. The tests are run according to ASTM STM E399-90[20]. The specimens are precracked by fatigue in air, at room temperature and constant stress intensity (ΔK_{fat}) range between 22 and 30 ksi$\sqrt{in}$ (see Table 2.3). This produces a sharp fatigue crack approximately 0.1

Table 2.3 The test temperature (°F) and the fatigue precracking stress intensity range in ksi$\sqrt{in}$.

Sample	B2	A1	D1	D2	C1	C2
Temp °F	0	70	70	70	150	150
ΔK_{fat}	21.8	23.3	29.4	29.1	24.1	24.2

inch long extending from the machined notch. The fatigue precrack length is monitored by the COD measured by a double-cantilever displacement gage at the front face of the sample; ΔP is continuously decreased with increasing crack length to maintain ΔK_{fat}. The C(T)(C-R) specimens are then loaded to failure at a displacement rate of 0.001 inch

per second in air under position control. The attached displacement gage and load cell record load versus COD curves. Specimens are tested at 0, 75 and 150°F. The temperatures 0 and 150°F are controlled by Instron's 3116 Environmental Chamber (see Table 2.3 for testing parameters).

Following testing, the fatigue precrack length (a) is measured to within ±0.0001 inches at five positions along the crack front with a Gaertner Scientific traveling microscope. The conditional result load (P_Q) is determined according to section 9.1.2 of E399-90[20]. Knowing "a" and P_Q allows the conditional plane strain fracture toughness, K_Q, to be calculated by the equation given in E399-90 for C(T) specimens:

$$K_Q=\frac{P_Q}{B\sqrt{W}}\left(2+\frac{a}{W}\right)\left(1-\frac{a}{W}\right)^{-\frac{3}{2}}\left(0.886+4.64\frac{a}{W}-13.32\frac{a^2}{W^2}+14.72\frac{a^3}{W^3}-5.6\frac{a^4}{W^4}\right) \quad \text{eq. (2.1)}$$

where B is the specimen thickness and W is the width. K_Q is a valid K_{Ic} value if all the requirements of E399-90 are met. Finally, low magnification macrographs of the fracture surfaces are made using a Nikon SMZ-10 stereo microscope illuminated by the Excel ring lamp or directionally by an Ehrenreich MKII Fiber Optic Light. The final steps involve sectioning three samples, one for each temperature, for viewing the fracture features with the SEM.

2.7 FATIGUE CRACK PROPAGATION TESTS

2.7.1 HISTORY

Paris, Gomez and Anderson utilized linear elastic fracture mechanics (LEFM) to characterize the fatigue crack growth rate per cycle (da/dN) in metals with the cyclic stress intensity range (ΔK)[23]. Dowling and Begley first drew the analogy between LEFM and elastic-plastic fracture mechanics by characterizing da/dN with the cyclic J-integral (ΔJ) in gross plasticity experiments[24]. The utility of the cyclic J-integral is suspect as its validity is dependent upon proportional loading in the plastic zone of the crack tip[25, 26]. However, the cyclic J-integral remains constant through stress reversal and, excluding the first quarter cycle, can characterize fatigue crack growth[27].

Elber showed that the crack faces could come in contact during fatigue before zero load is reached[23]. When the crack tip closes before the minimum load is reached, the nominal crack driving forces (ΔK and ΔJ) may not determine the fatigue crack growth rate. Instead, the effective stress intensity factor range (ΔK_{eff}) or J-integral range (ΔJ_{eff}) defined over the range of loads where the crack faces are open is used. On the loading portion of the curve, the crack faces separate at the crack closure load (P_{cl}). This load is determined by comparing the compliance at successive points of the loading portion of the curve with the unloading elastic compliance of the previous cycle (Fig. 2.11)[28]. The

load at which these compliances are within ten percent of each other is defined as P_{cl}.

In contrast to ΔK_{eff}, calculation of ΔJ_{eff} requires the entire loading history for a cycle. This is because the J-integral is a measure of the amount of energy flow into the crack tip during crack extension. Thus, it is proportional to the area beneath the load-load line displacement curve. By using P_{cl} as the baseline of the P-COD curve rather than zero load or the minimum load to calculate ΔJ_{eff}, the crack driving force is attributed only to the portion of the loading cycle where the crack faces are open and not in contact.

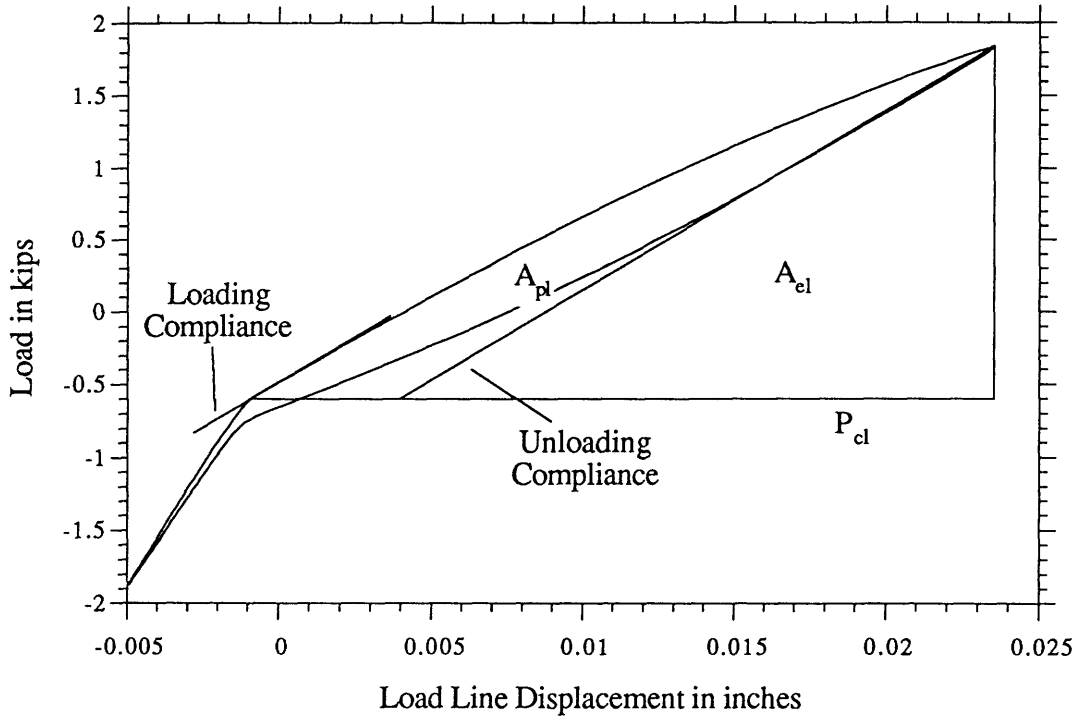

Fig. 2.11 The load-load line displacement curve for one cycle of a fatigue test.

2.7.2 TEST PREPARATION

A DOT Class L wheel section is cut into plates as shown in Fig. 2.2. One section yields seven plates (lettered A through G) able to be machined into side grooved C(T)(C-R) specimens with specifications as shown in Fig. 2.12. Following machining, each specimen's initial crack length, remaining ligament, thickness and net thickness (between side grooves) is measured to 0.0001" with the Gaertner Scientific traveling microscope. Testing is conducted at Instron Corporation on an Instron 8502 servohydraulic load frame using 8500 series electronics and controlled by the Advanced Fatigue Crack Propagation (AFCP) program run on a Compaq PC.

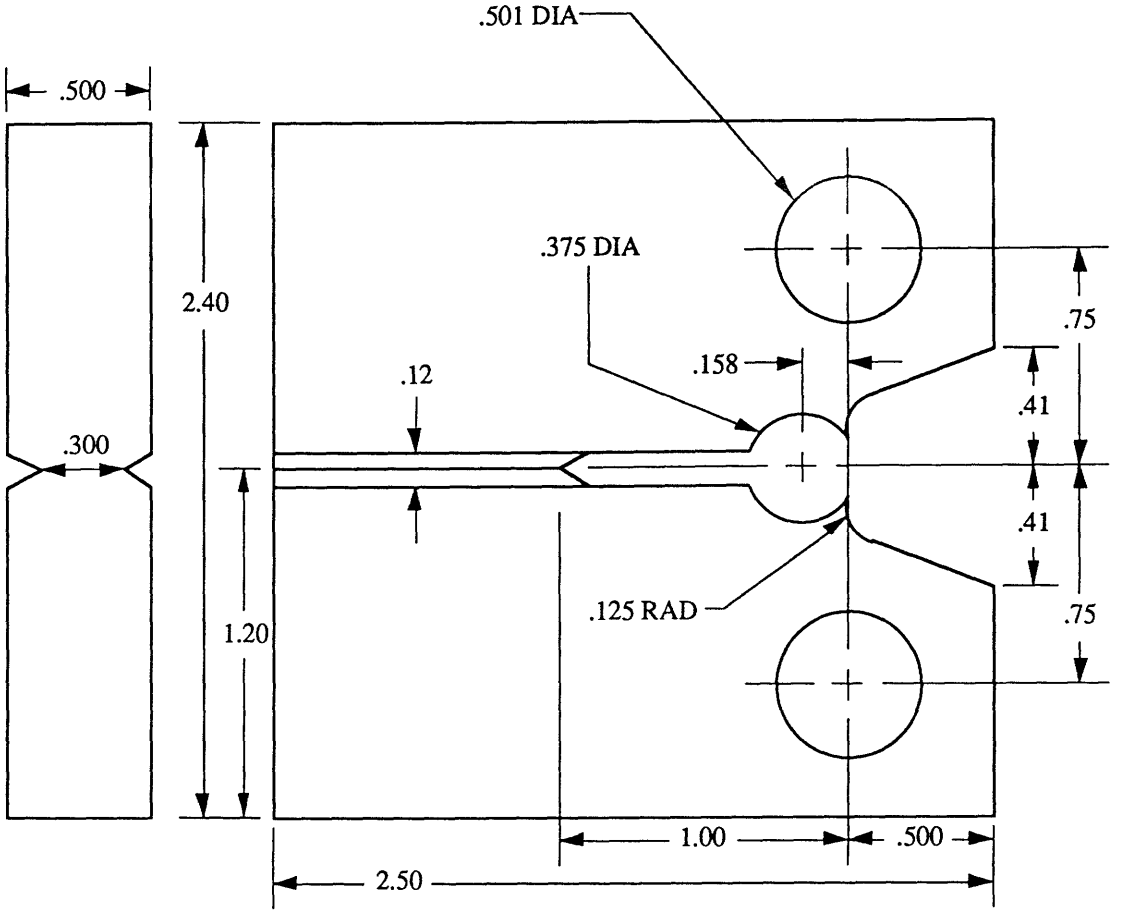

Fig. 2.12 The compact tension specimen used for fatigue crack growth rate testing. All dimensions are in inches. The machined starter notch has an included angle of 60° and radius of curvature of 0.015" and the mouth opening for the COD gage is angled at 20°.

The AFCP program was developed at Instron and measures the crack propagation rate (da/dN) as a function of either ΔK, ΔK_{eff}, ΔJ or ΔJ_{eff}[28]. Raw data is gathered by the computer in the form of load line COD and load (P) signals during runtime from the series 8500 electronics. For each cycle, a set of 200 P-COD pairs are recorded. Saxena and Hudak formulated normalized elastic compliance (ECB) expressions as functions of normalized crack length (a/W) for C(T) specimens[29]. Jablonski, et. al., showed that a/W as a function of ECB can be determined from established COD-a/W relationships or the stress intensity factor[30]. The AFCP program uses the relationship:

$$\frac{a}{W} = 1.0002 - 4.0632U + 11.242U^2 - 106.04U^3 + 464.33U^4 - 650.68U^5 \qquad \text{eq. (2.2)}$$

to determine the crack length[30]. U is a function of the normalized compliance given by:

$$U = \frac{1}{1+\sqrt{E'CB_{eff}}} \qquad \text{eq. (2.3)}$$

$E'=E/(1-\nu^2)$ is the plane strain elastic modulus and B_{eff} is the effective thickness:

$$B_{eff}=B-\frac{(B-B_{net})^2}{B} \qquad \text{eq. (2.4)}$$

The gross specimen thickness is B and the net thickness (B_{net}) is the reduced thickness between the side grooves. The specimen compliance (C) in the above equations is determined by a linear regression of the elastic unloading portion of the P-COD hysteresis loops.

All samples are precracked as mandated in ASTM STM E647-91 prior to any ΔK_{eff} or ΔJ_{eff} control fatigue testing[20]. The precracking ΔK is maintained at 26 ksi$\sqrt{in}$ with R of 0.1. Precracking is halted at a crack length of 1.100".

Crack lengths are verified using an Omniphot traveling microscope. The maximum load for the last precracking cycle is manually applied by slowly increasing the load set point. The sample is then cycled, a maximum of 15 times, between the maximum load, usually around 1.4 kips, and a lower load, about 1 kip. This distinguishes the crack tip and enables the crack length to be measured easily. The sample is then cycled in load control with ΔP=0.6 kips and R=0.4 by the AFCP program while the Young's modulus (E) is varied until the compliance crack length calculated by the computer (a_{cmpl}) matches the crack length measured with the traveling microscope ($a_{\mu scope}$). E may differ from that measured in a tension test by ten percent and still meet the E647-91 standard[20]. After the proper E is determined, the robustness of the compliance technique for measuring crack length is verified. This consists of cycling at various ΔP and R combinations to see if a_{cmpl} remains constant. This occurs when the maximum load (P_{max}) during cycling is approximately 0.6 kips or greater and the compliance window is set for 65-98% of P_{max}. The compliance window, set by the user, is the portion of the unloading curve which is linearly regressed to give the compliance.

2.7.3 RISING ΔK_{eff} FATIGUE TESTS

When running a rising ΔK_{eff} test, the computer runs the system in load control according to the equation:

$$\Delta K_{eff}=\Delta K_o \exp[C_g(a_{cmpl}-a_o)] \qquad \text{eq. (2.5)}$$

The constant ΔK_o is the initial stress intensity range for the test when the crack is a_o long and C_g gives the rate of increase of ΔK_{eff}. For each cycle, the computer must adjust the output from the waveform generator such that the achieved load amplitude meets that determined by eq. (2.5) and the specified R ratio. The conditions for all rising ΔK_{eff} tests are listed in Table 2.4.

Table 2.4 Test matrix for rising ΔK_{eff} tests. ΔK_o values are in ksi$\sqrt{in}$. C_g and R are dimensionless constants. Frequency is in hertz. E in ksi is the Young's modulus entered into the computer such that a_{cmpl}=$a_{\mu scope}$. All tests are stopped prior to the initiation of unstable crack propagation at the a_{cmpl} listed in Test End.

Sample	a_o	ΔK_o	C_g	Freq.	R	E	Test End
A	1.147"	30	4.76	0.5	-1	30500	1.382"
B	1.126"	28	3.50	1.0, 0.5	-1	29000	1.410"
E	0.025"	1.5	3.00	0.5	-1	30000	1.300"
F	0.025"	1.5	3.00	0.5	-0.5	32000	1.300"

2.7.4 RISING ΔJ_{eff} FATIGUE TESTS

The equation used to calculate ΔJ_{eff} is identical to that used to calculate the J-integral for a J_{Ic} test given in ASTM STM E813-89[20]:

$$\Delta J_{eff} = \frac{(\Delta K_{eff})^2(1-\nu^2)}{E} + \frac{A_{pl}\left(2+0.522\frac{W-a}{W}\right)}{B_{net}(W-a)} \qquad \text{eq. (2.6)}$$

The difference is the substitution of ΔK_{eff} for K and the plastic area (A_{pl}) shown in Fig. 2.11. A_{pl} for ΔJ_{eff} is defined as the area between the P-COD curve and the elastic unloading compliance line that lies above P_{cl} (Fig. 2.11).

During a rising ΔJ_{eff} test, the computer runs the system hardware in COD control according to the equation:

$$\Delta J_{eff}=\Delta J_o \exp[C_g(a_{cmpl}-a_o)] \qquad \text{eq. (2.7)}$$

The constants serve the same purpose as in eq. (2.5). Since in load control, the computer adjusts the waveform generator such that the achieved COD amplitude gives the proper ΔJ_{eff} demanded by the conditions set by the current crack length and eq. (2.7). The conditions for all rising ΔJ_{eff} tests are listed in Table 2.5.

Table 2.5 Test matrix for rising ΔJ_{eff} tests. ΔJ_o values are in ksi·in. Frequency is in hertz. C_g is a dimensionless constant. E in ksi is the Young's modulus used during testing to match a_{cmpl} and $a_{\mu scope}$. Test End lists crack lengths at which tests are stopped due to unstable crack propagation. The asterix indicates the control parameters are changed to the next line at the a_{cmpl} listed.

Sample	a_o	ΔJ_o	C_g	Freq.	E	Test End
D	1.098"	0.025	7.62	0.5	27300	1.136" *
			8.50			1.371"
E	1.300"	0.165	3.76	0.1	30000	1.452"
F	1.295"	0.145	2.50	0.1	32000	1.506"
G	1.135"	0.047	6.77	0.1	31500	1.351" *
	1.350"	0.200	2.72	0.05		1.427" *
	1.425"	0.245	1.72			1.497"

Following testing, the samples are placed in liquid nitrogen and the remaining ligament was fractured to reveal the fracture surface. The specimens are then sectioned so that the fracture surface can be viewed in the SEM.

3.0 EXPERIMENTAL RESULTS

3.1 METALLOGRAPHY

Characteristic of hypoeutectic steels, the microstructures of Class A and L wheel steels contain the micro-constituents ferrite and pearlite. The visual appearance of their microstructures comprise patterns of the micro-constituents indicative of the cooling history. Upon cooling from the austenite phase field, ferrite will nucleate and grow along austenite grain boundaries with a blocky allotriomorph (GBA) morphology[31]. Pearlite colonies form from the remaining austenite when the eutectoid temperature is reached and is enveloped by the ferrite GBA. This pattern is found in all micrographs presented with few exceptions. Using the lever rule and the equilibrium phase diagram, the volume percent of ferrite (V_α) can be calculated for different carbon compositions[32]. For Class A steel having compositions between 0.47 and 0.57 w/o C, corresponding V_α should be between 40 and 27%. For Class L steel, the composition is a maximum of 0.47 w/o C. It will be assumed that the lower bound of the carbon content is 0.37 w/o. This gives V_α between 53 and 40%.

3.1.1 MICROSTRUCTURES OF CLASS A AND L STEELS

Metallographic examination of the rim interior samples removed from new Class A and L wheels (Figs. 2.1 and 2.2) reveals both to be equiaxed with respect to the principal axes of the wheel. Fig. 3.1 displays representative micrographs of the ferritic-pearlitic microstructure of the two steels. The grain size (G) and V_α are given in Table 3.1. The point count method measured V_α in both steel classes to be far lower than that

Table 3.1 ASTM effective grain sizes and volume percent ferrite of rim interior samples of Class A and L steel. Values are given as averages ± SD or $CI_{95\%}$ with the corresponding RAC.

	New Class A	New Class L	Used Class L
V_α	23.3%	18.3%	30.6%
$\pm CI_{95\%}$	±2.70%	±2.15%	±2.6%
RAC	11.6%	11.7%	8.6%
ASTM G	9.1	8.3	9.0
±SD	+0.4-0.6	+0.5-0.7	±0.3
RAC	5.2%	6.4%	9.5%

predicted from the equilibrium diagram. The interlamellar spacing of the Class L steel is 0.436 microns with a 95% confidence interval, $CI_{95\%}$, of 0.072 microns and relative accuracy, RAC, of 16.6%. For the Class A steel, the spacing is 0.405 microns, $CI_{95\%}$=0.034 microns and RAC=8.8%.

(a)

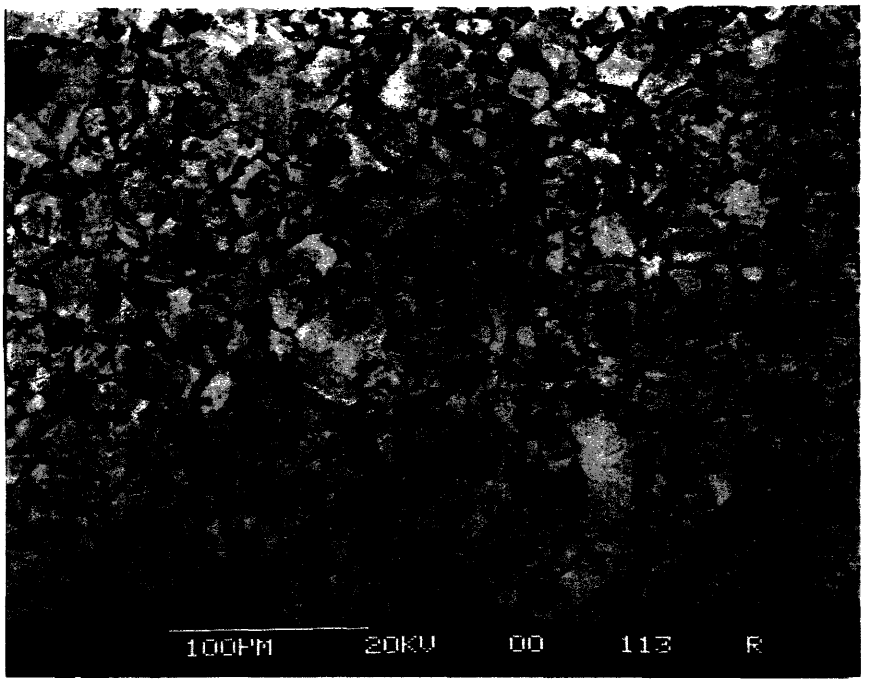

(b)

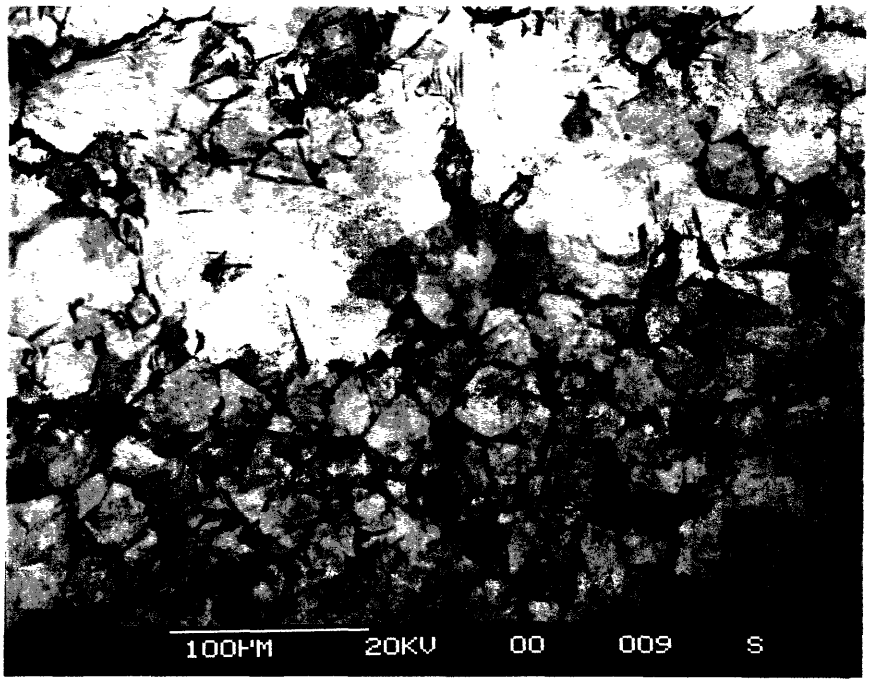

Fig. 3.1 Representative microstructures of new Class A (a) and Class L (b) wheel steels. Micrographs taken approximately 1.5" from tread surface of the circumferential plane at 250x.

The used Class L microstructure (UL) is shown in Fig. 3.2. This is a photomicrograph of Gleeble sample 593-3. It is assumed to accurately represent the microstructure present in used Class L wheels despite its origins; specimen 593-3 was heated to 1100°F and strained 0.8 percent, however, the micrograph location was far

removed from any deformation (area A of Fig. 2.6). A comparison of new Class L and UL microstructures shows that the arrangement of the micro-constituents remains similar to that descibed above. Data in Table 3.1 show that service changes the microstructure considerably. Upon use, the grain size will decrease and the amount of ferrite increase.

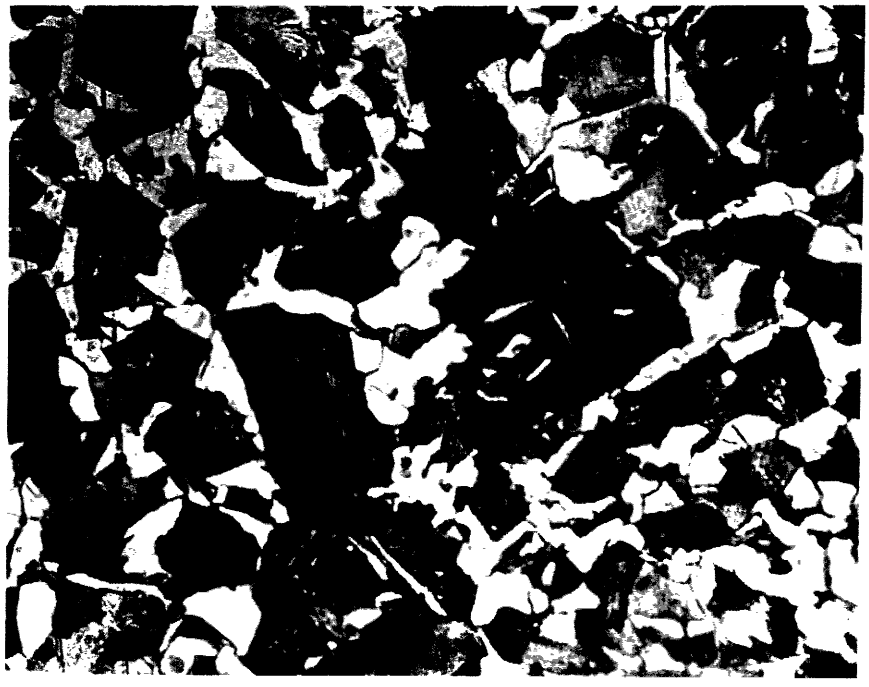

Fig. 3.2 The used Class L microstructure. Micrograph taken from Gleeble specimen 593-3, deformed at 1100°F to 3.4% total strain taken from area A of Fig. 2.6 at a magnification of 400x (abbreviated format: 593-3, 1100°F, 3.4%e, A, 400x).

3.1.2 GLEEBLE SPECIMENS

Etching the Gleeble specimens reveals three distinct patterns discernible to the naked eye. Macrographs of the patterns, or macrostructures, are presented in Figs. 3.3 through 3.5. In Fig. 3.3, no pattern appears before or after deformation. This is the as-received (A) macrostructure. In Fig. 3.4, material stressed by the anvils is lighter than uncompressed material of the specimen's ends. This is the stressed (S) macrostructure. In Fig. 3.5(a), the pattern appears as a cross connecting opposite anvil edges. This is the X macrostructure. Although it did not photograph well, it is schematically represented in Fig. 3.5(b).

Gleeble specimens possess the UL microstructure of Fig. 3.2 prior to testing. After compression, etching resolves four distinct zones in all samples, the introduction and discrimination of which will be covered here. In some samples, the region stressed by the anvils has grains (Fig. 3.6) similar to UL. These grains constitute the deformed

Fig. 3.3 The A macrostructure of 593-3, 1100°F, 3.4%e, all, 15x.

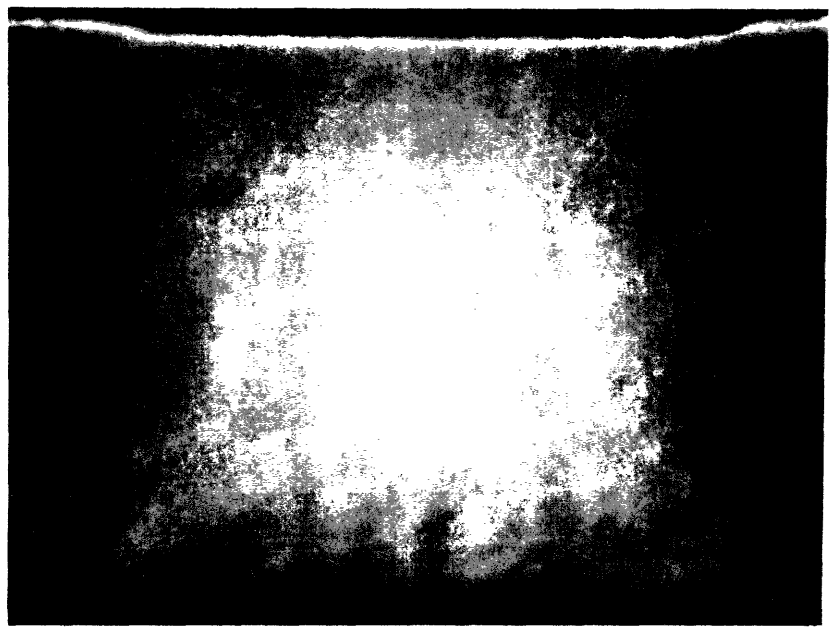

Fig. 3.4 The S macrostructure of 593-2, 1100°F, 5.4%e, all, 15x.

Class L microstructure (DL). Comparing Fig. 3.6 with Fig. 3.2 shows the similarity in grain sizes of DL and UL microstructures. In conjunction with the micrographs, data in Table 3.2 elucidates the differences: V_α decreases ten percent and the pearlite enveloping nature of the ferrite is more distinguished in the DL microstructures. The highly sheared microstructure (HS) is shown in Fig. 3.7. These grains appear to have the size of UL and DL grains although direct measurement is impossible due to their elongation. Also,

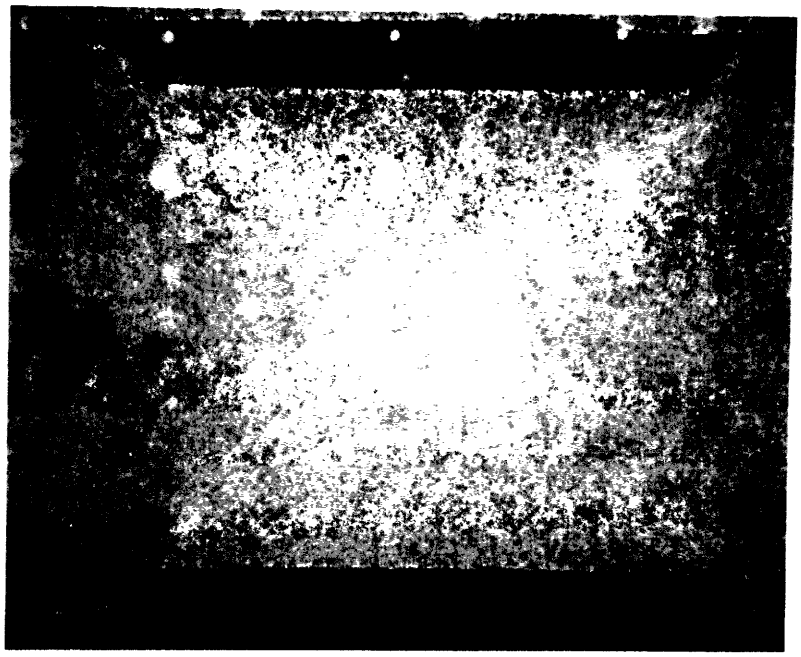

(b)

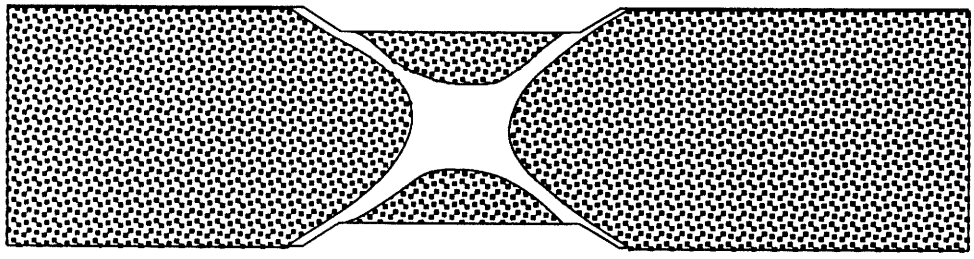

Fig. 3.5 (a) The X macrostructure of 593-1, 1100°F, 15.6%e, all, 15x. (b) Schematic depicting pattern in (a) which does not photograph well.

Table 3.2 Volume percent ferrite and ASTM effective grain size for each Gleeble microstructure. Error is given by $CI_{95\%}$ or SD.

	UL	DL	HS	PT	FR
Sample	593-3	593-1	593-1	760-2	760-2
V_α $\pm CI_{95\%}$ %RA	30.6 ±2.6 8.6	20.3 ±4.7 23.1	15.5 ±3.2 20.4	48.9 ±3.9 8.0	62.1 ±1.9 3.0
ASTM G ±SD %RA	9.0 ±0.30 9.5	Same as UL	Elongated	11.85 +0.35-0.40 8.2	13.10 +0.35-0.40 11.1

ferrite still surrounds pearlite but V_α decreases to a low value of 15.5%. A striking contrast of others, the partially transformed microstructure (PT) is displayed in Fig. 3.8. PT grains show a breakdown of pearlite. Instead of ferrite GBA surrounding pearlite, small grains of both ferrite and pearlite exist, reducing the ASTM effective grain size to 11.85. Unlike DL and HS, V_α in the PT microstructure increases over the UL value to

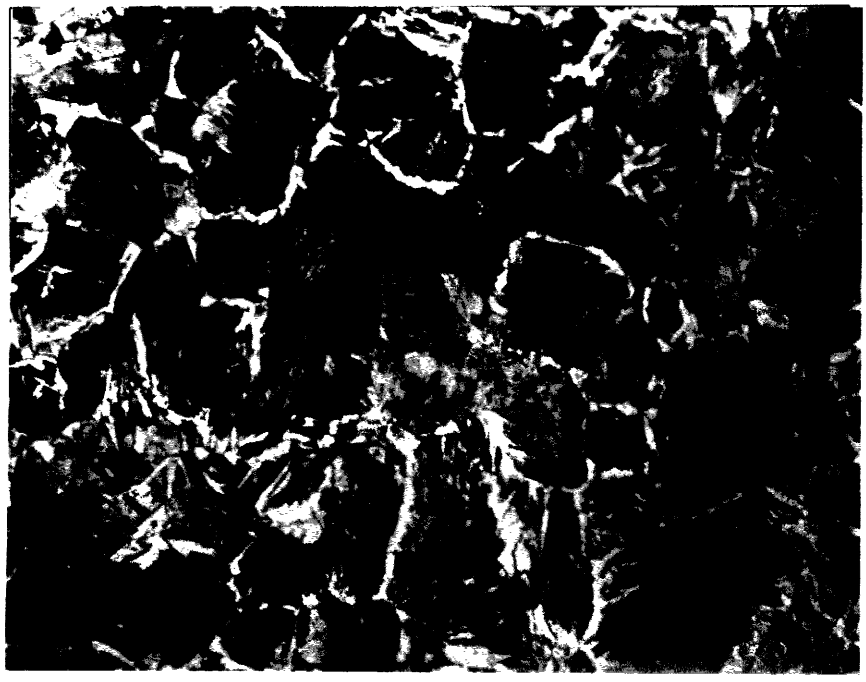

Fig. 3.6 The DL microstructure of 593-1, 1100°F, 15.6%e, B, 400x.

48.9%. This is within the range predicted by the use of the lever rule. Finally, the fully recrystallized microstructure (FR) appears in Fig. 3.9. FR grains significantly decrease the grain size with respect to UL, shrinking to an ASTM effective size of 13.1. Ferrite grains are equiaxed, do not surround pearlite and comprise more of the volume than equilibrium predictions at 62.1%.

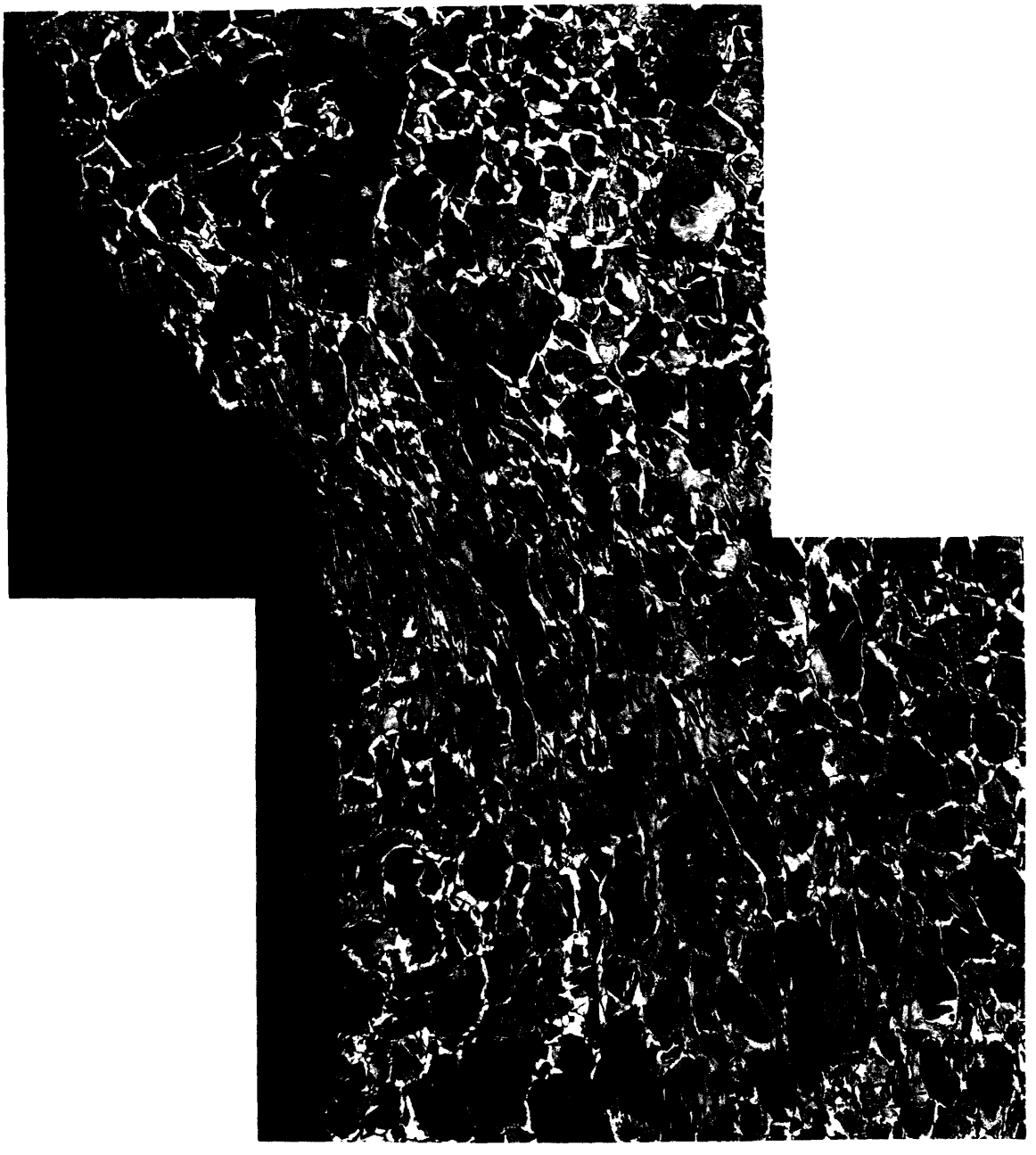

Fig. 3.7 Composite micrograph of the HS microstructure, sheared along the plane of maximum shear. 649-3, 1200°F, 13.1%e, C, 165x.

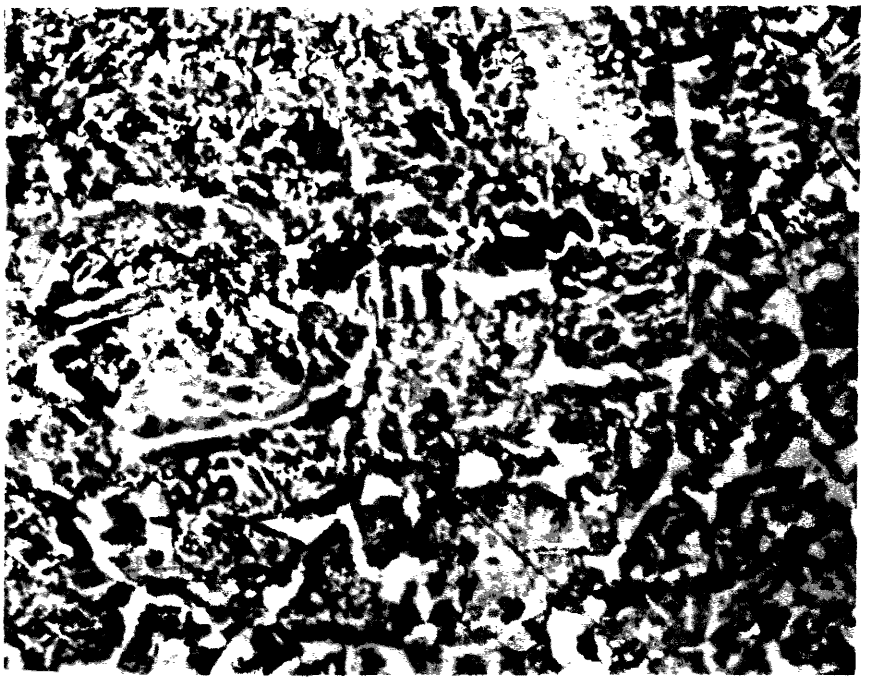

Fig. 3.8 The PT microstructure of 760-2, 1400°F, 14.0%e, D, 400x.

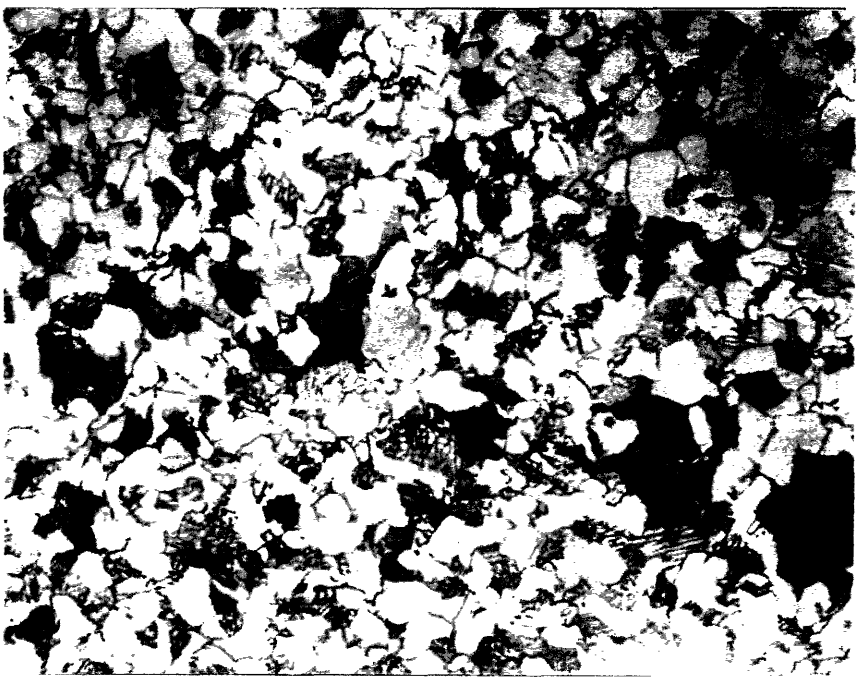

Fig. 3.9 The FR microstructure of 760-2, 1400°F, 14.0%e, F, 1000x.

3.2 HARDNESS

3.2.1 KNOOP MICROHARDNESS

Further microstructural discrimination is provided by the hardnesses of the various grains. Testing ranks the grains formed during the Gleeble test, in descending order of hardness, to be HS, FR, DL, UL and PT. Average Knoop microhardness numbers (HK_{300}) are given in Table 3.3.

Table 3.3 Average Knoop microhardness numbers (HK_{300}) in kgf/mm^2 measured for each grain. Error is given by the $CI_{95\%}$, also in kgf/mm^2. Location refers to the specimen region of Fig. 2.6 from which data was collected.

	UL	DL	HS	PT	FR
Location	A	B, H, J	C	G, H, J	H
HK_{300}	257.2	268.6	276.0	250.5	273.8
$\pm CI_{95\%}$	±7.5	±5.4	±8.8	±8.8	±25.5
RAC	2.9%	2.0%	3.5%	3.5%	9.3

The remaining Knoop microhardness results appear as graphs in the appendix of the traverses made across the used Class L wheel metallography samples and are summarized here in Table 3.4. Traverse nomenclature follows the E399-90 convention; the first two letters denote the surface at which the traverse is made, either TS for tread surface or FS for fracture surface, followed by letters denoting the plane and direction in which the traverse is made (e.g. in Fig. A1, the traverse is along the tread surface in the circumferential direction within the HAZ on the transverse plane and is traverse TS(T-C)). Average values for these traverses appear in Table 3.4. The average for traverse TS(T-R) excludes values within the HAZ (indentations closer than 0.36mm to the tread).

Table 3.4 Average values for Knoop microhardness traverses made on the transverse plane of a fractured Class L wheel.

Traverse Fig.	TS(T-C) 3.10	TS(T-R) 3.11	FS(T-R) 3.12	FS(T-C) 3.13
avg. HK_{300}	360.7	343.8	355.8	345.3
SD	41.2	28.5	43.4	28.3
$CI_{95\%}$	8.9	5.3	17.2	5.5
RAC	2.5%	1.5%	4.8%	1.6%

3.2.2 ROCKWELL HARDNESS

The results of R_B and R_C measurements made on cross-sectional plates of new Class A and L wheels appear in Fig. 3.10 while Fig. 3.11 shows the results of R_C measurements made on the used Class L wheel. In new wheels, the hardest material is found near the top of the flange back. The hardness across the tread is lower by 5.4% in

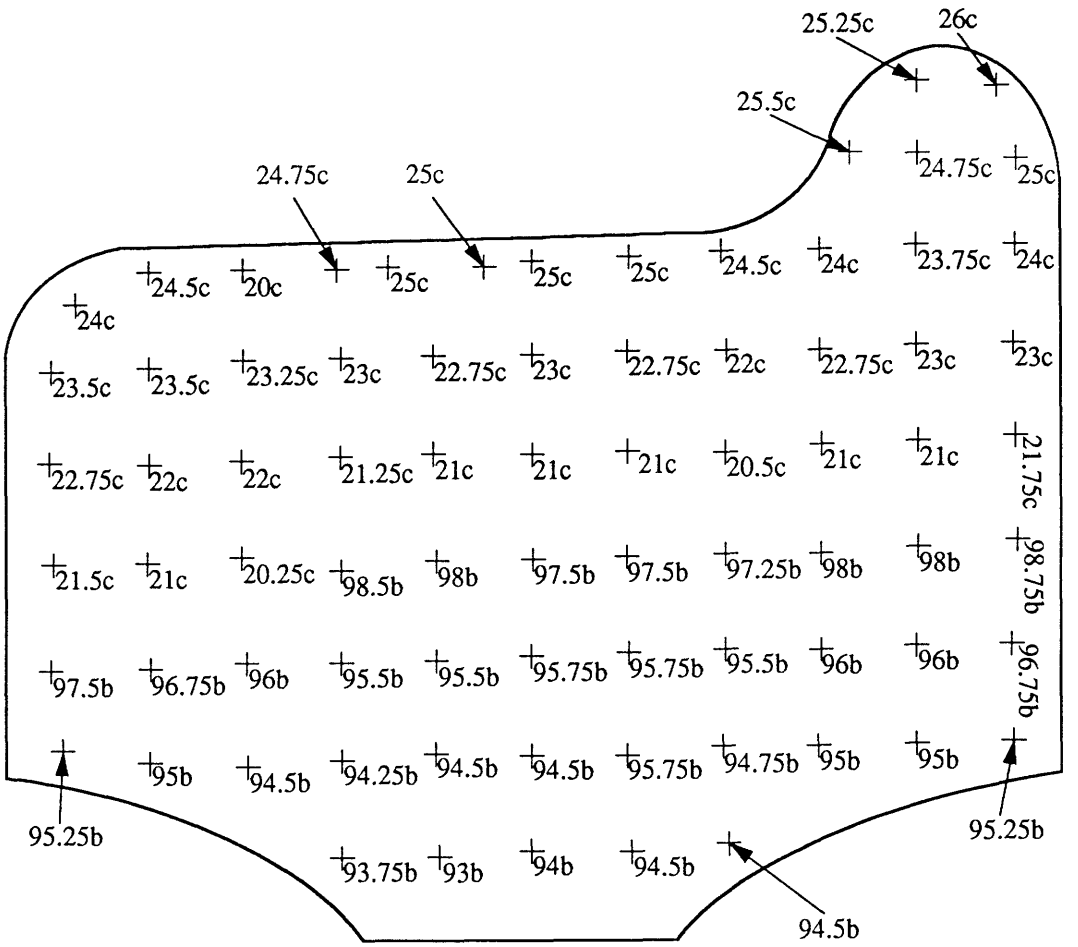

Fig. 3.10(a) The Rockwell B and C scale hardness profile of the circumferential plane of a new Class A wheel. Letters following numbers denote scale used.

the Class A section and 8.7% in the Class L section and decreases continuously through the rim section to 52 and 38% of the flange maximums, respectively, in Class A and L at the plate. The Class A wheel is harder than Class L to approximately 1" in depth from the tread surface. Through the remainder of the rim section, Class L is harder. Comparing new and used Class L wheels shows service hardens the wheel considerably. The flange maximum hardness increases by 20% while the tread surface hardness increases by 28%.

3.3 TENSILE TEST RESULTS

During tension testing, new Class L wheel steel specimens exhibit discontinuous yield point behavior at all three testing temperatures. The values for upper and lower yield points (σ_{uyp} and σ_{lyp}) and the ultimate tensile strengths (UTS) for each specimen are listed in Table 3.5. As expected, both yield points and UTS increase as the temperature decreases. However, in agreement with the Rockwell hardness tests of the

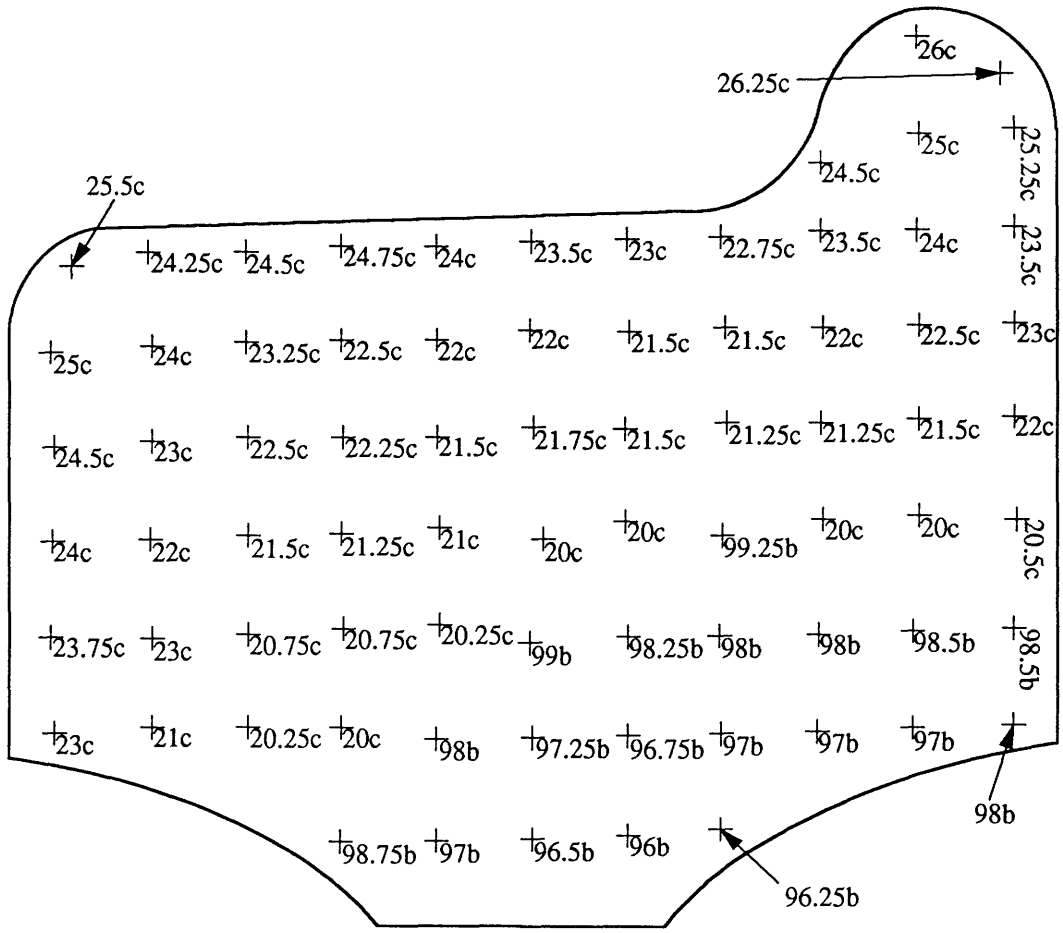

Fig. 3.10(b) The Rockwell B and C scale hardness profile of the circumferential plane of a new Class L wheel. Letters following numbers denote scale used.

wheel cross sections, the tensile data are also affected by the specimen's origin within the wheel. The deeper the sample's location within the wheel, the lower the yield points and UTS. Further, the strength decreases across the tread towards the flange. This may be seen in sample 4 tested at 70°F. It's location is shielded from the rim quench by the flange to such an extent that specimen 5 adjacent to it tested at 150°F (see Fig. 2.8 for

Table 3.5 Tensile test data from a new Class L wheel at temperatures of 0, 70 and 150°F. Specimen numbers are those given in Fig. 2.8 Values for σ_{uyp}, σ_{lyp}, UTS, and E are in ksi.

Spec, T°F	σ_{uyp}	σ_{lyp}	UTS	E	%el	%RA
1 0°	92.5	85.8	125.3	30423	20.3	36.2
5 0°	91.0	83.6	123.3	29800	22.3	40.8
3 70°	90.5	86.3	124.5	30492	18.7	36.7
4 70°	80.7	77.0	115.4	31090	21.9	41.7
2 150°	86.5	82.5	118.9	30434	18.2	36.6
6 150°	86.3	80.7	116.3	29962	20.6	41.6

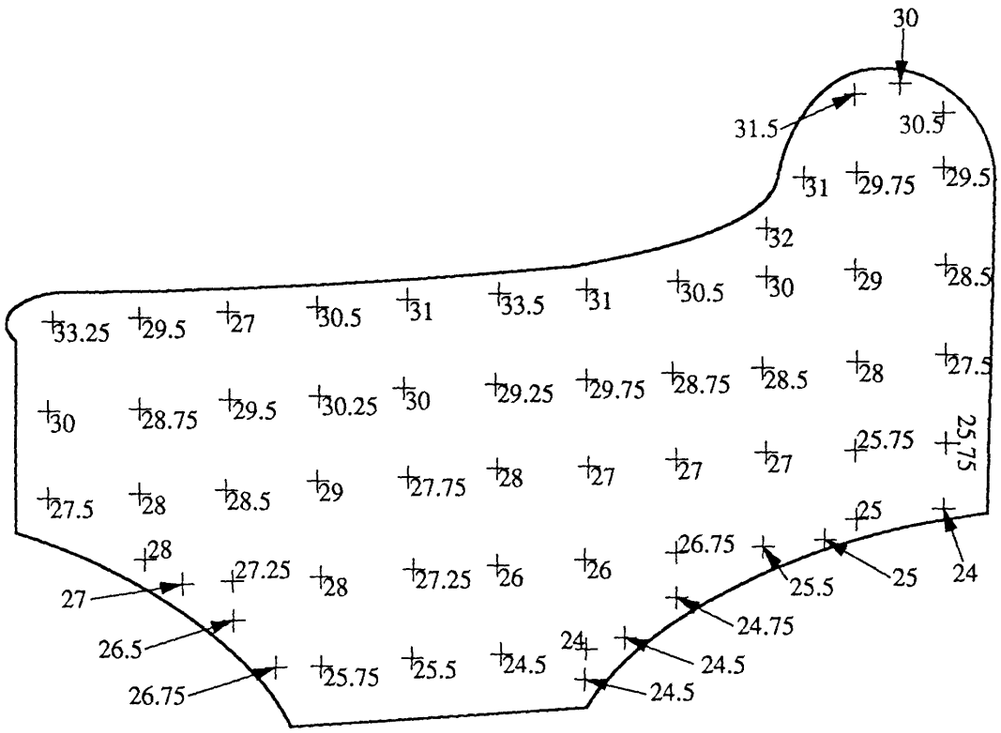

Fig. 3.11 The Rockwell C scale hardness profile of the circumferential plane of a used Class L wheel.

locations) is stronger. Also determined for each test and listed in Table 3.5 are Young's modulus (E), the percent elongation (%el) and percent reduction in area (%RA). E is determined as instructed in ASTM STM E111-82 using the strain deviation to determine acceptable data for the linear regression. This gives correlation coefficients of 0.9995 or better and coefficients of variation of 0.2% or less in all cases. As a comparison, a line fit to data for B82 wheel steel gives E at 0, 70 and 150°F of 30722, 30358 and 29944 ksi[33]. The data presented here are all within three percent of the B82 values.

In addition to these tensile properties, parameters describing the flow curves of the steel have been determined. The plastic portion of the stress-strain curves are fitted to a simple power law (eq. 3.1) and the Ramberg-Osgood equation (eq. 3.2):

$$\sigma = k\varepsilon^{n} \qquad \text{eq. (3.1)}$$

$$\frac{\varepsilon}{\varepsilon_{lyp}} = \frac{\sigma}{\sigma_{lyp}} + \alpha\left(\frac{\sigma}{\sigma_{lyp}}\right)^{n'} \qquad \text{eq. (3.2)}$$

where k is the strength coefficient, n is the strain-hardening exponent, $\varepsilon_{lyp}=\sigma_{lyp}/E$, α is a dimensionless constant and n' is the Ramberg-Osgood strain hardening exponent[34, 35].

The fitted data corresponds to uniform plastic strain and is taken at strains between the lower yield point at the end of the yield discontinuity and the maximum load. The regressions all have correlation coefficients of 0.999 and greater. All fitting parameters are listed in Table 3.6. These parameters show that as the strength increases, the ability to strain harden decreases.

Table 3.6 Results of power law and Ramberg-Osgood curve fits to true stress-strain data from tensile tests.

Spec, T°F	k	n	α	n'
1 0°	220.73	0.20275	2.5579	5.4658
5 0°	221.04	0.21186	2.8168	5.1945
3 70°	216.55	0.19364	2.2709	5.7702
4 70°	206.00	0.20906	2.8948	5.1807
2 150°	207.19	0.19382	2.4017	5.7373
6 150°	202.97	0.19559	2.5533	5.6390

3.4 CHARPY IMPACT

The results of all Charpy impact tests are given in Table 3.7. The Class A steel requires more energy (CVN) to fracture the specimens at all temperatures than the Class L steel. Included in the table are the lateral expansions of the CVN specimens at the striking side of the specimen and the percent shear fracture of the fracture surface. Both increase with increasing CVN. All values given are averages of three tests conducted at each temperature except for Class L at 70°F (see Table 2.2). Only one test was conducted at this temperature because CVN values were already established at this temperature[36]. However, the Class L steel for this battery of tests is much more brittle. At 70°F, the previous testing recorded an average CVN of 15.0 ft-lbs. placing it closer to the 150°F tests of this round of testing.

Table 3.7 Average Charpy impact energy (CVN±SD) in foot-pounds for Class A and Class L wheel steel. The linear expansion (LE) is measured in mm and %SF is the percent shear fracture.

	Class A			Class L		
Temp. °F	CVN	LE	%SF	CVN	LE	%SF
0	7.32±0.38	0.13	0	2.68±0.26	<0.05	0
70	10.2±1.22	0.18	23	9.44	0.20	18
150	17.2±2.46	0.37	47	13.6±1.65	0.30	27

3.5 PLANE STRAIN FRACTURE TOUGHNESS

Using the average crack length and eq. (2.1), K_Q is calculated for each specimen and listed in Table 3.8. In turn, K_Q validity requirements are verified. Invalid criteria are listed in Table 3.8. As can be seen, only one test met all requirements of ASTM STM E

399-90 to yield a valid K_{Ic} value. All samples, except B2, are too small since $2.5(K_Q/\sigma_{lyp})^2$ is larger than a and B. With K_Q serving as an indicator, a and B would need to be around 1.65 and 1.85 inches for the 70 and 150°F tests, respectively. Further, samples D1 and C1 both have a short fatigue precrack on one of the side faces. This renders these tests invalid since the crack front in this region may be affected by the stress concentration of the machined straight through notch which will cause failure at a lower apparent K value. The last validity requirement not met is the maximum to conditional

Table 3.8 Record of the conditional plane strain fracture toughness (K_Q) in ksi$\sqrt{in}$ and the invalid test parameters which refer to the section in STM E399-90 that is violated.

Sample	K_Q	P_{max}/P_Q	$2.5(K_Q/\sigma_{lyp})^2$	Invalidity by ASTM section
B2 0°F	49.6 (K_{Ic})	1.000	0.859	Valid
A1 70°F	63.5	1.143	1.514	7.1.1, 9.1.2
D1 70°F	60.3	1.000	1.363	7.1.1, 8.2.2 (2)
D2 70°F	65.9	1.000	1.629	7.1.1
C1 150°F	66.8	1.530	1.672	7.1.1, 8.2.2 (2), 9.1.2
C2 150°F	68.5	1.423	1.762	7.1.1, 9.1.2

load ratio. The acceptable value of 1.10 is exceeded by specimens A1, C1 and C2. A high P_{max}/P_Q ratio indicates that a significant amount of plastic yielding is occurring within the body during loading. This is also evident in Figs. A9 and A10 of the appendix where a considerable amount of nonlinear plastic loading occurred in the high temperature tests.

Macrofractography of 0 and 70°F tests reveals faceted regions of the fracture surfaces following the fatigue precracks. This is true for the 150°F fracture surface, however, the fatigue crack here is immediately followed by a fibrous zone and then the faceted region (Fig. 3.12). None of the fracture surfaces exhibit chevron marks due to the square cross section of the samples. The remaining macrofractographic feature is the appearance of shear lips on all samples. As the crack advances, the front close to free surfaces is inclined 45° to the crack plane. The shear lip widths are listed in Table 3.9.

Table 3.9 The shear lip width in mm for each sample. Sample B2 has a discontinuous shear lip. Prop is the proportion of the fracture surface involved in oblique fracture per unit thickness. %SF is the percent of the fracture surface which failed by microvoid coalescence.

Sample	B2 0°F	A1 70°F	D1 70°F	D2 70°F	C1 150°F	C2 150°F
Width	0.2	1.0	0.7	0.9	2.4	3.7
Prop	0.01	0.04	0.03	0.04	0.10	0.15
%SF	2	15	7	10	43	44

(a)

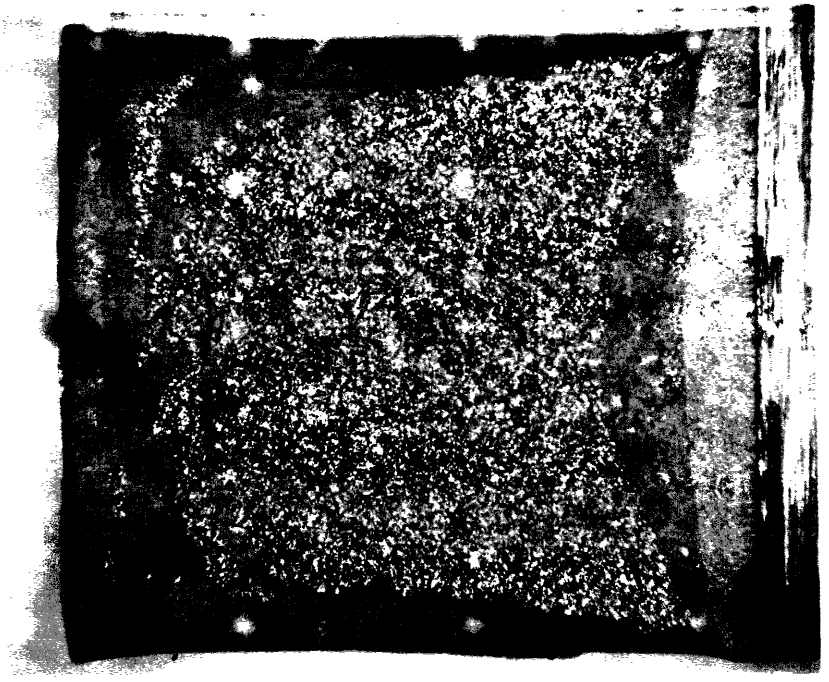

(b)

Fig. 3.12 C1, 150°F, 3.25x. (a) Excel lamp (b) Directed incandescent. Shear lips are present on all samples and thicken with temperature as does the amount of ductile fracture (dull gray in (a)). Readily seen is the popin, the fibrous fracture surface directly following the precrack. Crack growth is from left to right.

The increased resolution of the SEM identifies the micromechanisms of fracture to be transgranular cleavage (Fig. 3.13) and microvoid coalescence (Fig. 3.14). The relative amount of shear fracture (%SF) surface for each specimen is listed in Table 3.9.

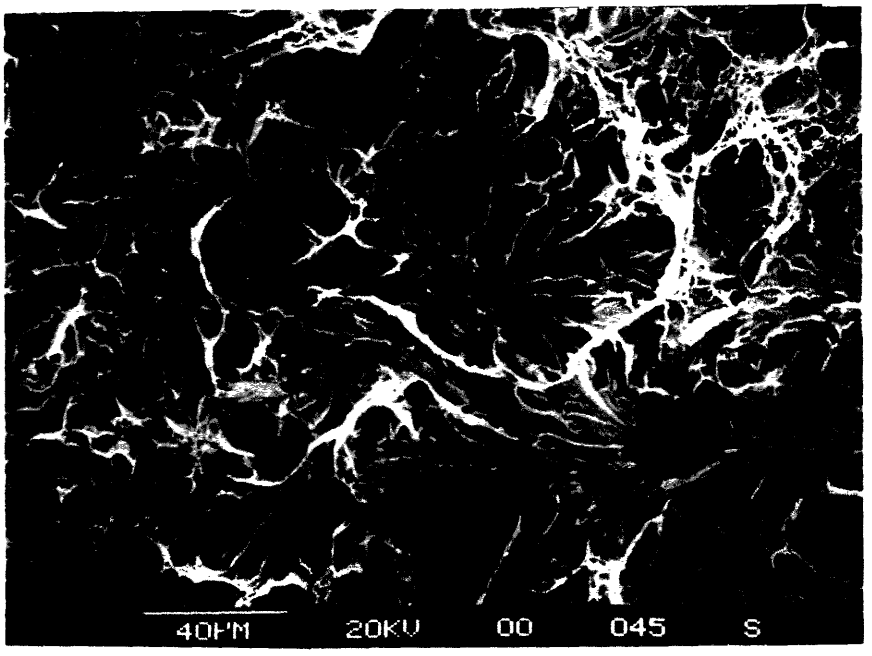

Fig. 3.13 D2, 70°F, 475x. SEM microfractograph of the surface of the brittle fast fracture region showing failure by transgranular cleavage. Crack grows from bottom to top.

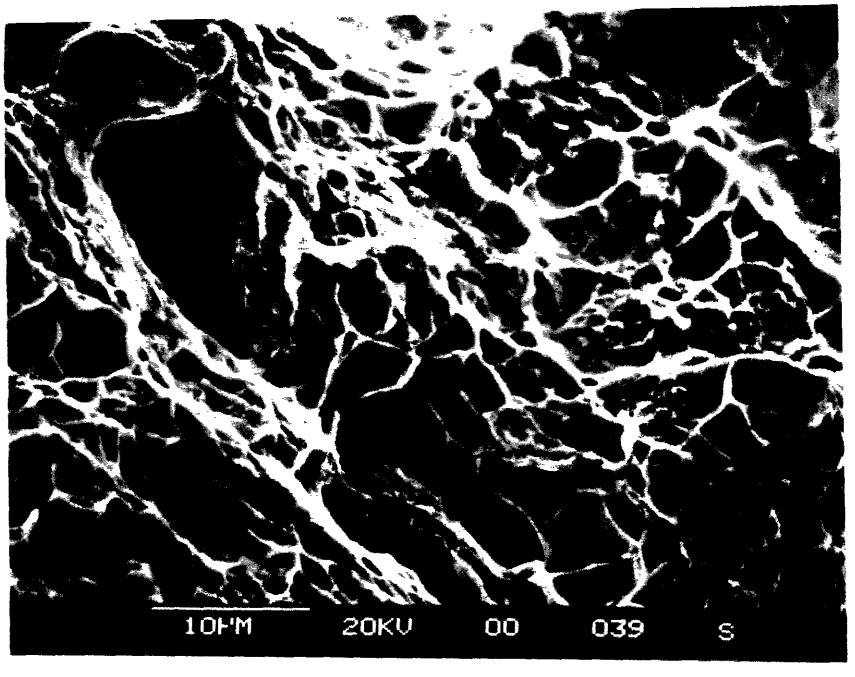

Fig. 3.14 D2, 70°F, 2150x. The oblique fracture of the shear lip occurred by the nucleation, growth and coalescence of voids. Crack grows from bottom to top.

Cleavage occurs throughout the faceted region of all samples. Likewise, the dimpled appearance of microvoid coalescence is found in the shear lips of samples at all temperatures and the fibrous zone of the 150°F samples. However, microvoid

coalescence is not held exclusively to these areas and in the 70 and 150°F tests, dimples are found on the flat portion of the crack plane as well as the shear lips.

3.6 FATIGUE CRACK PROPAGATION

To determine the material's resistance to fatigue, the crack propagation rate (da/dN) is plotted versus the crack driving force (either ΔK or ΔJ). An attempt to do this for rising ΔK_{eff} test data calculated during runtime by the AFCP program is shown in Fig. 3.15. In it are plotted da/dN versus ΔK_{eff} and ΔK_J where ΔK_J is defined as:

$$\Delta K_J = \sqrt{\frac{E\Delta J_{eff}}{1-\nu^2}} \qquad \text{eq. (3.3)}$$

ΔK_J quantifies the plastic portion of ΔJ_{eff} and allows comparisons between cyclic J-integral and cyclic stress intensity data. Fig. 3.15 would imply that the amount of

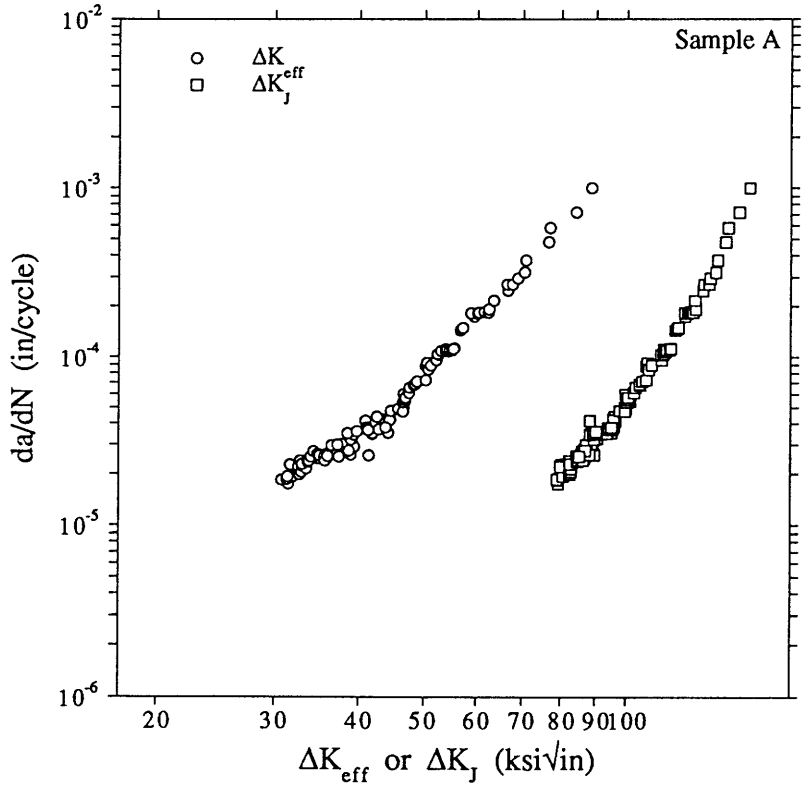

Fig. 3.15 Plot of fatigue crack growth rate vs ΔK_{eff} and ΔK_J as calculated by the AFCP program.

plasticity taking place during cycling, even at low stress intensity levels of ≈30 ksi√in, is large enough to double the crack driving force ($\Delta K_J \approx 80$ ksi√in). Closer inspection reveals that the AFCP program computes ΔJ_{eff} using the nominal rather than the effective cyclic stress intensity factor. In effect, the computer calculates ΔJ_{eff} in eq. (2.6) using ΔK rather than ΔK_{eff} and it is unknown as to what area A_{pl} represents (see Fig. 2.11).

To overcome this problem computer programs are written to recalculate the data for the tests from the raw load-load line displacement (P-COD) hysteresis loops. The first program simply finds the normalized unloading compliance (ECB) as described in section 2.7.1 and then calculates a compliance crack length (a_{cmpl}) using eq. (2.2). This program is used with the initial cycles of the precracking data to determine the Young's modulus for each specimen (E_i) such that a_{cmpl} matches the initial machined starter notch length. Once all E_i are determined, the average ($\overline{E}$=27948.7 ksi) is taken and used for the remainder of the recalculations. Although $\overline{E}$ is low for steel, it is within ten percent of the actual value and therefore acceptable to use as mandated by ASTM STM E647-91[20]. The error in using $\overline{E}$ rather than E_i is less than 0.25% for the initial cycles of the precracking tests.

The program is then expanded to calculate all the parameters determined during runtime by the AFCP program. ECB changes by 15% at most and this is attributable to the use of $\overline{E}$ and the fact that the unloading slope of a loading cycle's hysteresis P-COD loop is used to determine the closure load rather than the previous cycle's. This affected the calculation of a_{cmpl} but only changes it by 4%. Other parameters slightly affected (changed by 10 to 20%) are P_{cl}, ΔK and ΔK_{eff}. On the other hand, rising ΔK_{eff} control tests have cyclic J-integral parameters (the elastic, plastic and total ΔJ_{eff}) and ΔK_J vary by hundreds to thousands of percent. These same parameters for a rising ΔJ_{eff} control test, however, only differ by 50% or less. Finally, a_{cmpl} versus the number of cycles are smoothed using a routine given in the appendix of E647-91. This also gives very different results for da/dN as compared with the runtime data. This is expected since the runtime routine must use a secant method to approximate da/dN and doesn't have the benefit of knowing the crack lengths for future cycles necessary to perform the piecewise curve fit described in E647-91. Compare Fig. 3.16(a) with Fig. 3.15 to see the effects of recalculation. Plots of data for the remaining tests are given in Fig. 3.16(b)-(f).

Fig. 3.16(a)-(f) These 6 figures follow on the next 3 pages. Each plot contains two curves, one each for da/dN versus ΔK_{eff} and ΔK_J. The open symbols denote data generated by a rising ΔK_{eff} test run in load control and filled symbols are for rising ΔJ_{eff} tests run in COD control.

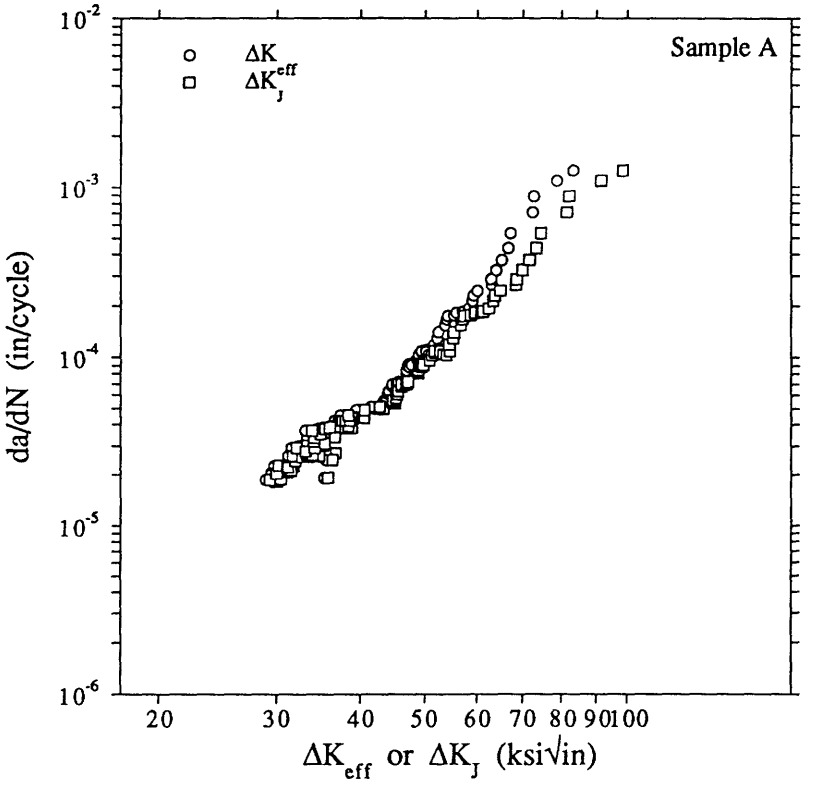

Fig 3.16 (a)

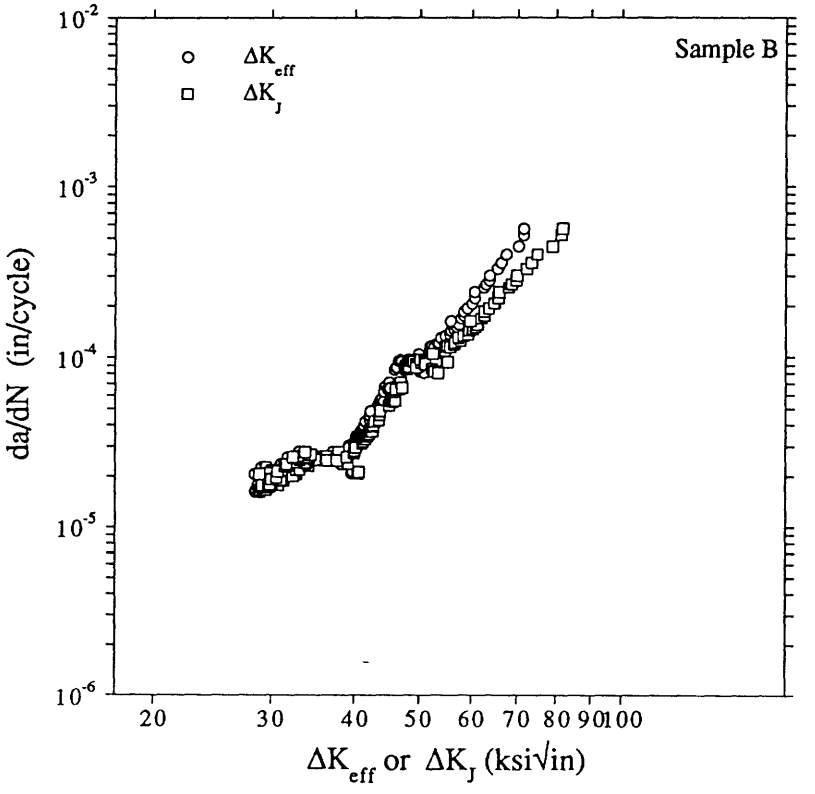

Fig. 3.16 (b)

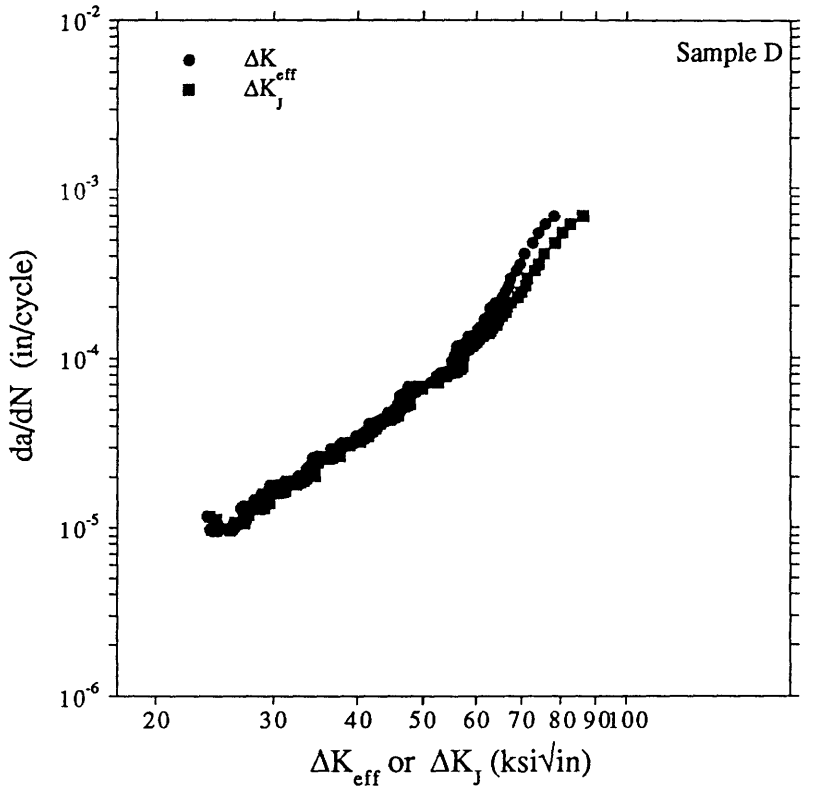

Fig. 3.16(c)

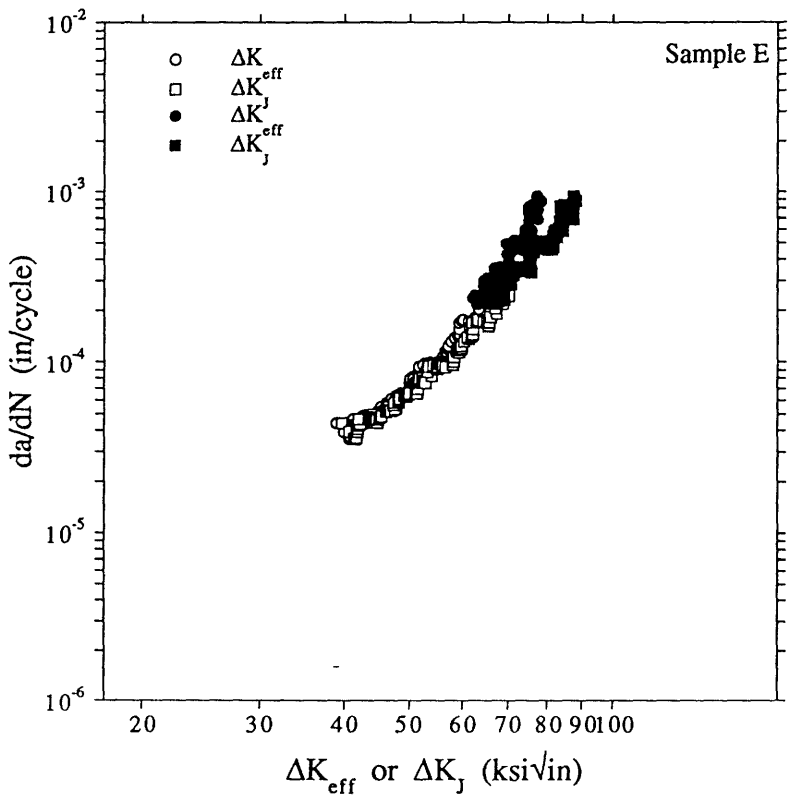

Fig. 3.16 (d)

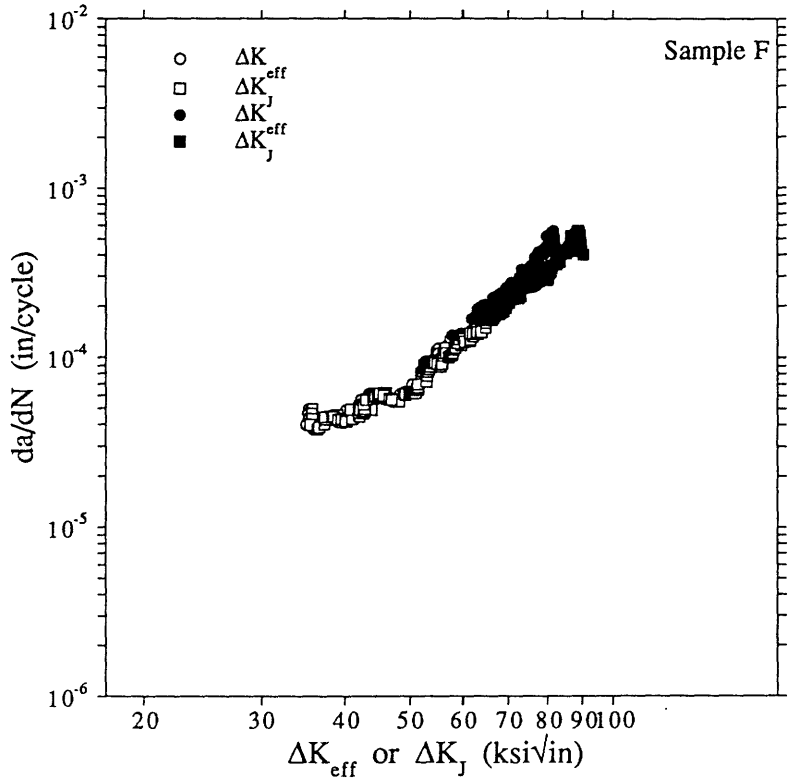

Fig 3.16(e)

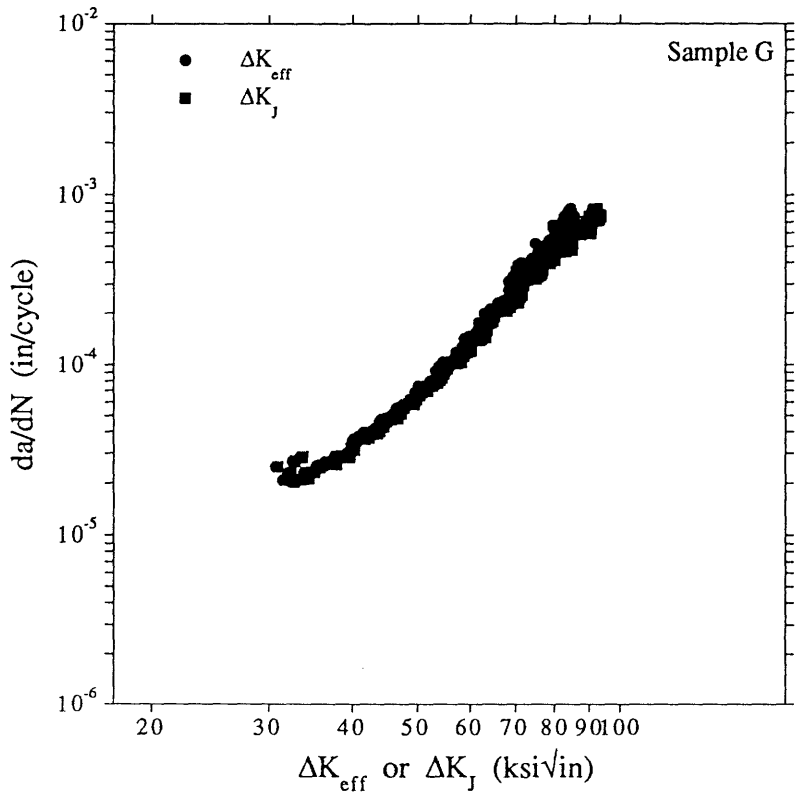

Fig. 3.16(f)

Three additional parameters are calculated for each cycle: the maximum stress intensity factor (K_{max}) and two specimen size criteria. The criteria (CRITY or CRITF) are given by:

$$CRIT = \frac{4}{\pi(W-a)}\left(\frac{K_{max}}{\sigma_o}\right)^2 \qquad \text{eq. (3.4)}$$

where CRITY is given when σ_o is substituted by σ_{lyp} and CRITF is given when σ_o is substituted with the flow stress:

$$\sigma_{fs} = \frac{\sigma_{lyp}+UTS}{2} \qquad \text{eq. (3.5)}$$

These parameters, when greater than 1.0, ensure that the specimen is predominantly elastically loaded through the cycle[20].

At this point, the data can be fitted to power law curves such that the fatigue crack propagation rate may be given as a function of either the elastic or elastic plastic crack driving force. Plots for each sample are given in the appendix. These fits give the constants C and m in the Paris law equation:

$$\frac{da}{dN} = C(\Delta DF)^m \qquad \text{eq. (3.6)}$$

where ΔDF is the crack driving force and represents either ΔK_{eff} or ΔJ_{eff}. The results of the curve fitting are given in Table 3.10. Samples E and F differ from the others because they had crack growth via a ΔK_{eff} control test followed by a ΔJ_{eff} control test (see Tables 2.4 and 2.5). However, plots of the data generated by the subsequent ΔK_{eff} and ΔJ_{eff} control tests show no discontinuity at the transition. This is true despite the fact that sample E was cycled at R=-1.0, sample F at -0.5 and the following ΔJ_{eff} control tests cover a range of R because the system is in COD control. This shows the robustness of the method used to determine the closure load by the AFCP program and shows that the true crack driving force extends the crack only when the crack has completely opened. Concerning the specimen size criteria, CRITY is exceeded for about ten cycles in samples A, B and D. For samples E, F and G approximately half of the data are invalid. Despite the invalidity of CRITY, the data are quite well behaved as evidenced by the correlation coefficients listed in Table 3.10. Apparently the material in front of the crack tip strain hardens enough during cycling that the plastic zone size remains small and the specimen is predominantly elastically loaded. It has been noted that for high strain hardening materials, where $UTS/\sigma_{ys} \geq 1.3$, the CRITY specimen size requirement may be too restrictive[20]. This seems to apply to Class L steel with $UTS/\sigma_{lyp}=1.47$ and CRITF valid for all cycles of all samples except the last 40 of sample G.

The fatigue fracture surfaces are flat with neither shear lips nor lateral contraction and do not stray from the plane of the side grooves. To the naked eye, the fatigue fracture surface appears rough but less so than the cryogenic fast fracture region. A representative

Table 3.10 Listing of the material constants of the Paris law determined for fatigue crack propagation rates as functions of either the cyclic stress intensity factor or the cyclic J-integral. Values of C are to be multiplied by 10^{-10} and C' by 10^{-3}. The units of C and C' depend upon the magnitude of m and m': C≡in/cycle/(ksi$\sqrt{\text{in}}$)^m and C'≡in/cycle/(ksi·in)$^{m'}$.

	ΔK_{eff}	data	fit	ΔJ_{eff}	data	fit
Sample	C	m	R	C'	m'	R
A	0.610	3.70	0.972	6.33	1.67	0.983
B	1.53	3.42	0.973	4.38	1.58	0.987
D	2.59	3.23	0.942	3.55	1.55	0.961
E	0.0106	4.64	0.971	12.6	2.06	0.982
F	3.18	3.19	0.979	3.21	1.48	0.986
G	0.123	4.01	0.991	7.83	1.86	0.987
ALL	1.01	3.51	0.932	5.11	1.65	0.955

macrofractograph depicting the surface variation is shown in Fig. 3.17. The fatigue fracture shows no signs of beach markings. The only discernible crack front traces are those due to the transition between precracking and the fatigue tests and between fatigue at test end and fast fracture. Of these, the demarcation between precracking and the fatigue tests is very faint and not readily seen.

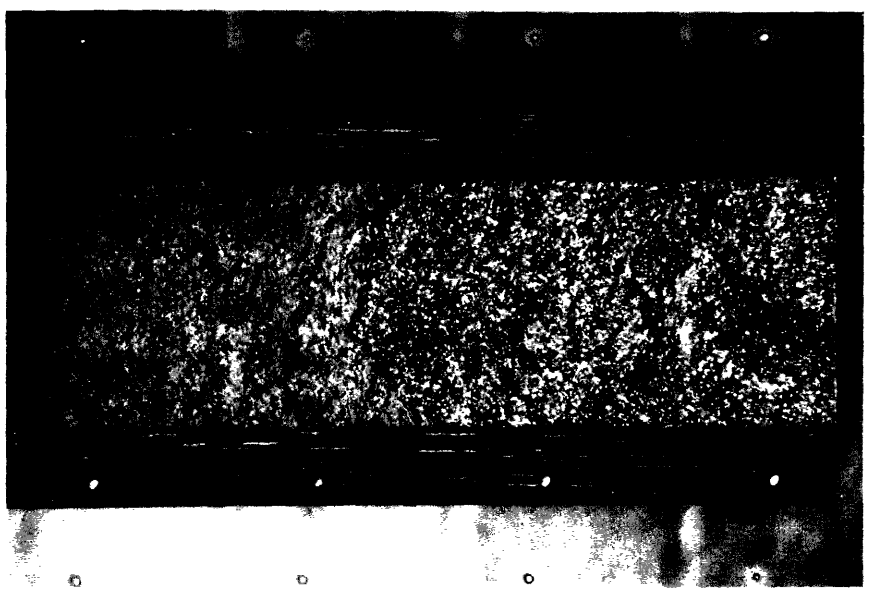

Fig. 3.17 Fracture surface of fatigue sample E at 4.25x. The crack growth direction is from left to right. Visible are the crack front at test end prior to fast fracture at cryogenic temperatures.

The crack front at either test transition location is bowed. However, due to the side grooves, the crack does not tunnel; instead the crack front grows fastest at the side groove notches. This is one of the motivations behind the recalculation of $\overline{E}$. Because the crack grows fastest at the side groove notches, monitoring the crack front with a traveling microscope and modifying the Young's modulus input to the AFCP program so

that a_{cmpl} matches the side groove notch root crack length is erroneous. Even still, a_{cmpl} determined using $\overline{E}$ in the recalculation programs does not match that measured from the crack surface at test end since the measured compliance is an average for the curved crack front. However, the difference between a_{cmpl} and that measured from the crack surface at test end differ at most by two percent at the specimen center. Unfortunately, this error rises to as much as 8.2% at the side groove notch root. This bowing behavior is expected since K will increase by approximately 75% at the side groove notch roots[37].

The initiation and growth of a fatigue crack emanating from the side groove notch at the back face is not expected but can be rationalized. This backcrack, barely visible in Fig. 3.17 is magnified in Fig. 3.18 and appears as a triangular region. During the compression portion of the fatigue cycle the back face of a specimen is loaded in tension. The side groove notch root radius is quite sharp (0.015") and may readily initiate fatigue backcracks. Backcracks are present in all specimens, including the D and G rising ΔJ_{eff} tests run completely under COD control. This illustrates the effectiveness of the stress concentration at the side groove notch root because the R of the COD controlled tests are small and become negative later in the tests. Listed in Table 3.11 are the lengths of the backcrack measured along the side grooves (a_g) and back face (a_b). Specimen A has such a large backcrack because it was used for a trial rising ΔJ_{eff} test to an a_{cmpl} of 1.7".

The final feature of the fatigue fracture surfaces observable to the unaided eye is the appearance of cleavage facets seen as bright points of light amidst the ductilly

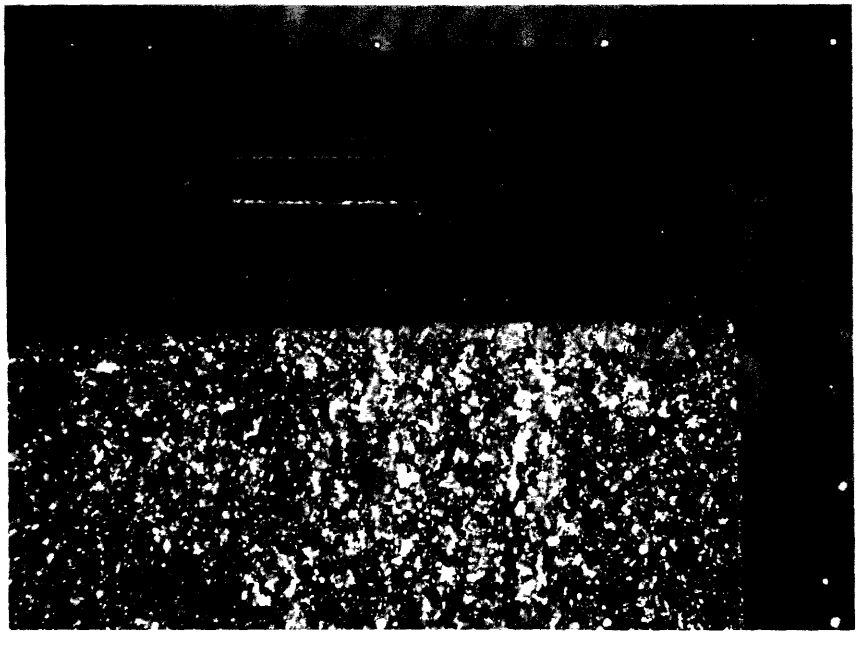

Fig. 3.18 Magnified (13.8x) view of Fig. 3.17 showing the backcrack which initiated and grew from the back face at the side groove stress concentration.

Table 3.11 Backcrack lengths in mils measured along the side groove notch root (a_g) and specimen back faces (a_b).

	LEFT SIDE		RIGHT SIDE	
Specimen	a_g	a_b	a_g	a_b
A	223	78	204	72
B	99	26	—	—
D	68	6	—	—
E	175	17	172	12
F	163	13	122	8
G	122	10	88	5

ruptured dull gray surface. These appeared randomly across the fatigue fracture surface, did not become more prevalent at higher fatigue crack growth rates and are estimated to account for less than one percent of the fatigue fracture surface area. Upon an increase in magnification through the use of the SEM it is found that locating a cleavage facet in the fatigue fracture surface is difficult, confirming the one percent estimate.

On the microscopic scale resolved by the SEM the fatigue fracture surface is non uniform, indicative of a tortuous crack path. Fractography reveals several different micromechanisms of fatigue fracture. A representative example of the fatigue fracture surface is shown in Fig. 3.19. Immediately evident is the high amount of plasticity which occurred during fatigue fracture. Secondary cracking caused by the large plastic zone size on large (multiples of the grain size) and smaller (fraction of the grain size) scales is

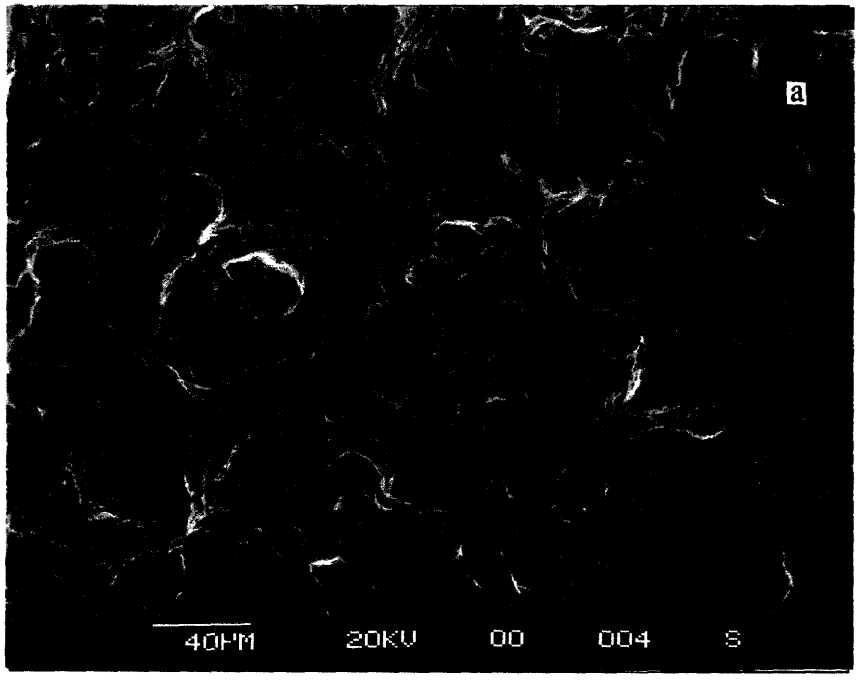

Fig. 3.19 A representative SEM fractograph (sample A, 300x) of a fatigue fracture. The crack grew at a high rate from bottom to top. Striations are at marker "a."

also present. Increasing the magnification of the area marked "a" in Fig. 3.19 shows the presence of striations (Fig. 3.20)[38]. Fatigue striations result from subsequent plastic blunting and resharpening of a fatigue crack tip by duplex slip and concomitant slip irreversibility due to oxidation[39, 40]. Striations appear in small patches, the size and frequency of which diminish at higher crack growth rates. Locally, striations may propagate skew to the macroscopic crack growth direction. This is a testament to the

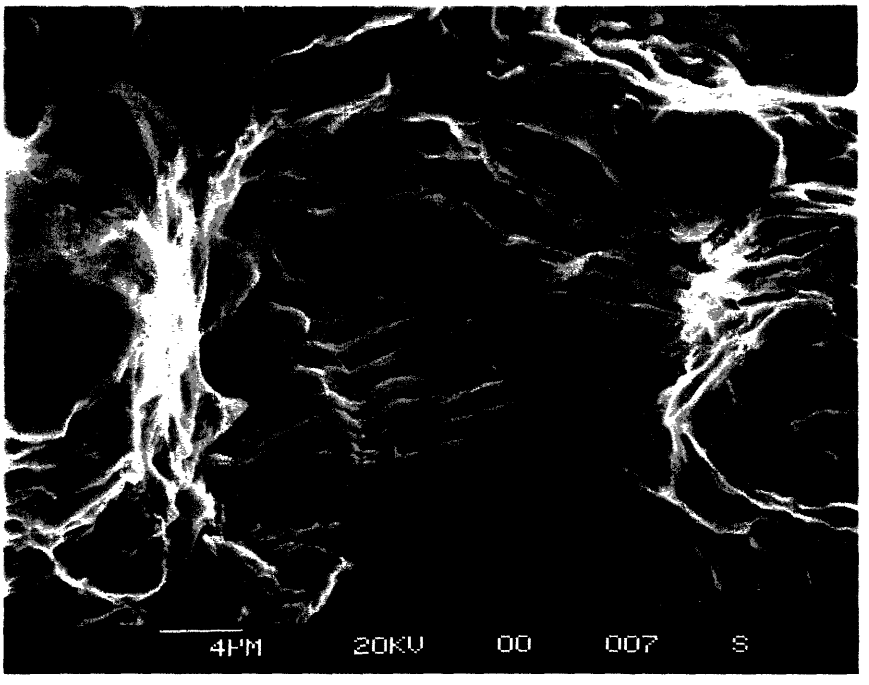

Fig. 3.20 Secondary cracks initiated at striations marked "a" in Fig. 3.19 are seen here at 2500x.

variation in the crack front[38]. Striations may also serve as initiation sites for secondary cracks which grow as fatigue cracks (Fig. 3.20). Striation patches are accompanied by the ductile rupture mechanism of microvoid coalescence (Fig. 3.21) which becomes more pronounced at higher crack growth rates. Due to the compressive component of the fatigue cycle present in all tests there is much damage to the fatigue fracture surface. Severe rubbing occurred on many spots (Fig. 3.22) and may be responsible for the general lack of discernible features.

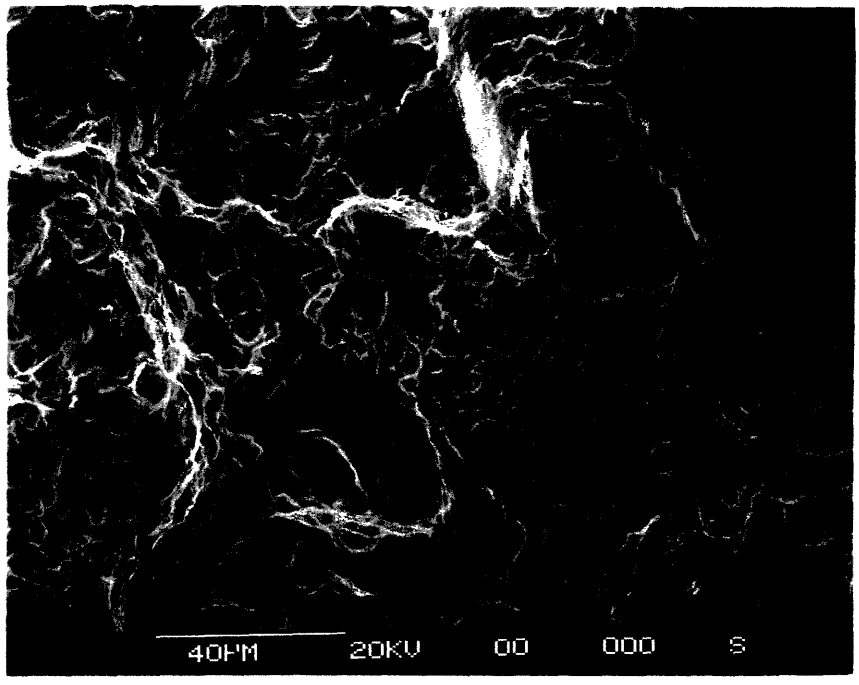

Fig. 3.21 Sample F, 610x. The crack advances by a ductile void growth mechanism from bottom to top at approximately $4 \cdot 10^{-4}$ $^{in}/_{cycle}$ in this microfractograph.

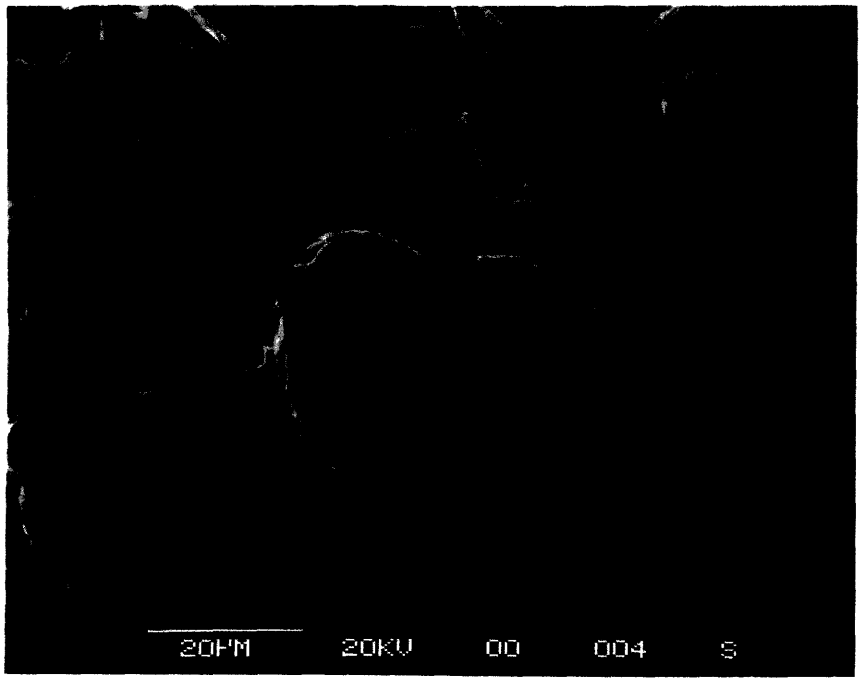

Fig. 3.22 Rubbing caused by ΔK_{eff} cycling at R=-1. Sample B, 1000x, crack growth from bottom to top.

4.0 DISCUSSION

4.1 METALLOGRAPHY AND HARDNESS

4.1.1 QUENCHING EFFECTS

The rim quench greatly influences the microstructure of the wheel tread surface and accounts for the drastic differences in V_α present in the two wheel alloy classes and that predicted by the equilibrium phase diagram. The wheel steels contain Mn which is an austenite stabilizer capable of reducing the eutectoid carbon content. Silicon also has this ability[32]. At the alloy concentration levels present in the wheel steels, this effect can reduce the equilibrium V_α by less than two percent. The remaining loss in V_α may be due to undercooling the austenite during the rim quench process. This being the case, the Class L wheel studied was subjected to a more severe quench than the Class A wheel. This is seen in the micrographs of Fig. 3.1. Increasing the cooling rate causes an instability along the front of growing ferrite GBA resulting in the growth of Widmanstätten side plates (WSP)[31]. The micrographs of Fig. 3.1, taken at a depth of 1.5" from the tread surface, show the WSP morphology only in the Class L steel. Microstructures closer to the surface show copious WSP in Class L steel while Class A steel primarily forms GBA with few plates (Fig. 4.1). This proves the severity of the Class L quench to be considerably greater than that of the Class A wheel.

These findings are partially supported and negated by Rockwell hardness tests. Fig. 3.10 shows Class A steel is slightly harder along the tread surface. This contradicts the notion that Class L steel, being subjected to a more severe quench, should form more pearlite and be harder. More inconsistency to the theory is provided by the comparison of the interlamellar spacings. A more severe quench will have higher cooling rates and, consequently, narrower pearlite lamellae, yet the classes have nearly the same interlamellar spacing (0.41 microns for Class A versus 0.44 for L)[21]. A possible explanation for the hardness discrepancy may be the grain size; smaller grains can increase the strength and Class A has smaller grains (Table 3.1). Support for the quench severity comes from the gradient in the wheel's hardnesses. Class L should be able to harden the wheel to a greater depth. This does occur, as the Class A wheel's hardness drops at a faster rate through the rim thickness (Fig. 3.10).

4.1.2 GLEEBLE MICROSTRUCTURE-MACROSTRUCTURE RELATIONSHIPS

4.1.2.1 Strain Effects: Slip Line Field Theory

For plane strain conditions, slip line field theory predicts, for the sample-anvil geometry tested (Fig. 2.4(a)), planes of maximum shear stress produced in the sample to run diagonally through the body from each anvil edge to the opposite anvil edge on the

(a)

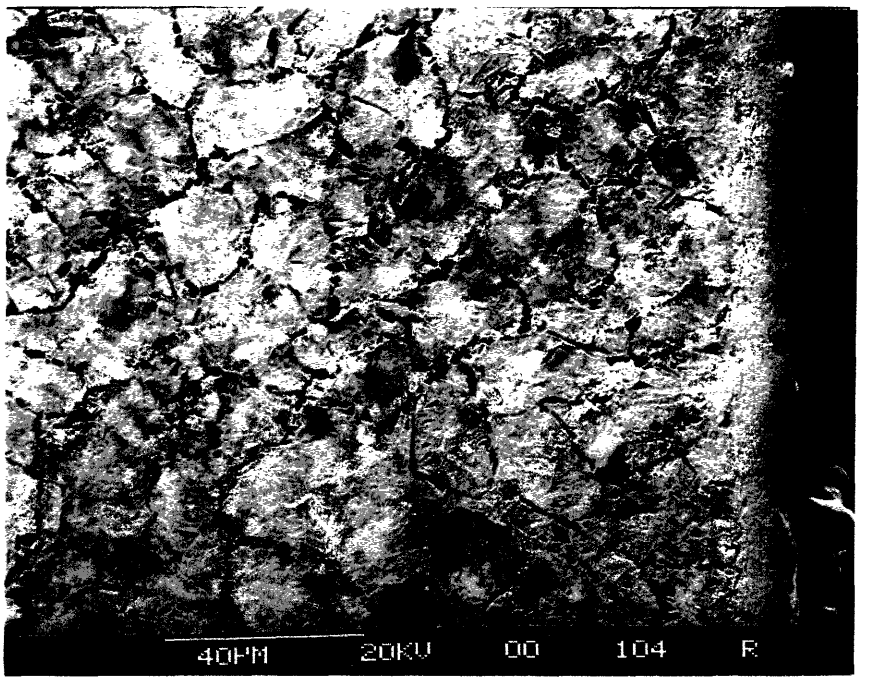

(b)

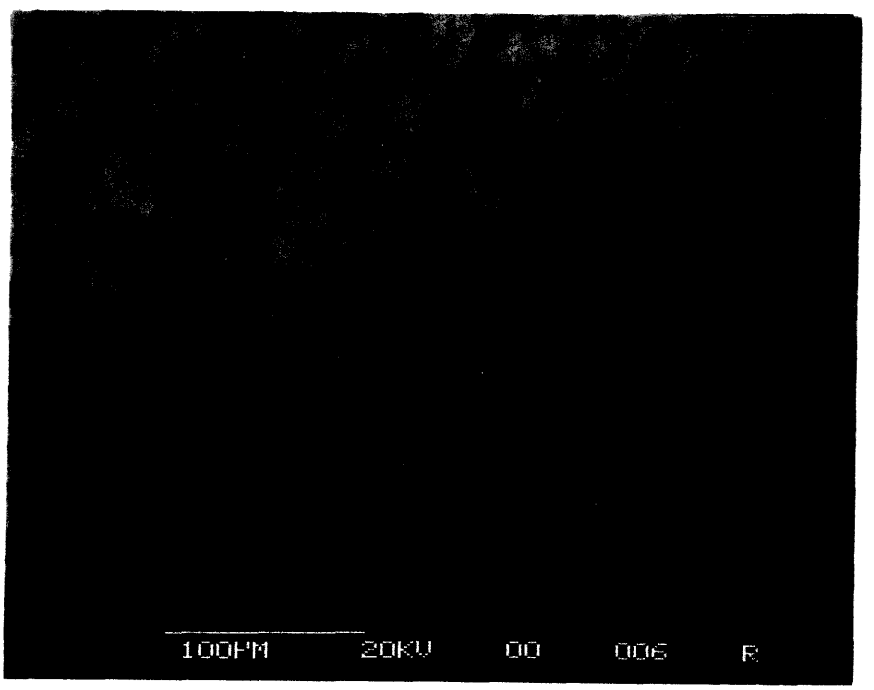

Fig. 4.1 Quench affects the Classes differently at the tread surface. (a) Class A (at the surface, circumferential plane, 640x) procutectoid ferrite remains predominantly GBA. (b) Class L proeutectoid forms principally as WSP (6mm below tread surface, 250x).

other side (Fig. 4.2). This partially explains the hot compression test results. Maximum shear stress planes delineate regions of heavy plastic deformation. Therefore, the appearance of HS grains at anvil edges is expected with either UL or DL grains appearing elsewhere. Fig. 3.7 illustrates this and the continuation of strained grains toward the

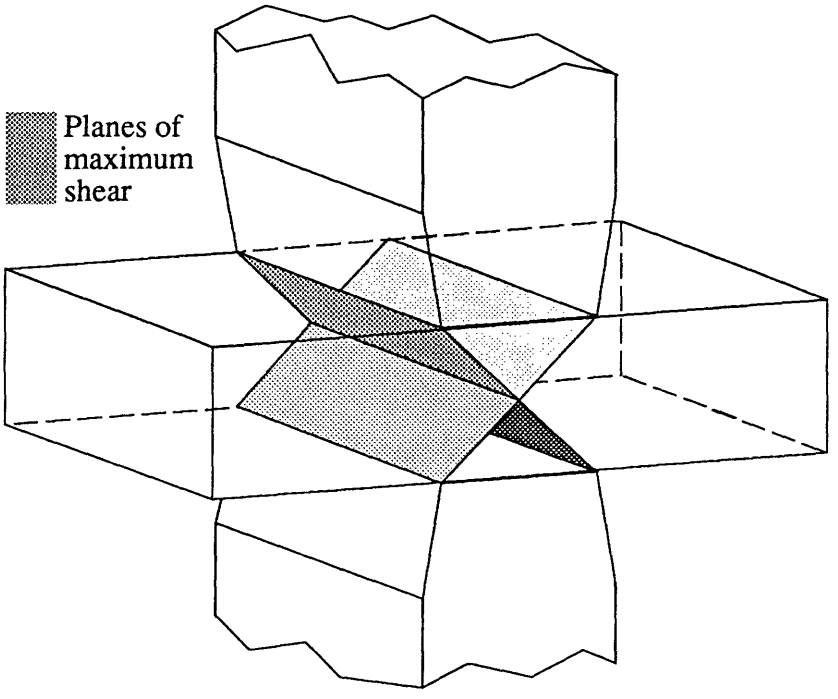

Fig. 4.2 Schematic showing the maximum planes of shear strain within the specimen during compression

specimen center. The HS grains manifest the X macrostructure on a macroscopic level. Thus, applying sufficient strain produces the X macrostructure with HS, DL and UL microstructures from a specimen initially containing A and UL structures.

4.1.2.2 Temperature Effects: Recrystallization

PT and FR grains develop from the HS grains. HS grains contain stored energy from heavy plastic deformation and act as primary recrystallization sites. Recrystallization occurs in these regions, but initiates at specimen centers. Fig. 4.3 shows specimen center PT microstructure development. In specimen 732-3, HS grains did not recrystallize, yet FR grains appear at its center and PT grains appear between these and the surface in contact with the anvils. Therefore, grains of advancing PT and FR microstructures consume the strained matrix, ultimately leading to the S macrostructure of Fig. 3.4.

Recrystallization initiation at specimen centers is odd. Recrystallization ease generally increases with strain and temperature. Grains near anvil edges are strained much more than the center. Therefore, recrystallization is expected to start at the edge and move toward the center. Anvil cooling of the specimen face may suppress this. In Fig. 4.4, extensive recrystallization occurred throughout except for the faces in contact with anvils.

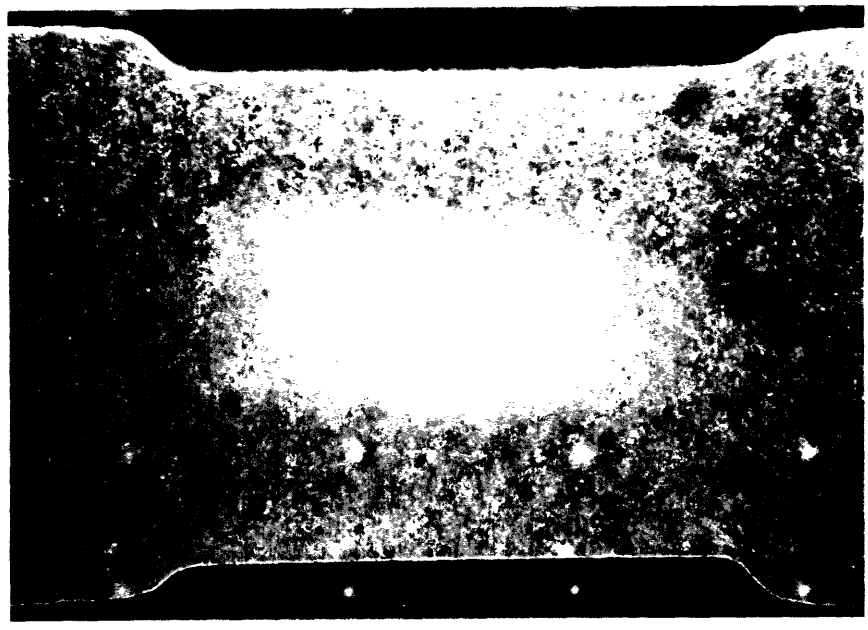

Fig. 4.3 732-1, 1350°F, 17.8%e, all, 15x. Recrystallization at specimen center by consumption of HS microstructure. The macrostructure is a mixture of X and S.

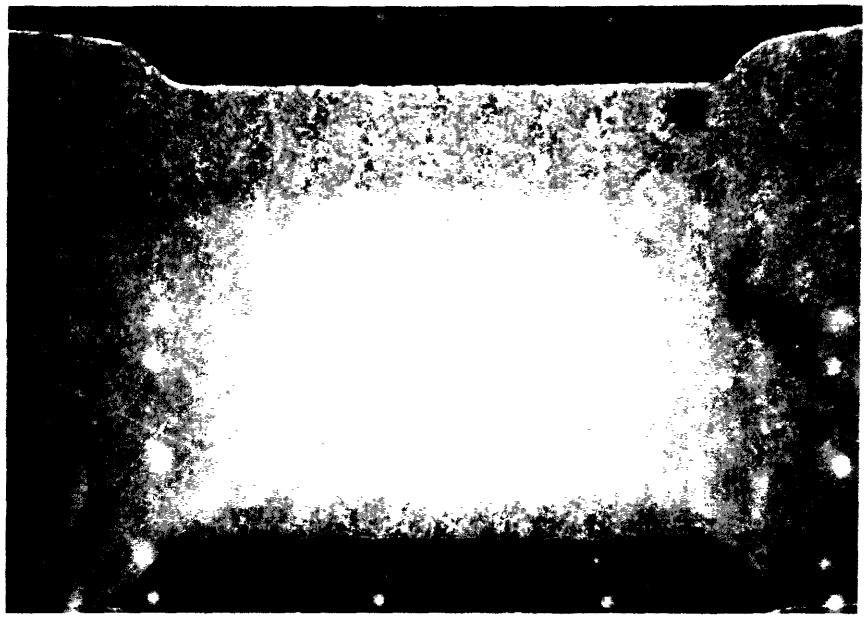

Fig. 4.4 760-3, 1400°F, 16.2, all, 15x. Recrystallization suppression of specimen faces by anvil cooling.

4.1.2.3 Normal Macrostructures

Normal macrostructures (Figs. 3.3 through 3.5) are symmetrical and contain one macrostructure. All macrostructures contain UL grains at the specimen ends. The A macrostructure contains UL and DL grains. The X macrostructure is devoid of PT and FR grains while the S macrostructure is HS grain free. Complications to these basic relationships exist and result in a mixture of two macrostructures. The first complication

results from the extent of recrystallization. Cooling the sample shortly after the onset of recrystallization incompletely consumes the HS microstructure (Fig. 4.3) and gives compelling evidence that the HS grains transform to PT and then FR grains. Cooling is also seen in sample 704-2 where all four microstructures exist (Fig. 4.5). Tantalum strips between specimen and anvil reduces friction during compression. These induce recrystallization in DL grains and complicate a macrostructure that otherwise would be X. The final complication depends on the grips and anvils. Uneven compression bends the sample; one side strains more than the other. This causes each side to recrystallize differently and is evident in Fig. 4.4.

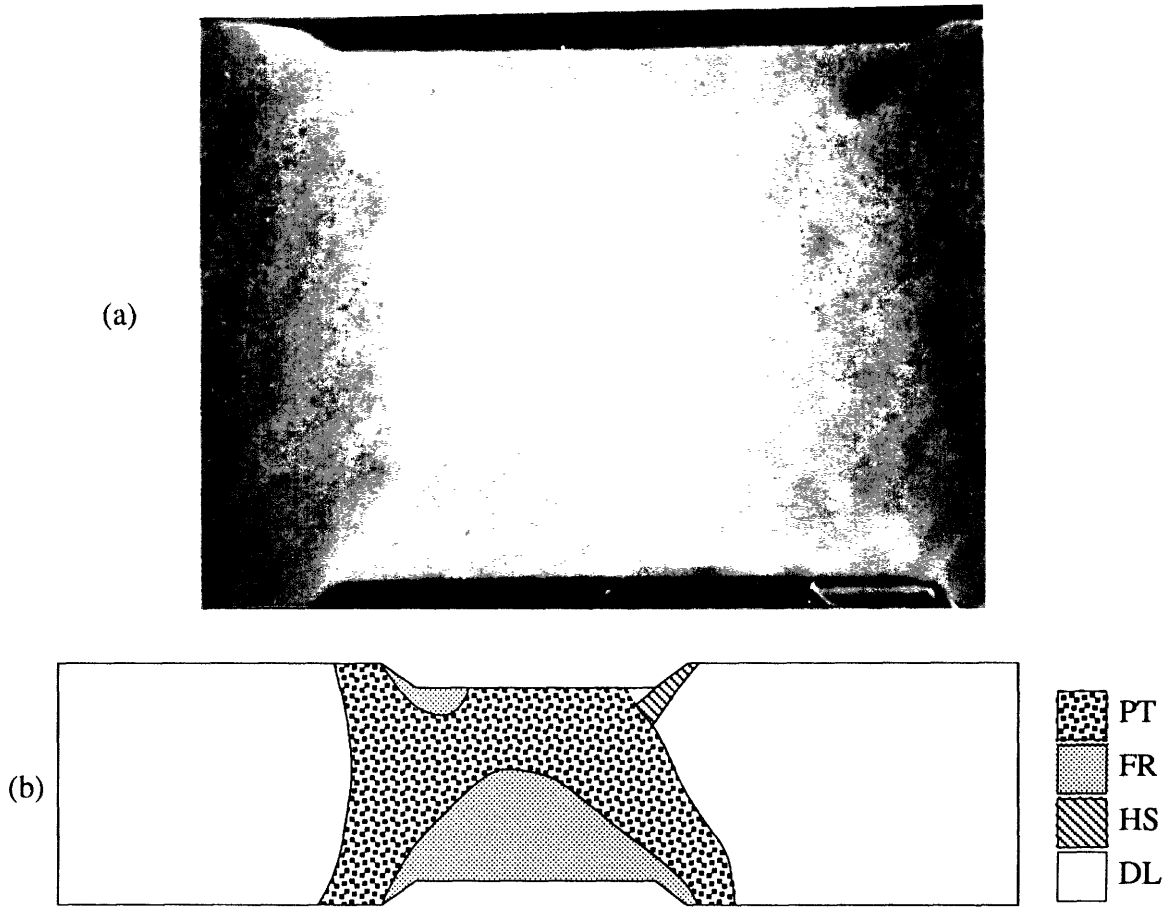

Fig. 4.5 704-2, 1300°F, 11.2%e, all, 15x. (a) The presence of HS, and DL grains among PT and FR grains of the S macrostructure. (b) Schematic of (a) clarifying areas of different microstructures.

4.1.2.4 Summary of Gleeble specimen recrystallization

The observations made here are summarized in the recrystallization map of Fig. 4.6. The expected result: increasing the test temperature, for a given strain level, generally causes recrystallization. Unexpectedly, however, increasing the strain at a

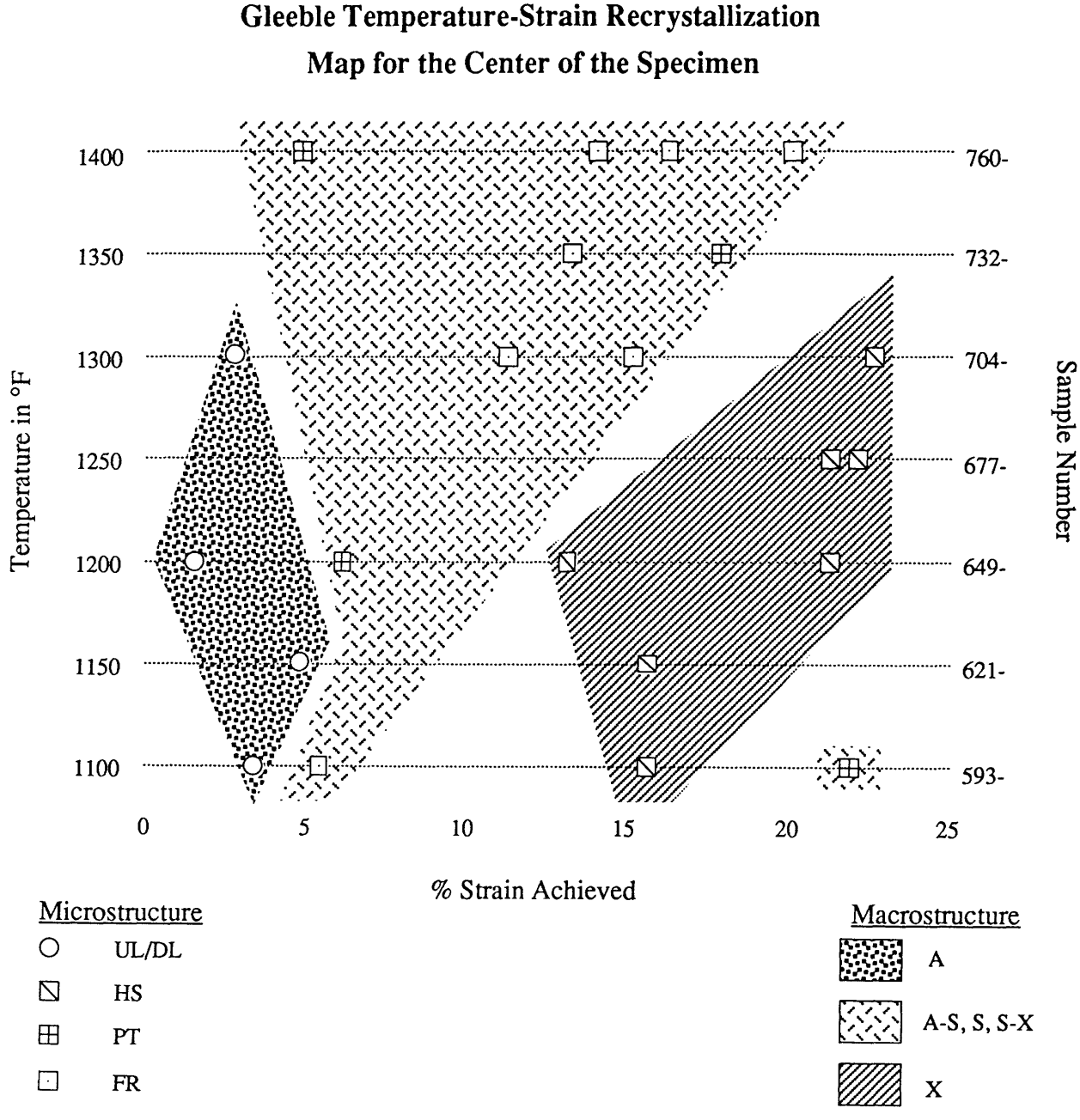

Fig. 4.6 Plot of microstructure at the specimen center for all samples at corresponding strain values and temperatures. The macrostructures fall on the map according to strain regimes. Note that asymmetric or mixed macrostructures are in S and not A or X.

given temperature may reduce recrystallization. Specifically, recrystallization occurred extensively at 1100°F with only 5.4% strain while at 1150°F, a strain of 4.8% had no affect on the microstructure and at 1200°F, a strain of 6.1% leads to recrystallization, but to a much lesser degree. Thus, it is possible that anvil cooling does not solely suppress HS grain recrystallization. Rather, the high strain level of these grains, relative to center grains, may slow recrystallization.

4.1.2.5 Gleeble grain hardnesses

All average Knoop hardness numbers of the microstructures fall within the specifications for Class L wheels. Of the microstructures, only FR grain hardness is scattered enough to approach the upper bound of 302 kgf/mm^2. The variation between microstructures is caused by the amount of strain (high dislocation density), grain size and volume fraction of iron carbide (pearlite), all being impediments to dislocation motion. Thus, the hardness should increase from UL to DL and HS since the strain increases and V_α decreases. The dip in hardness of the PT grains is caused by the higher V_α and the release of strain energy upon initializing transformation since the grain size shrinks. Also, the increase in FR grain hardness must be a result of the small grain size despite the increase in V_α and the release of all strain energy.

4.1.3 BRAKING EFFECTS AND THE HAZ

The combination of loads and heating in service drastically alter the microstructure of the tread surface (Fig. 4.7). Earlier it was reported that the HAZ contained spheroidite[36]. From a fracture standpoint, it would be beneficial to form spheroidite in the HAZ as this is the softest and most ductile form of carbide strengthened steel[32]. It is tough because it is composed of a continuous ferrite matrix. The samples observed have HAZ composed of short, randomly oriented plates that resemble pearlite, but the structure lacks ferrite (Fig. 4.7), and is, therefore,

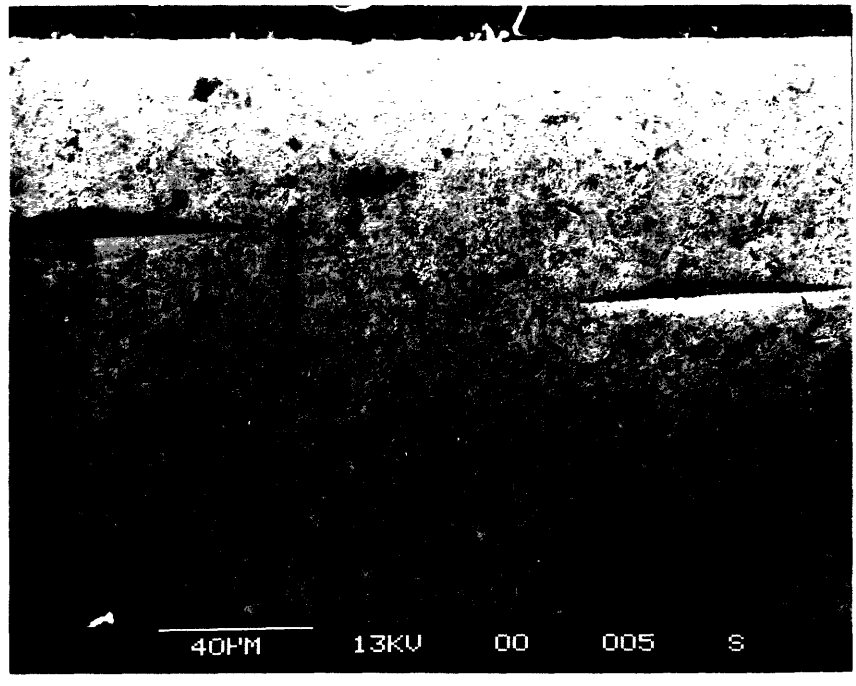

Fig. 4.7 Rolling surface of transverse plane of metallography sample 2S displaying the pearlite like microstructure (500x). The Knoop indentations had hardnesses of 456 and 442 kgf/mm^2.

brittle. The HAZ is similar to PT grains observed in Gleeble samples. The PT microstructure, however, has ferrite present and is soft. For comparison, the Knoop indentations shown in Fig. 4.7 have HK_{300} of 456 and 442 kgf/mm^2 while PT grains have an average HK_{300} of only 250 kgf/mm^2.

The HAZ developed during service may be hard. However, the hardness level obtained can vary widely (Fig. A1). Traverses of the metallography samples 2F and 2S illustrate this; indenting entirely within the HAZ gives an average HK_{300} with a large standard deviation (Table 3.4). The scatter is caused by variability in the HAZ depth. Fig. 4.8 plots the hardness at increasing distances from the tread surface. The transition through the HAZ is clearly indicated by the precipitous decline in hardness. The microstructure mimics this; the boundary between HAZ and the UL microstructure is well delineated (Fig. 4.9). Measuring the HAZ from micrographs and plotting the hardness at a depth of 0.05 mm from the surface shows a good correlation (Fig. 4.10). Apparently the hardness of the HAZ increases as the depth to which the microstructure is altered during service.

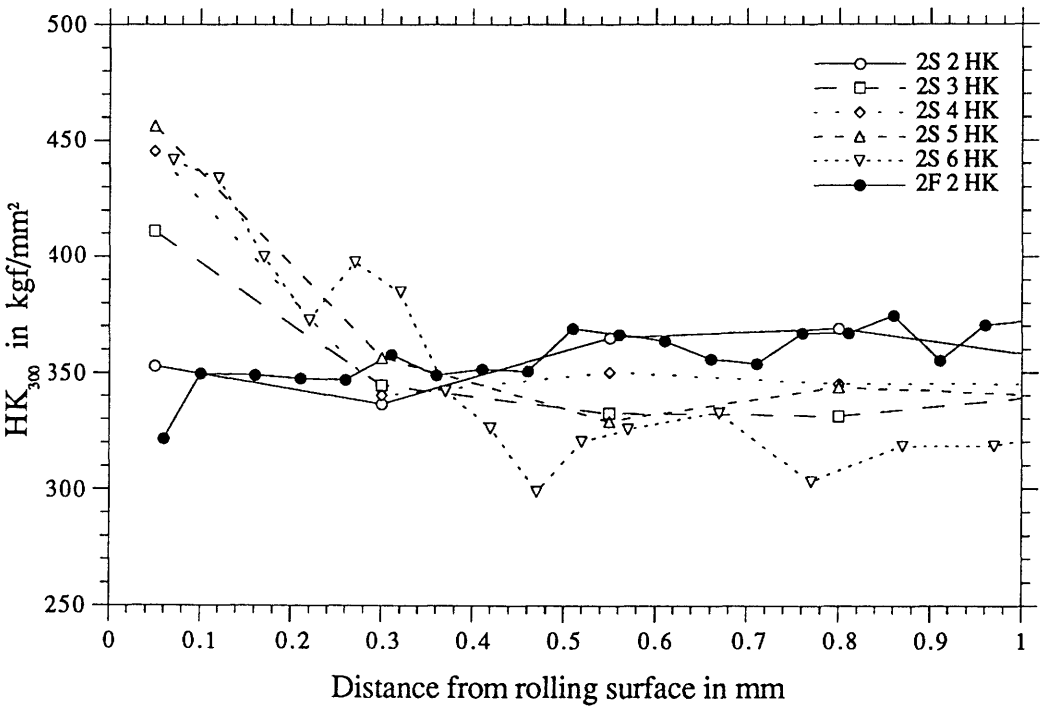

Fig. 4.8 Knoop microhardness traverses across the HAZ (RS(C-R)) of samples 2F and 2S.

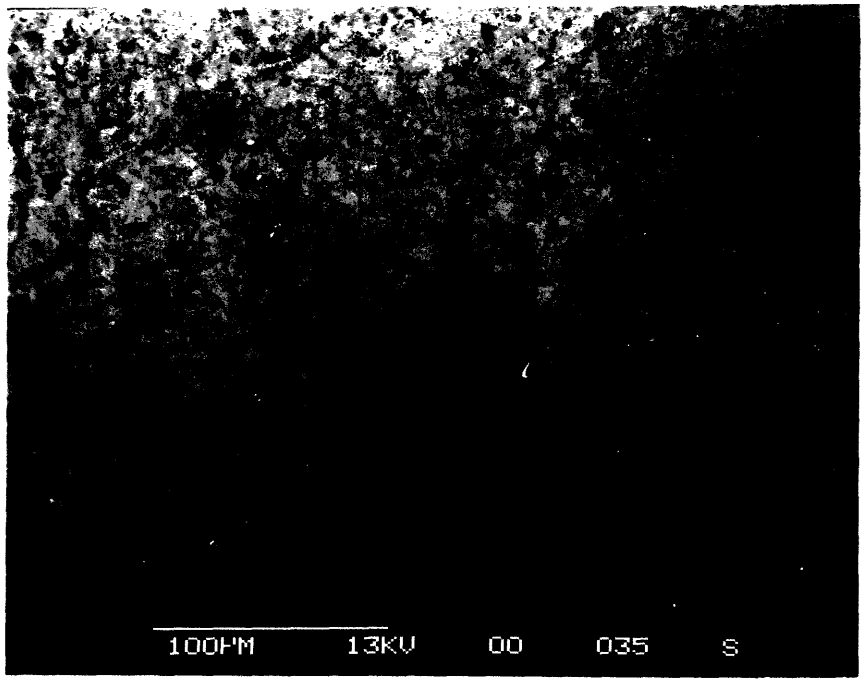

Fig. 4.9 SEM photomicrograph (310x) of the boundary between the HAZ and the parent ferritic-pearlitic microstructure.

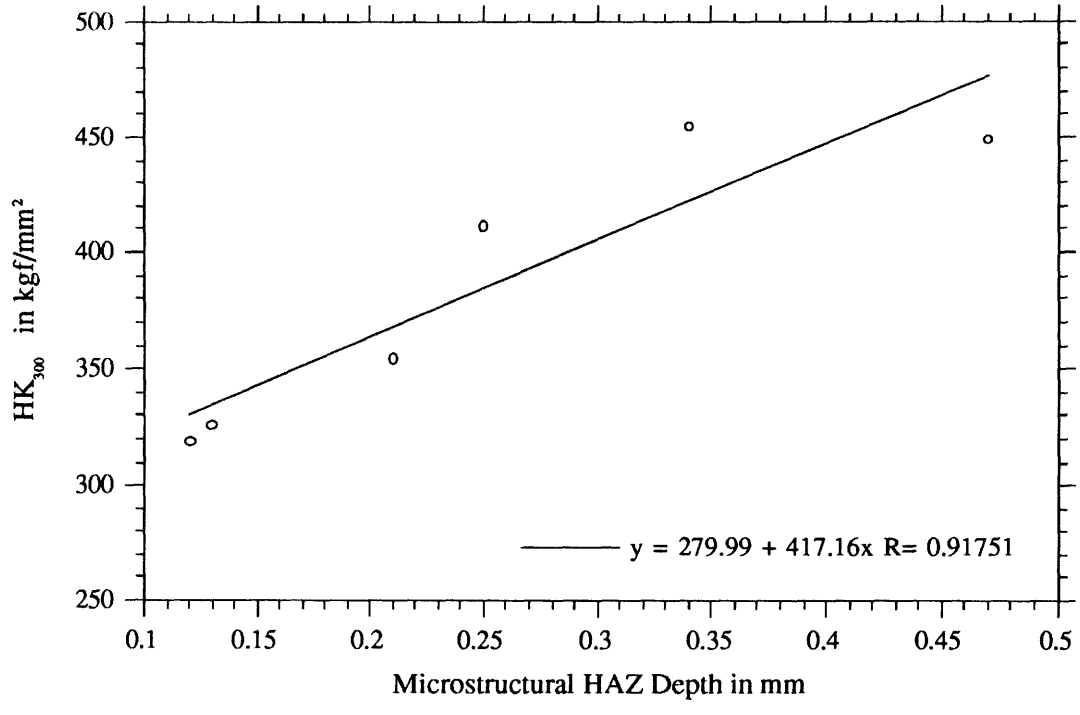

Fig. 4.10 Plot showing correlation between the depth of the HAZ and the hardness 0.05 mm beneath the tread surface.

4.2 CRITICAL CRACK SIZE PREDICTION

4.2.1 PLANE STRAIN FRACTURE TOUGHNESS ESTIMATIONS

Although all plane strain fracture toughness tests, save one, are invalid, the results obtained are useful. For example, specimen A1 exceeds the maximum load criterion by four percent. Also, the proportion of the fracture surface experiencing fast fracture by cleavage is eighty five percent. These two facts together indicate that although a valid K_{Ic} did not result, the critical K (K_c) at which the specimen did fracture is very close to the limiting plane strain value. The same is not true for the two high temperature specimens. In both cases, the maximum load exceeds the allowed limit by thirty percent or more. Although the shear lips are moderate, as evidenced by the proportion of fracture surface involved in oblique fracture per unit thickness (Prop in Table 3.9), the fracture surfaces contain a great deal more ductile fracture area than Prop accounts for. The fracture surface is nearly half void coalescence. Irwin determined a way to use K_{Ic} values to estimate the increase in fracture toughness of thin plates where plane strain conditions may not prevail[41]. The relation is:

$$K_c = K_{Ic}\sqrt{1+\frac{1.4}{B^2}\left(\frac{K_{Ic}}{\sigma_{lyp}}\right)^4} \qquad \text{eq. (4.1)}$$

The relation may also be used backwards: given a critical stress intensity for a plate of known thickness and yield strength, the plane strain fracture toughness may be calculated. Using tensile data and the K_Q values in Table 3.8, which are essentially K_c for the specimen geometry, plane strain fracture toughness values are solved for iteratively. The results of these calculations are listed in Table 4.1.

The CVN energy from impact tests may also be used for comparison with the invalid K_{Ic} test results. It has been determined that the standard CVN specimen has some

Table 4.1 Class L K_{Ic} values estimated from K_Q using the Irwin equation in ksi$\sqrt{in}$.

Sample	B2 0°F	A1 70°F	D1 70°F	D2 70°F	C1 150°F	C2 150°F
K_Q (K_c)	49.6 (K_{Ic})	63.5	60.3	65.9	66.8	68.5
Irwin K_{Ic}	—	55.7	53.7	57.1	57.5	58.5

constraint at the notch root such that plane strain conditions are partially imposed there. Also, temperature and strain rate affect K_{Ic} and CVN results similarly[42]. Because of these facts, the possibility of empirically relating K_{Ic} and CVN data exists, particularly for widely used steels. One correlation, taken from data on different types of steel, by Rolfe, Novak and Barsom is[42]:

$$\left(\frac{K_{Ic}}{\sigma_{lyp}}\right)^2 = 5\left(\frac{CVN}{\sigma_{lyp}} - 0.05\right) \qquad \text{eq. (4.2)}$$

where K_{Ic} is in ksi$\sqrt{in}$ and from slow loading rates, σ_{lyp} is in ksi, CVN is dynamic and in ft-lbs. and σ_{lyp} and CVN are both determined at the upper-shelf temperature. Since this is for upper-shelf temperatures, the toughness data will be less sensitive to loading rate and notch acuity than in the transition region. At upper-shelf temperatures, temperature and strain rate effects are small and eq. (4.2) can be used for steels with yield strengths less than 100 ksi.

In the transition region, the toughness data will be sensitive to loading rate and temperature. A relation which accounts for this is given by Barsom and Rolfe[42]:

$$K_{Id,T} = K_{Ic,T-T_{shift}} = \sqrt{5\ E\ CVN} \qquad \text{eq. (4.3a)}$$

$$T_{shift} = 215 - 1.5\sigma_{lyp} \qquad \dot{\varepsilon} \leq 10^{-4}\frac{1}{s} \qquad \text{eq. (4.3b)}$$

where K_{Id} is the dynamic plane strain fracture toughness in psi$\sqrt{in}$, E is Young's modulus in psi, CVN is in ft-lbs. and σ_{lyp} is taken at room temperature in ksi. The loading rate is accounted for by matching impact CVN data with dynamic K. Temperature is accounted for by noting that dynamic and static fracture toughness curves are similar but displaced along the temperature axis by T_{shift} of eq. (4.3b). Thus, conducting a Charpy test at temperature T will yield, via eq. (4.3a), a K_{Id} at temperature T which is also the K_{Ic} value at temperature ($T-T_{shift}$). Notch acuity can also be accounted for by changing the 5 in eq. (4.3a) to a 4 if a fatigue precracked CVN specimen is used.

There are also static K_{Ic} – impact CVN relations for the transition temperature region that do not account for strain rate effects:

Barsom and Rolfe[42]:	$K_{Ic} = \sqrt{2\ E\ CVN^{1.5}}$	psi-in, ft-lbs.	eq. (4.4)
Corten and Sailors[42]:	$K_{Ic} = 15.5\sqrt{CVN}$	ksi$\sqrt{in}$, ft-lbs.	eq. (4.5)
Roberts and Newton[42]:	$K_{Ic} = 9.35\ CVN^{0.63}$	ksi$\sqrt{in}$, ft-lbs.	eq. (4.6)

Results of calculations for all of the above equations are listed in Table 4.2. None of the equations is able to correlate the CVN of a 0°F test to the valid K_{Ic} of 49.6 ksi$\sqrt{in}$, all being off by 50% or more. Accounting for the temperature shift, eq. (4.3) predicts a K_{Ic} of 45.2 ksi$\sqrt{in}$ for 57°F, which in comparison to the valid 0°F K_{Ic} is too low. The only relationship which approaches the Irwin K_{Ic} is eq. (4.5) for 150°F.

Table 4.2 K_{Ic} values, in ksi$\sqrt{in}$, estimated by empirical relations from CVN tests, in ft-lbs, performed at room temperature. Eq. (4.2) is Barsom, Novak and Rolfe's. Eq. (4.3) is Barsom and Rolfe's and accounts for T_{shift} given in parenthesis. Eq. (4.4) is Barsom and Rolfe's. Eq. (4.5) is Corten and Sailors'. Eq. (4.6) is Roberts and Newton's[42].

Temp °F	CVN	eq. (4.2)	eq. (4.3)	eq. (4.4)	eq. (4.5)	eq. (4.6)
0	2.68	—	20.1 (88°)	16.2	25.4	17.4
70	9.44	46.7	38.1 (93°)	42.3	47.6	38.5
150	13.6	62.1	45.2 (93°)	54.9	57.0	48.3

It was noted in the results section that CVN tests conducted on a used Class L wheel have given much higher CVN values, 15 ft lbs, at 70°F[36]. The relationships presented here and the results of calculations listed in Table 4.2 indicate that the CVN of Table 3.7 are quite low. With this in mind, the K_{Ic} predicted by the Irwin equation will be used as plane strain fracture toughnesses.

4.2.2 CRITICAL CRACK LENGTH PREDICTIONS

Having an estimate of the plane strain fracture toughness allows for the calculation of critical crack sizes in the wheel which will cause failure for given stress levels. In a wheel peeling survey of used Class L wheels, the average crack depth for known surface crack lengths (a/c) is determined to be 0.443[43]. Because the crack front shape is elliptical, the stress intensity factor will be a function of the position along the crack front. To determine the critical crack size, the maximum stress intensity factor (K_{Imax}) along the crack front will be used. For a wheel with a center tread crack the stress intensity factor may be approximated as an infinite slab by[44]:

$$K_{Imax}=1.12\frac{\sigma\sqrt{\pi a}}{\varphi} \qquad \text{eq. (4.7)}$$

$$\varphi=\frac{3\pi}{8}+\frac{\pi}{8}\left(\frac{a}{c}\right)^2 \qquad \text{eq. (4.8)}$$

This equation can only be used for cracks which have depths less than half the rim thickness. For applied stresses (σ) of 40 and 50 ksi, eqs. (4.7) and (4.8) give critical crack sizes (a_c) of 0.49 and 0.31 inches, respectively. These would be cracks approximately 1.41 and 2.20 inches long at the surface. Following the convention of Carter and Caton, it is known that the yield stress of the wheel may be reached and that a_c for σ=81.6 ksi should be determined[45]. Under these conditions, a_c will shrink to 0.12" with a surface length of 0.53". For cracks that initiate at the front rim edge, a/c is assumed to be unity and eq. (4.7) is altered by squaring 1.12[46]. Applying similar conditions as for center tread cracks, c_c=a_c for rim edge cracks becomes 0.96, 0.62 and 0.23 inches for σ of 40, 50 and σ_{lyp} ksi. This implies that front edge rim cracks are more dangerous since catastrophic failure can result at similar stress levels for much shorter cracks.

4.3 FRACTOGRAPHY

4.3.1 STRETCH ZONE IN PLANE STRAIN FRACTURE TOUGHNESS SPECIMENS

SEM fractography shows the initial catastrophic crack growth to be comprised of several regions. A fatigue precracked sample is assumed to have the sharpest possible crack tip. Upon initial loading of the body, the crack opens by plastically blunting as a result of double shear sliding at the crack tip. On the fracture surface, this appears as a

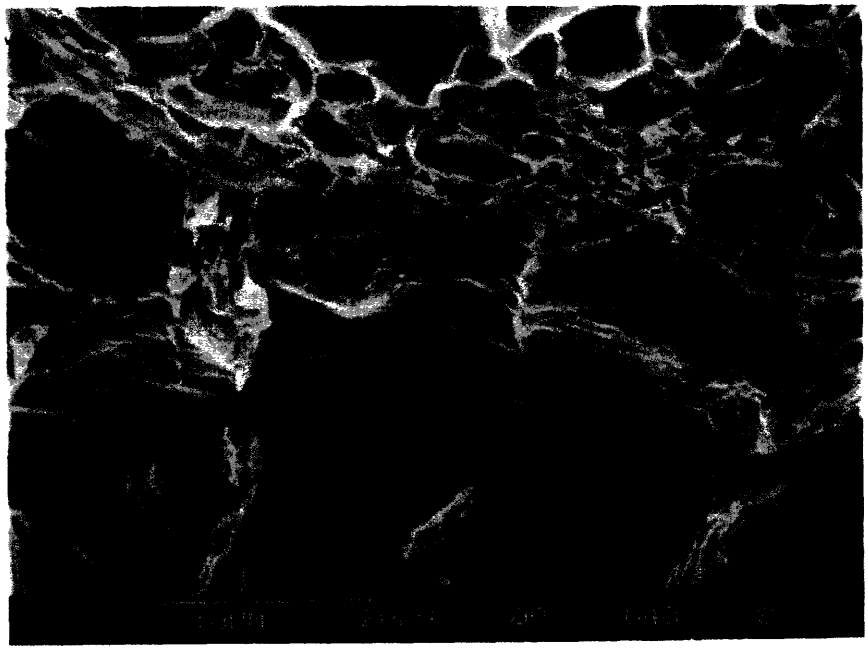

Fig. 4.11 SEM microfractograph of sample D2 tested at 70°F showing the fatigue precrack at bottom followed by the stretch zone (width of 7-10 microns) running diagonally across the frame. Crack propagated from bottom to top. (2800x)

large striation or slip band which is known as the stretch zone (Fig. 4.11). Kobayashi and Nakamura determined the stretch zone widths (SZW), for iron, copper, titanium and aluminum alloys, to be functions of J/E[47]. Since J and K are related in linear elastic fracture mechanics, their function can be rewritten in terms of K as follows:

$$SZW=89(1-\nu^2)\left(\frac{K}{E}\right)^2 \qquad \text{eq. (4.9)}$$

The ninety percent confidence interval limits for eq. (4.9) are given by replacing 89 by 54.7 and 143. Using the Irwin K_{Ic} data generated by eq. (4.1) and the temperature dependence of Young's modulus over the range of testing[33], the SZW and confidence interval can be determined for each sample. The results of these calculations are listed in Table 4.3. The SZW observed in the samples in the SEM falls in the range predicted by eq. (4.9).

Table 4.3 The expected stretch zone width in microns calculated from the Irwin K_{Ic} using Kobayashi and Nakamura's eq. (4.9) along with the 90 percent confidence interval, in parenthesis. The measured SZW, in microns, from SEM micrographs is also tabulated.

Sample	Irwin K_{Ic}	SZW (calc)	SZW (obs)
B2 0°F	49.6 (valid)	5.2 (3.2-8.4)	4-12
A1 70°F	55.7	6.7 (4.1-10.8)	—
D1 70°F	53.7	6.2 (3.8-10.0)	—
D2 70°F	57.1	7.1 (4.3-11.3)	7-11
C1 150°F	57.5	7.4 (4.5-11.8)	5-17
C2 150°F	58.5	7.6 (4.7-12.2)	—

After initial loading of the specimen which causes the crack tip to blunt, additional loading causes the crack to advance by the coalescence of voids formed during and after plastic blunting of the crack tip. This can be seen in Fig. 4.12. The fatigued region of the precrack is in the lower left hand corner of the micrograph followed by the SZW and the dimpled appearance of the coalesced voids. While SZWs followed by dimpled fracture are present in all samples, they are not necessarily present along the entire fatigue precrack front of a single sample. For example, at 0°F, Fig. 4.13 shows the fatigue precrack along the bottom of the fractograph with a few areas having SZWs and dimples while some of the front immediately enters fast fracture by transgranular cleavage. This intermittent behavior is found in samples B2 and D2, but not C1. In C1, it is found that SZWs and especially the dimpled fracture extended entirely across the sample. Indeed, both 150°F samples experienced a popin, initial crack growth at the midpoint of the crack front (where plane strain conditions are present) that was arrested by the constraint of material of the sample edges (where plane stress conditions are present). The widest point of the popins are 3.5 and 0.4 mm for C1 and C2 respectively.

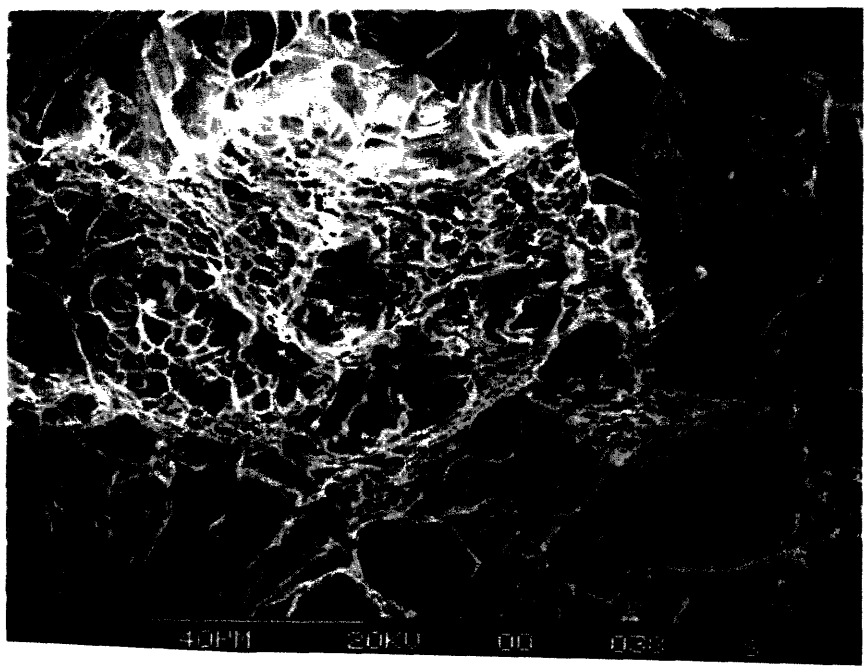

Fig. 4.12 Overview of the fracture surface shown in Fig. 4.11. This shows the presence of a region which fractures via nucleation, growth and coalescence of voids immediately following the stretch zone. (713x)

Beyond the SZW and dimpled regions, fracture occurs primarily by transgranular cleavage (Fig. 3.13). This occurs in the interior of the fracture surface which is in plane strain. Near the edges of the sample, which is in plane stress, fracture occurs by the nucleation, growth and coalescence of voids (Fig. 3.14) forming at either inclusions or, primarily, cementite. This fracture mechanism, being driven by dislocation motion, is

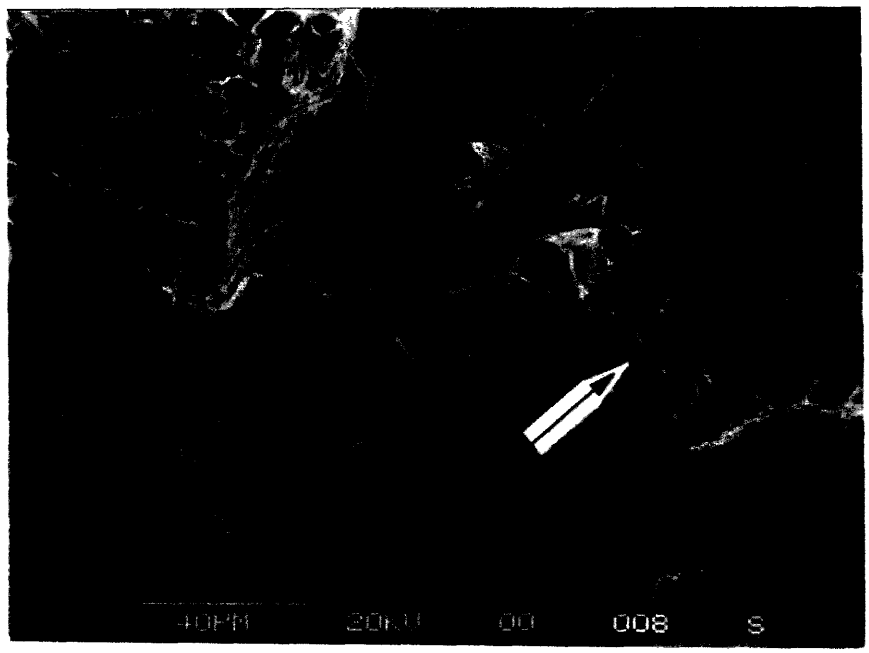

Fig. 4.13 The arrow indicates a region of fracture in sample B2 tested at 0°F which formed neither a stretch zone nor dimples between the fatigue precrack and cleaved fast fracture surface.

most prevalent on the planes of maximum shear. For the plane stress regions of the sample edges, these planes are angled 45° to the crack plane and give rise to an inclined shear lip which runs along the edges of the sample. It should be noted that for sample B2, the shear lips are not continuous.

4.3.2 FATIGUE STRIATIONS

Failure analysis utilizes the fatigue striation spacing (FSS) left on fracture surfaces to reconstruct the crack growth sequence of a component[48]. To accomplish this, a correlation must be established between the FSS and macroscopic crack growth rates (da/dN). An attempt to determine this relationship for Class L steel was unsuccessful. Shown in Fig. 3.17 are fatigue striations from high da/dN on the order of $5 \cdot 10^{-4}$ inch/cycle. For comparison, striations developed at da/dN of around $4 \cdot 10^{-5}$ inch/cycle are shown in Fig. 4.14. The only significant difference is the length to which lower da/dN striations are able to extend across the microstructure. Extensive FSS measurements were made across the fracture surface of sample F. Comparing the FSS to da/dN measured by compliance shows no correlation (Fig. 4.15). Indeed, the FSS are approximately constant at 1.34 microns ($CI_{95\%}$=0.16, RAC=12.1%).

In a study of pearlitic rail steels, several micromechanisms for fatigue crack propagation are given[49]. One mechanism involves a monotonic ductile rupture process involving pearlite lamellae[50]. Oriented correctly, rupture through a pearlite colony has a fracture surface similar to fatigue striations. In the sample studied on the SEM,

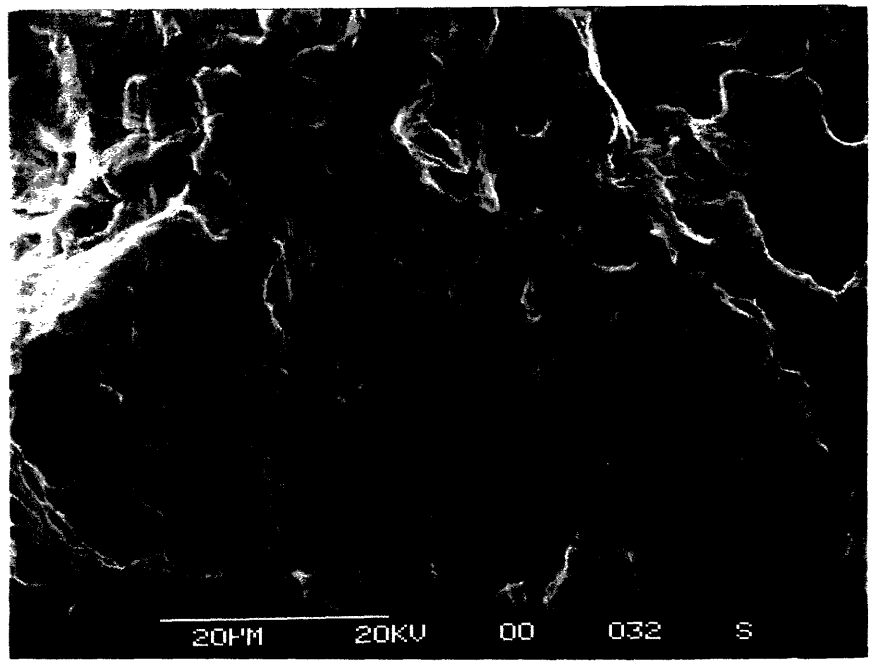

Fig. 4.14 Striations formed in sample F under COD controlled ΔJ_{eff} testing at a macroscopic crack growth rate of approximately $4 \cdot 10^{-5}$ $^{in}/_{cycle}$ (growth is from bottom to top). (1500x)

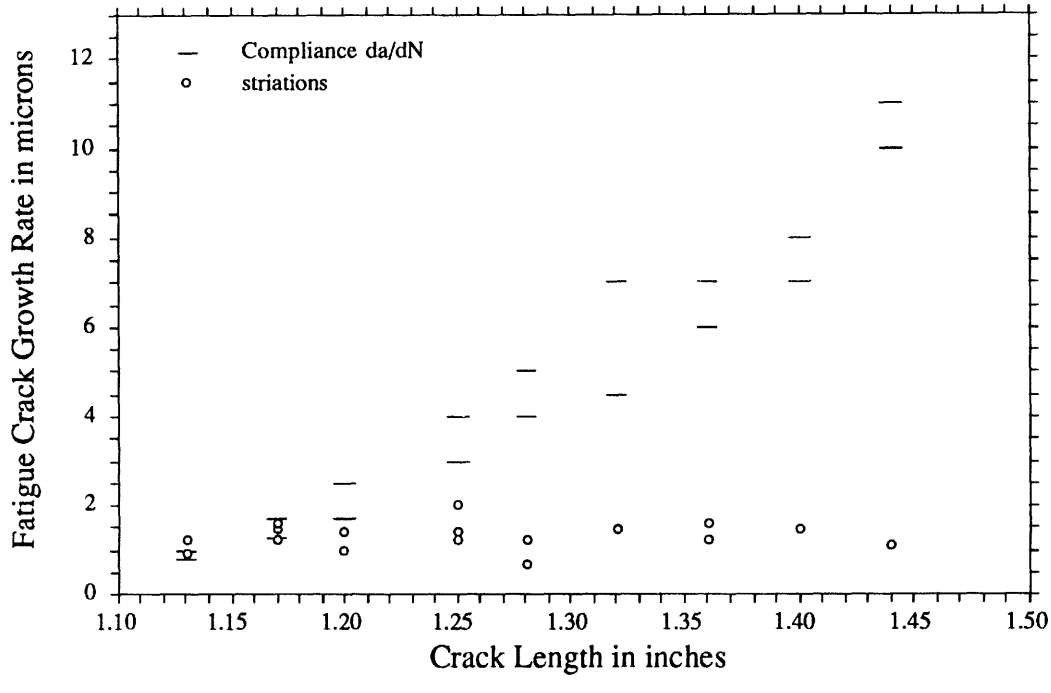

Fig 4.15 Comparison of the fatigue striation spacing to the macroscopic crack growth rate in sample F.

individual pearlite lamellae striations are not observed, the FSS being too large. However, due to the large plastic zone and secondary cracking, it is hypothesized that groups of three or four lamellae comprise a single FSS.

4.4 APPROXIMATE LIFE PREDICTION

A constant fatigue striation spacing for various levels of cyclic stress intensity precludes the cycle counting method for life prediction of a component. Knowing the material's resistance to fatigue crack propagation, i.e. the da/dN as a function of applied cyclic stress intensity factor, allows a life prediction by means of integration. From the results section, da/dN for all samples tested is:

$$\frac{da}{dN} = 1.01 \cdot 10^{-10} (\Delta K_{eff})^{3.51} \qquad \text{eq. (4.10)}$$

The da/dN-ΔK_{eff} relation is used despite significant amounts of plasticity (measured as the ratio of plastic to total cyclic J-integral range), exceeding 20% for some tests, because a good correlation exists and, also, the use of ΔK_{eff} rather than ΔJ_{eff} will predict higher crack growth rates for the same nominal loading conditions. This results in a measure of safety in the calculations.

4.4.1 DETERMINATION OF SERVICE CYCLIC STRESS

The only unknown quantity in eq. (4.10) assuming cracks grow with a constant aspect ratio of a/c=0.443, is the stress range braking subjects the wheel to. A wheel failed by a rim edge crack with a=0.91" and a/c=0.518 (it was not semicircular). The rim thickness (t) has been reduced by wear and truing operations to 1.31", disallowing the use of eqs. (4.7) and (4.8). Instead eq. (4.11), which accounts for the high a/t ratio, is used[35]:

$$K_I = 1.12 \sigma F \sqrt{\frac{\pi a}{Q}} \qquad \text{eq. (4.11)}$$

where the additional factor of 1.12 is due to the failed crack being a corner crack. The parameters F and Q account for elliptical crack shape, the extent of cracking along the tread surface and its depth. Substituting the K_{Ic} value for 150°F and the appropriate crack size and aspect ratios yields an applied stress of 32 ksi at failure.

4.4.2 CENTER TREAD AND RIM FRONT CRACK GROWTH

Calculations to determine the number of braking cycles to failure for a center tread crack integrate eq. (4.10) between an initial crack size (a_i) determined by the limits of visual inspection and final crack sizes (a_f) determined by a_c given in section 4.2.2. This models the loading history as a series of uniform brakings which produce a cyclic crack opening stress of 32 ksi to drive the crack growth and ultimate failure caused by a random overload at the corresponding critical crack size. To determine the life the alternating stress which has both tensile and compressive components will be assumed to have crack closure at zero stress. Thus the magnitude of ΔK_{eff} is proportional to 32 ksi.

Integration of eq. (4.10) using eqs. (4.7) and (4.8) to approximate the stress intensity factor for a wheel with a thick tread or short surface crack (i.e., a/t<0.5) yields:

$$\Delta N = 1.31 \cdot 10^{10} \left(\frac{\varphi}{1.12 \Delta\sigma \sqrt{\pi}} \right)^{3.51} \left(\frac{1}{a_i^{0.755}} - \frac{1}{a_f^{0.755}} \right) \qquad \text{eq. (4.12)}$$

This gives the number of braking cycles (ΔN) required to drive a crack between a_i and a_f at a cyclic stress level of $\Delta\sigma$, assuming the crack growth is self-similar (a/c and, therefore, φ constant). For center cracked treads, it is assumed a surface crack length of 0.5" is easily detected which gives a_i=0.111" for aspect ratio of a/c=0.443. The corresponding life is calculated for $\Delta\sigma$=32 ksi with a_f=a_c determined by the random overload stresses (σ_o) and is tabulated in Table 4.4.

Table 4.4 The number of braking cycles to failure (ΔN) given an initial crack depth of 0.111" where failure is determined by a random overload (σ_o) and its corresponding critical crack length (a_c) for center tread cracks.

	Cyclic	Stress
σ_o and a_c	$\Delta\sigma$ = 32 ksi	$\Delta\sigma$ = 40 ksi
40 ksi 0.49"	48600	16800
50 ksi 0.31"	38900	13400
81.6 ksi 0.12"	4250	1470

During fatigue testing the closure load is not necessarily zero. For rising ΔK_{eff} tests where the nominal load ratio is fixed at R of -0.5 or -1.0, the closure load will be positive initially. As the crack length grows, the closure load becomes negative and at test end, the closure load ratio (R_{cl}=P_{cl}/P_{max}) may be -0.25. This is also true for COD controlled rising ΔJ_{eff} tests. This knowledge is applied to growing cracks in train wheels by increasing $\Delta\sigma$ by 25% but assuming K_{max} to remain the same. Calculations showing the decrease in ΔN due to negative R_{cl} are listed in Table 4.4 and predictions show that 70% of the life may be lost.

Corresponding life predictions were performed for the case where a corner crack at the rim front edge is subjected to similar loading conditions as above. Integration of eq. (4.10) for a rim edge crack with a/c of unity gives the number of cycles to failure as:

$$\Delta N = 1.31 \cdot 10^{10} \left(\frac{\sqrt{\pi}}{2.51 \Delta\sigma} \right)^{3.51} \left(\frac{1}{a_i^{0.755}} - \frac{1}{a_f^{0.755}} \right) \qquad \text{eq. (4.13)}$$

Calculations for loading conditions are those used for center cracks above. It is assumed that inspection can resolve surface cracks of length a_i=0.118" and catastrophic failure occurs at a_c determined in section 4.2.2 for random overloads. The results of these calculations are given in Table 4.5.

Table 4.5 The number of braking cycles to failure (ΔN) given an initial crack depth of 0.111" where failure is determined by a random overload (σ_o) and its corresponding critical crack length (a_c) for rim edge cracks.

	Cyclic	Stress
σ_o and a_c	$\Delta\sigma$ = 32 ksi	$\Delta\sigma$ = 40 ksi
40 ksi 0.96"	80500	36800
50 ksi 0.62"	72100	33000
81.6 ksi 0.23"	40200	18400

5.0 CONCLUSIONS

5.1 PRODUCTION PROCESS AND SERVICE EFFECTS

Forging operations do not impart any anisotropicity to the wheel microstructure as the grains are equiaxed with respect to the wheel. The quench treatment of the steel prevents the formation of proeutectoid ferrite in amounts commensurate with the Fe-Fe_3C equilibrium phase diagram. The quench affects the microstructure by forcing the growth of Widmanstätten side plates from proeutectoid ferrite grain boundary allotriomorphs in Class L steel. It is thought that the presence of Widmanstätten plates may be an indicator of the zone of compressive residual stress resulting from the quench. Class A steel can be hardened slightly more than Class L but Class L is able to harden a larger section of the rim. Service conditions harden the wheel, improving its wear resistance, beyond that of the quench but simultaneously removes the beneficial compressive residual stress. At the tread surface, the heat affected zone can increase the hardness by 25% over that of the material immediately outside the zone. The heat affected zone is composed entirely of a pearlite-like microstructure, is brittle and susceptible to cracking. The high hardness of the heat affected zone at a depth of 0.05 mm from the surface correlates with the depth of the heat affected zone microstructure into the tread at that point.

5.2 GLEEBLE COMPRESSION TESTS

Monotonic hot compression of Class L steel is unable to accurately reproduce the microstructure of the heat affected zone in terms of morphology, volume fraction of microconstituents and hardness. Hot compression transforms the parent microstructure of Class L steel into 4 distinct microstructures. The location of these microstructures within a sample correlates with the macrostructure observed by the naked eye. Unexpectedly, recrystallization in Class L steel can be suppressed by increasing the amount of strain at a given temperature. Recrystallization and the subsequent macrostructures formed are complicated by tantalum induced recrystallization, sample cooling by compression anvils and specimen bending during testing.

5.3 MECHANICAL BEHAVIOR

The tensile tests of Class L steel confirmed reported strengths to be low. Charpy impact tests show the Class A steel is tougher than Class L. Plane strain fracture toughness tests of Class L steel did not yield valid K_{Ic} values at temperatures other than 0°F. At the higher temperatures, K_{Ic} is estimated using K_Q values and the Irwin equation. Empirical relations correlating Charpy impact energy to K_{Ic} give poor results. The resistance to fatigue crack growth for Class L steel correlates well with ΔJ_{eff} as well as ΔK_{eff} despite significant plasticity at the crack tip. Consequently, determination of valid

specimen sizes for cyclic data must account for the strain hardening capacity of the steel through the use of the flow stress in calculations.

5.4 FRACTOGRAPHY

A stretch zone is formed upon initial loading of plane strain fracture toughness specimens at all temperatures tested. The stretch zone width is found to correlate well with a Kobayashi and Nakamura's semi-empirical equation. Although striations exist, they are found to have a constant spacing over a wide range of macroscopic, compliance measured fatigue crack growth rates. Use of compact tension specimens in fully reversed cycling results in fatigue crack initiation and growth from the back face of a specimen at the stress concentration produced by side grooves.

5.5 CRITICAL CRACK SIZE AND LIFE PREDICTIONS

Under identical loading conditions, calculations reveal critical surface crack sizes for rim edge cracks to be smaller than those for center tread cracks. However, the rim edge cracks require more braking cycles to reach critical crack lengths. Accounting for possible compressive closure stresses in the wheel illustrates that a 25% increase in the crack driving force can reduce the expected life by approximately 65%. Caution must be applied in estimating the life of various cracks. The rim edge crack requires more cycles to fail primarily because the initial crack size is smaller than a center tread crack and the sensitivity of the life equation to this geometric parameter. The lives calculated also assume very uniform brake applications and neglect the possibility of life reduction via the initiation and subsequent arrest of an unstable crack due to a harsh, but noncatastrophic, stop.

6.0 RECOMMENDATIONS

In test simulations monotonic hot compression is unable to produce the heat affected zone. Similar testing involving cyclic hot compression under more severe plastic flow constraints may be able to reproduce the effects.

The hoop stress in the wheel arises from a temperature distribution driven elastic and plastic strain gradient of the tread surface, the rim and the plate. High temperature tensile properties of the steel should be determined. Use of these properties in finite element simulations may be able to accurately predict the quench residual stresses and, more importantly, the crack opening stress due to braking.

The life predictions made are based on the steel's mechanical behavior at room temperature and applied to a high temperature situation. If possible, fatigue tests conducted at high temperatures would give more realistic crack propagation lives. In conjunction with this, high temperature J-integral testing should be used to characterize the steel's catastrophic crack initiation behavior to accurately predict critical crack sizes.

APPENDIX

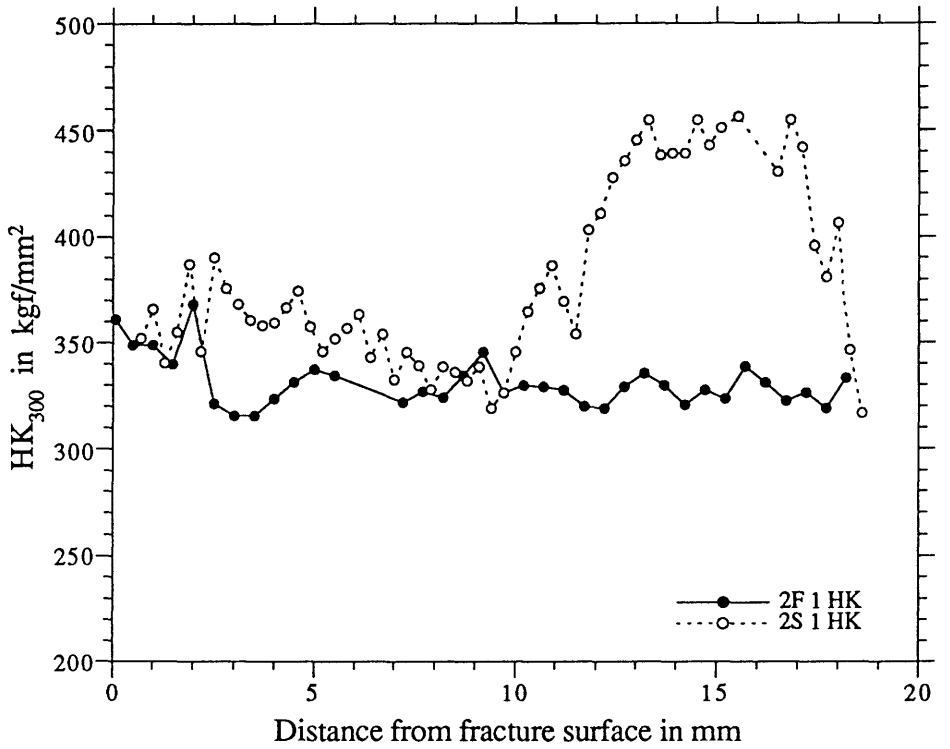

Fig. A1 Traverse TS(T-C) of Knoop microhardness indentations (HK_{300}) 0.05 mm below the tread surface in the circumferential direction within the HAZ.

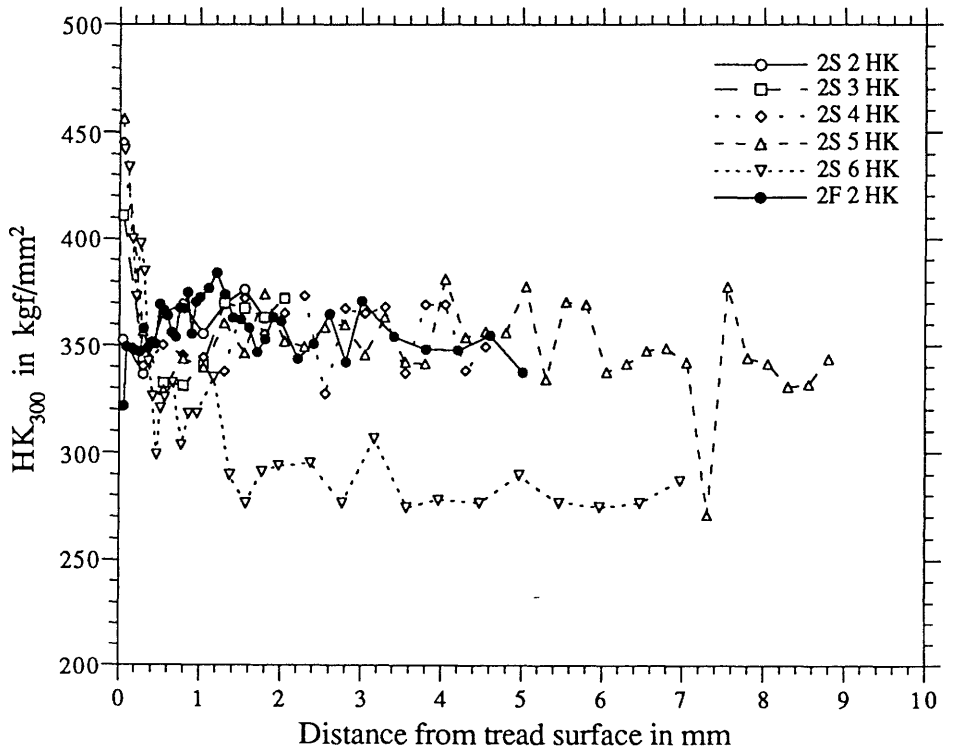

Fig. A2 Traverse TS(T-R) away from the tread surface passing through the HAZ.

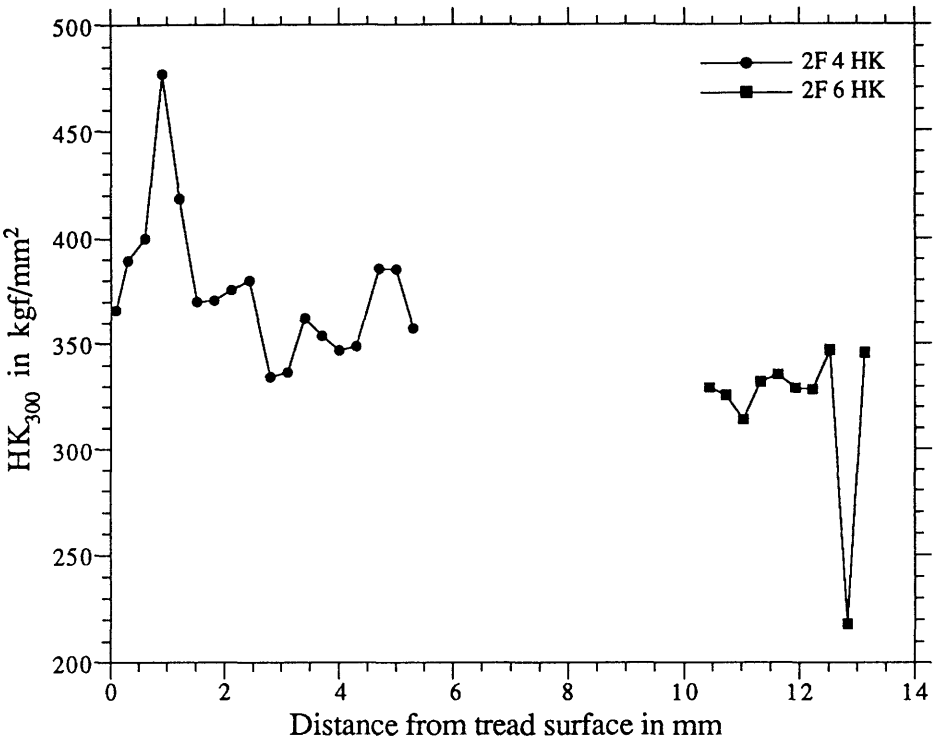

Fig. A3 Traverse FS(T-R) of Knoop indentations along the fracture surface.

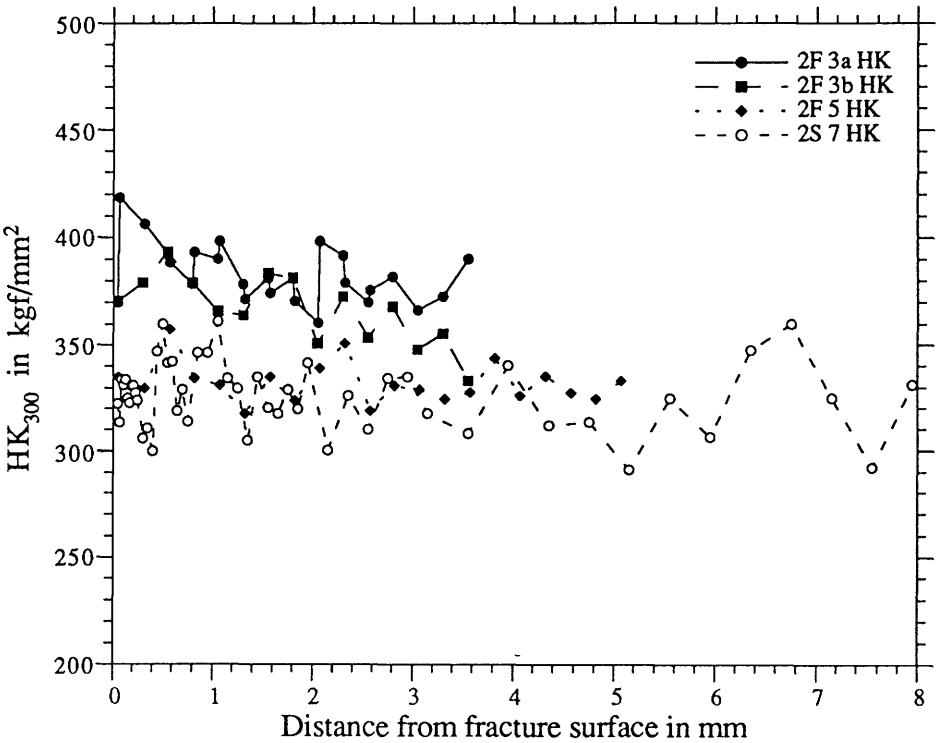

Fig. A4 Traverse FS(T-C) of indentations away from the fracture surface.

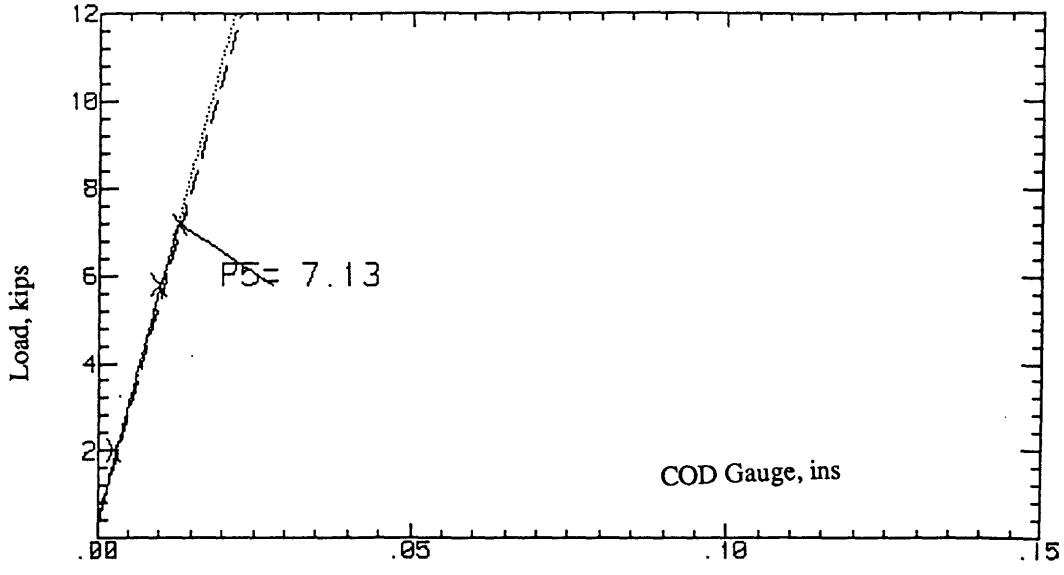

Fig. A5 Plot of the load versus front face displacement curve for K_{Ic} specimen B2 tested at 0°F.

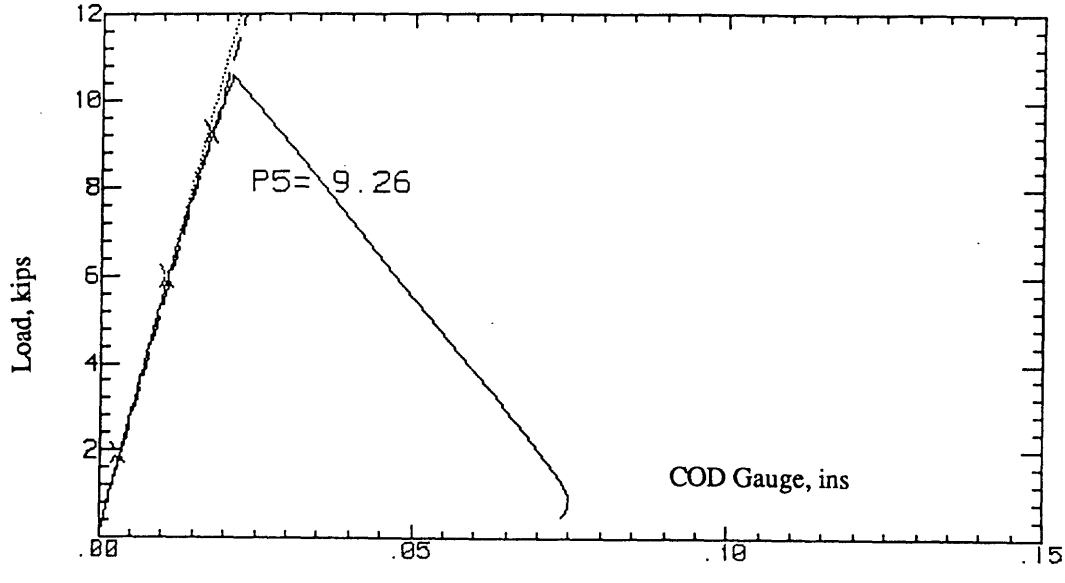

Fig. A6 Plot of the load versus front face displacement curve for K_{Ic} specimen A1 tested at 70°F.

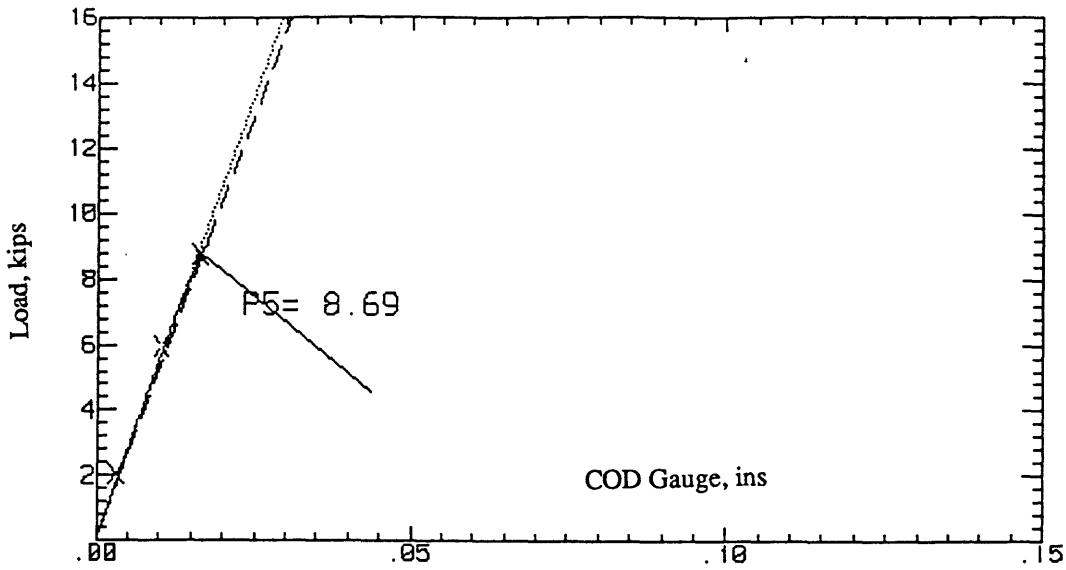

Fig. A7 Plot of the load versus front face displacement curve for K_{Ic} specimen D1 tested at 70°F.

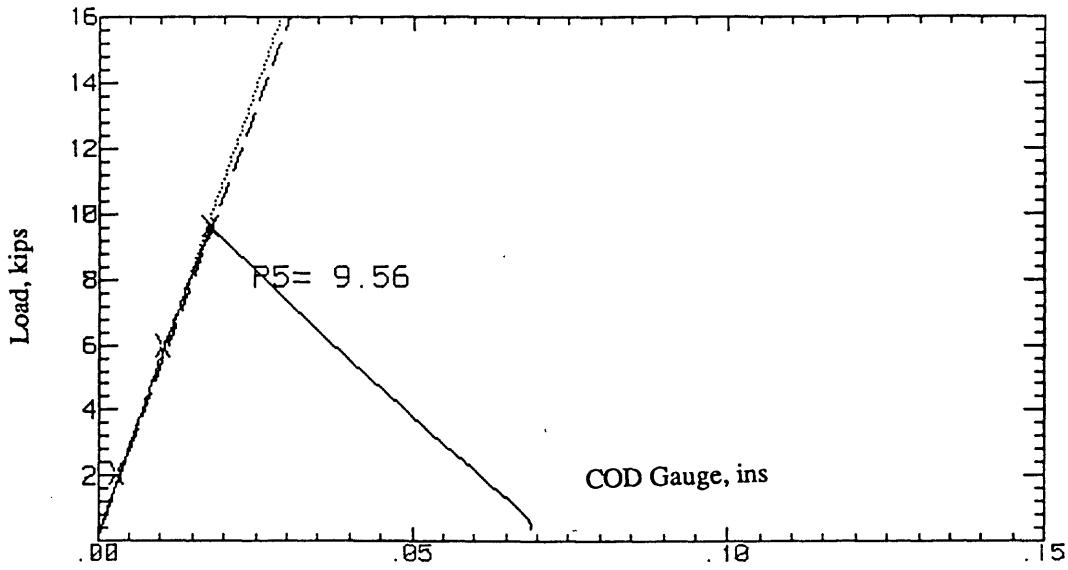

Fig. A8 Plot of the load versus front face displacement curve for K_{Ic} specimen D2 tested at 70°F.

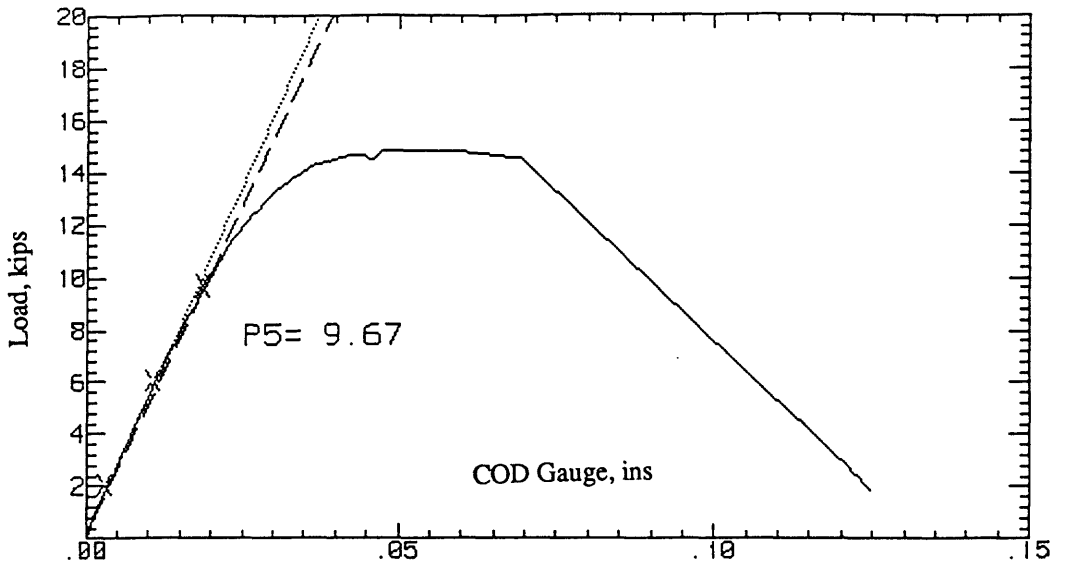

Fig. A9 Plot of the load versus front face displacement curve for K_{Ic} specimen C1 tested at 150°F.

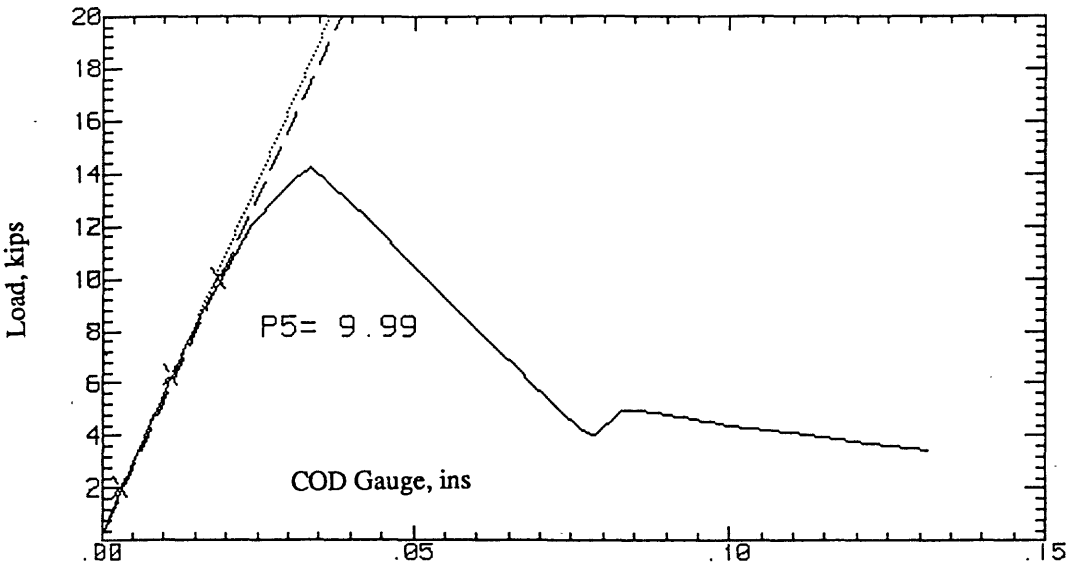

Fig. A10 Plot of the load versus front face displacement curve for K_{Ic} specimen C2 tested at 150°F.

REFERENCES

[1] Statement of Work, *"Metallographic Examination of Railroad Components: Thermally Cracked Wheels and Failed Stub Sills,"* Contract Number DTRS-57-88-C-00078, Technical Task Directive No 43, October 1991, 3-7.

[2] O.Orringer, D.E.Gray and R.J.McCown, *"Evaluation of Immediate Actions Taken to Deal with Cracking Problems Observed in Wheels of Rail Commuter Cars,"* VNTSC, Cambridge, MA and FRA, Washington, D.C., report no. FRA/ORD-93/15, July 1993, 1-37.

[3] Field Manual of the Interchange Rules, Operations and Maintenance Department, Mechanical Division, AAR Washington, D.C., 1984, Rule 41-Section A.

[4] The Making, Shaping and Treating of Steel, edited by W.T.Lankford Jr., N.L.Samways, R.F.Craven and H.E.McGannon, United States Steel Corporation, Pittsburgh, PA, 1985, 1373.

[5] Annual Book of ASTM Standards Vol. 01.04, Standard Test Method A504-89, ASTM, Philadelphia, PA, 1992, 302-8.

[6] S.A.Perfect, *"Stress Changes in Railroad Car Wheels Due to Axially Symmetric Thermal Loads,"* Ph.D Thesis, University of Illinois at Urbana-Champaign, 1986, 1-60.

[7] C.S.Carter and R.G.Caton, *"Fracture Resistance of Railroad Wheels,"* Report FRA-ORD-75-12, April 1967, 1-46.

[8] E.J.Ripling and P.B.Crosley, *"Thermal Cracking of Railcar Wheels,"* Materials Research Laboratory, Inc., Glenwood, IL, 1-8.

[9] C.Q.Bowles and J.R.Roland, *"Comparison of the Fracture Behavior of Conventional Class U Railway Wheels and an Experimental Alloy Wheel,"* Mechanical and Aerospace Engineering Department, University of Missouri, 1-24.

[10] J.M.Wandrisco and F.J.Dewez, *"Service Defects in Treads of Railroad Wheels During Service,"* ASME paper 60-RR-1, 1960.

[11] H.R.Wetenkamp, O.M.Sidebottom and H.R.Schrader, *"The Effect of Brake Shoe Action on Thermal Cracking and on Failure of Wrought Steel Railway Car Axles,"* University of Illinois, Experimental Engineering Station Bulletin 387, 1950.

[12] M.Yontar, *"A Modern Approach to Evaluating Operating Plate Stresses in 28 Inch Reversed Disk Wrought Steel Wheels on Transit Cars,"* Proceedings of the Third International Congress on Wheelsets, Sheffield, UK, 1969.

[13] M.Balzer, H.Sehitoglu and G.J.Moyar, *"An Inelastic Finite Element Analysis of the Contribution of Rail Chill to Braked Tread Surface Fatigue,"* Rail Transportation, ASME, 1992, 117-122.

[14] H.R.Wetenkamp, *"Thermal Checking of Wrought Steel Railway Wheel Material,"* Transactions of the AIME, May, 1954, 649-654.

[15] D.H.Stone and G.J.Moyar, *"Wheel Shelling and Spalling - an Interpretive Review,"* Rail Transportation, ASME, 1989, 19-31.

[16] D.H.Stone, G.J.Moyar and T.S.Guins, *"An Interpretive Review of Railway Wheel Shelling and Spalling,"* Rail Transportation, ASME, 1992, 97-103.

[17] G.J.Moyar and J.Morrow, *"Surface Failure of Bearings and Other Rolling Elements,"* University of Illinois, Experimental Engineering Station Bulletin 468, 1964.

[18] M.T.Gallagher, M.A.Polzin and C.D.Christie, *"Railroad Wheel Flange Failures: Causes and Preventions,"* Rail Transportation, ASME, 1992, 155-163.

[19] Atlas of Stress Strain Curves, H.E.Boyer, Ed., ASM, Metals Park, OH, 1987, 193.

[20] Annual Book of ASTM Standards Vol. 03.01, ASTM, Philadelphia, PA, 1992, 302-8.

[21] N.Ridley, *"A Review of the Data on the Interlamellar Spacing of Pearlite,"* Metallurgical Transactions A, Volume 15A, June 1984, 1019-36.

[22] P.Clayton, *"Hot Compression Tests on the Gleeble 1500,"* Oregon Graduate Institute of Science and Technology, Beaverton, OR, November, 1992.

[23] S.Suresh, Fatigue of Materials, Cambridge Solid State Science Series, 1992, 5-6.

[24] N.E.Dowling and J.A.Begley, *"Fatigue Crack Growth During Gross Plasticity and the J-Integral,"* In Mechanics of Crack Growth, ASTM STP 590, 82-103.

[25] J.W.Hutchinson, *"Singular Behavior at the End of a Tensile Crack in a Hardening Material,"* Journal of the Mechanics and Physics of Solids, **16**, 1968, 13-31.

[26] J.R.Rice and G.F.Rosengren, *"Plane Strain Deformation Near a Crack Tip in a Power-Law Hardening Material,"* Journal of the Mechanics and Physics of Solids, **16**, 1968, 1-12.

[27] K.Tanaka, *"The Cyclic J-Integral as a Criterion for Fatigue Crack Growth,"* International Journal of Fracture, **22**, 1983, 91-104.

[28] D.A.Jablonski and B.H.Lee, *"Computer Controlled Fatigue Crack Growth Rate Testing Using the J-Integral,"* Proceedings, Conference on Fatigue: Analysis and Prediction, U.S.Goel, Ed., American Society for Metals, 1985, 245-58.

[29] A.Saxena and S.J.Hudak, *"Review and Extension of Compliance Information for Common Crack Growth Specimens,"* International Journal of Fracture, **14**, 1978, 453-68.

[30] D.A.Jablonski, B.Journet, R.S.Vecchio and R.Hertzberg, *"Compliance Functions for Various Fracture Mechanics Specimens,"* Engineering Fracture Mechanics, Volume 22, Number 5, 1985, 819-27.

[31] J.D.Verhoeven, Fundamentals of Physical Metallurgy, John Wiley and Sons, New York, 1975, 421-8

[32] G.Krauss, Principles of Heat Treatment of Steel, ASM, Metals Park, OH, 1980, 10-19 & 110.

[33] R.Lunden, *"Contact Region Fatigue of Railway Wheels Under Combined Mechanical Rolling Pressure and Thermal Brake Loading,"* Wear, **144**, 1991, 57-70.

[34] G.E.Dieter, Mechanical Metallurgy, 3rd Edition, McGraw-Hill, New York, NY, 1986, 287.

[35] T.L.Anderson, Fracture Mechanics Fundamentals and Applications, CRC Press, Boca Raton, FL, 1991, 143 & 735.

[36] R.M.Pelloux and J.Liang, *"Metallographic Examination of Thermally Cracked Commuter Car Wheels,"* Department of Materials Science and Engineering, MIT, July, 1992, 1-13.

[37] C.F.Shih and H.G.deLorenzi, *"Elastic Compliances and Stress Intensity Factors for Side-Grooved Compact Specimens,"* International Journal of Fracture, **13**, 1977, 544-8.

[38] Metals Handbook, Volume 9, Fractography and Atlas of Fractographs, 8th Edition, ASM, Metals Park, OH, 1974, 27-88.

[39] C.Laird, ASTM STP 415, 1967, 131.

[40] R.M.N.Pelloux, *"Mechanisms of Formation of Ductile Fatigue Striations,"* Trans. ASM, **62**, 1969, 281-5.

[41] J.G.Merkle, *"New Method for Analyzing Small Scale Fracture Specimen Data in the Transition Zone,"* Tenth Water Reactor Safety Meeting, **4**, Materials Engineering Research, US Nuclear Regulatory Commission, Washington, DC, 1982, 307-315.

[42] J.M.Barsom and S.T.Rolfe, Fracture and Fatigue Control in Structures Applications of Fracture Mechanics, 2nd Edition, Prentice Hall, Englewood Cliffs, NJ, 1987, 169-76.

[43] S.Yu and C.Stuart, *"Wheel Peeling Experiment Report for the Cracked Wheel Investigation,"* Ensco, Inc., Springfield, VA, May 1992.

[44] D.Broek, Elementary Engineering Fracture Mechanics, 4th Edition, Kluwar Academic Press, Norwell, MA, 1991, 85.

[45] C.S.Carter, R.G.Caton and J.L.Guthrie, *"Fracture Resistance and Fatigue Crack Growth Characteristics of Railroad Wheels, and Axles,"* Report FRA/ORD-77/50, November 1977, 31.

[46] C.F.Tiffany and J.N.Masters, *"Applied Fracture Mechanics,"* in Fracture Toughness Testing and ts Applications, ASTM STP 381, 1965, 249.

[47] H.Kobayashi and H.Nakamura, *"Evaluation of the Stretched Zone Width and Striation Spacing,"* Current Japanese Materials Research, Volume 6, R.Koterazawa, R.Ebara and S.Nishida, Eds. Elsevier Applied Science, New York, NY, 1990, 141-60.

[48] R.M.Pelloux and A.S.Warren, *"Fatigue Striations and Failure Analysis,"* Proceedings of the 1st International Conference on Failure Analysis, J.I.Dickson, Ed., ASM International, July 1991, 45-9.

[49] R.D.Buchheit and D.Broek, *"Microstructural and Fractographic Characterizations of Fatigue-Tested Rail Steels,"* Final Report DOT-TSC-, October 1977, 48-80.

[50] U.Lindborg, *"Morphology of Brittle Fracture in Pearlite,"* Trans. ASM, **61**, Volume 3, September 1964, 500-4.